Vortices in unconventional correlated superconductors

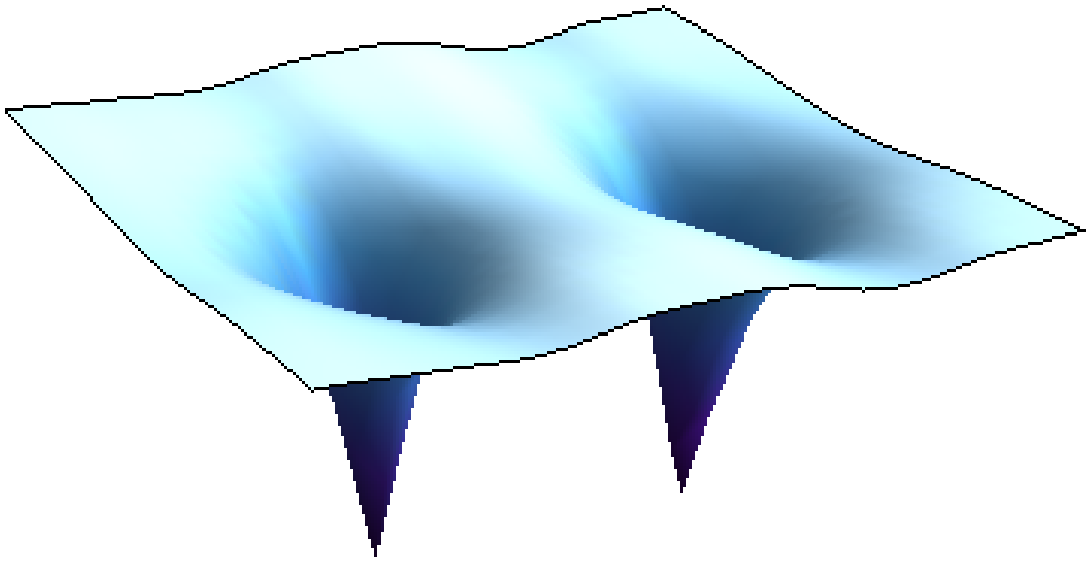

Beñat Mencia Uranga

Master's project in Physics

Supervisor: Brian M. Andersen

Niels Bohr Institute
University of Copenhagen

Signature:
September 1, 2014

Abstract

Abstract

The discovery of superconductivity in the Fe-based compounds in the year 2008 has led to thousands of publications on this subject over the last six years. These compounds are the second-highest-temperature superconducting material family known to date. In this work, we study the magnetic field dependence of the superconducting state of the Fe-based superconductors. We also study some new properties of the mixed state of the cuprates in the last chapter. To perform these studies we have built a real-space code able to deal with the five-orbital Hubbard model in the presence of a magnetic field, and solve the associated quantum mechanical problem of vortices inside superconductors. Specifically, we study; 1) the effect of the magnetic field on the magnetic order measured in neutron scattering experiments, 2) the structure of the local density of states in the vortex state, and 3) the effect of a magnetic field on the so-called neutron resonance found quite generally in neutron scattering measurements on unconventional superconductors. We reproduce qualitatively (and in some cases semi-quantitatively) several of the recent experimental results.

Laburpena

Burdinean oinarritutako konposatuetan supereroankortasunaren aurkikuntzak 2008 urtean, gai honi buruzko milaka argitarapen eragin ditu azken sei urteotan. Konposatu hauek, orain arte ezagutu diren tenperatura altuko material supereroaleen artean, bigarren temperatura altuen dun familia osatzen dute. Lan honetan, Burdinean oinarritutako supereroaleen supereroankor egoerak, eremu magnetikoarekiko duen dependentzia aztertzen dugu. Azken atalean, Kobrean oinarritutako supereroaleen egoera nahasiko berezitazun batzuk ere aztertzen ditugu. Hortarako, bost orbitaldun, espazio errealeko Hubbard eredu bat sortu dugu eremu magnetiko baten presentzian, eta supereroale barneko bortitzeei dagokion kalkulu kuantikoa egin dugu . Aztertzen dugu 1) eremu magnetikoak neutroi sakabanaketa experimentuetan neurtutako ordena magnetikoarengan duen eragina, 2) bortize egoeran egoeren-dentsitate lokalak duen egitura, eta 3) eremu magnetikoak duen eragina Kobre-an oinarritutako tenperatura altuko supereroaleetan egindako neutroi sakabanaketan neurketetan. Zenbait emaitza experimental erreproduzitzen ditugu, gehien bat modu kualitatiboan baina batzuek modu kuantitatiboan ere bai.

Resumen

El descubrimiento de la superconductividad en compuestos basados en Hierro en el ao 2008, ha originado miles de publicaciones sobre este tema en los ltimos seis aos. Estos compuestos constituyen la familia de materiales superconductores de segunda ms alta temperatura conocidos hasta la fecha. En este trabajo, estudiamos la dependencia del campo magntico del estado de superconductividad de los superconductores basados en Hierro. Tambin estudiamos algunas nuevas propiedades del estado mixto de los superconductores Cobre en el ltimo captulo. Para ello, construimos un modelo Hubbard de cinco orbitales de espacio real en presencia de un campo

magntico, y resolvemos el problema mecnico cuntico de los vrtices en los superconductores. Estudiamos 1) el efecto del campo magntico sobre el orden magntico medido en los experimentos de neutron scattering, 2) la estructura de la densidad local de los estados en el estado vorticial, y 3) el efecto del campo magntico en las mediciones de neutron scattering en superconductores basados en cobre de altas temperaturas. Reproducimos cualitativamente (y en algunos casos cuantitativamente) algunos de los resultados experimentales recientes.

Resume

Opdagelsen af superledning i de Fe-baserede materialer i 2008 har allerede medført tusindevis af publikationer indenfor dette felt gennem de seneste seks år. Disse systemer udgør pt den familie af sammensætninger med den anden højeste kritiske overgangstemperatur T_c. Vi har valgt at studere magnetfelt-afhængigheden af den superledende fase af disse Fe-baserede materialer. Det samme gælder for kupraterne (Cu-baserede høj-T_c superledere) studeret i det sidste kapitel. For at foretage disse studier har vi opbygget en real-space kode, som gør det muligt for os at udføre beregninger med fem-orbital Hubbard modellen med et eksternt påtrykt magnetfelt, og dermed løse det medfølgende kvantemekaniske problem om hvirvler i superledere. Vi studerer mere specifikt; 1) effekten af magnetfeltet på den magnetiske orden målt i neutron spredningseksperimenter, 2) strukturen i den lokale tilstandstæthed i hvirvelfasen, og 3) effekten af et magnetfelt på den såkaldte neutron resonans fundet generelt i neutron spredningsmålinger på ukonventionelle superledere. Vores resultater forklarer kvalitativt (og i nogle tilfælde næsten kvantitativt) adskillige af de seneste eksperimentelle resultater.

Contents

Chapter 1

Introduction

In the year 2008, Hideo Hosono and collaborators [41] found the first iron based superconductor(FeSC), it was iron arsenide LaFeAsO with critical temperature 26K. Within two months, the critical temperature of Fe-based materials was raised to 55K by the synthesization of materials based on substitution of La with other rare earths. This fast sequence of discoveries attracted the high-temperature superconductivity community. During the next three years, many related families of materials were discovered, their electronic structure was calculated based on density-functional theory (DFT), and many microscopic models based on these DFT calculations were developed. The existence of a second family of superconductors, is not only good because of the possibility of finding materials with even higher T_c within the same family, but also because the comparison with cuprates may give some important hints for the recipe for the high-T_c superconductors. Among others, one of the fascinating issues with FeSC is the structure and the symmetry of the superconducting gap. In the study of the cuprates, $d_{x^2-y^2}$ symmetry with $\cos k_x - \cos k_y$ gap structure was soon established after high quality samples were prepared by penetration depth, ARPES, NMR and phase sensitive Josephson tunneling experiments. After six years of intense research, there is still no universal consensus about the gap structure in the FeSC and there is strong evidence that small differences in the electronic structure might lead to a big diversity in gap structure, including gaps with nodes in some materials and full gaps in others. The symmetry is probably A_{1g} (s-wave), with sign change of the order parameter between the Fermi surface (FS) sheets. There have also been suggestions for d-wave symmetry. Understanding the symmetry of the ground state and its detailed structure, might help to understand what is the pairing mechanism in FeSC and more generally high-T_c superconductivity.

1.1 Comparison with cuprates

Cuprates are characterized by their high T_c, unconventional superconducting state and unusual normal state properties. The FeSC with T_c up to 55K in $SmFeAsO_{1-x}F_x$ stand in second place after cuprates and 15K above MgB_2. Let us compare the main properties of FeSC with those of cuprates.

In both, the buildings blocks are 2-dimensional lattices of $3d$ transition metal ions (see Fig. 1.2). In both of them an orthorhombic distortion of the lattice at small doping is present (see Fig. 1.4). On the other hand, while 2p ligands lie very nearly in-plane with Cu in cuprates, in FeSC, As, P, Se, or Te lie in nearly tetrahedral positions above and below the Fe planes. For the cuprates, all in-plane d-orbitals e_g have weight on the Fermi surface, but among these, $d_{x^2-y^2}$ is by far the one with the strongest presence; this fact allows to reduce the multiband electronic structure to an effective low-energy single band model. In the FeSC, As hybridize well with the t_{2g} Fe d-orbitals and all of them have weight at the Fermi surface. There is a substantial overlap

between all d-orbitals. This implies that the minimal model is essentially multiband. The phase diagrams of the cuprates are quite similar to many of the FeSC (see Fig. 1.4). The undoped compounds exhibit antiferromagnetism and it vanishes with doping. Superconductivity appears at some non-zero doping and then it disappears, thus T_c forms a "dome". In the case of cuprates, the long range ordered Néel phase vanishes before superconductivity appears, whereas in the FeSC the competition between the two orders might take several forms (see Fig. 1.4). Although it might be tempting to think that they are similar, there are some profound differences. The first striking difference is that cuprates are Mott-insulators in the normal state whereas FeSC are metals. This fact implies that the Mott-Hubbard physics of half-filled Hubbard model is not quite a good starting point for FeSC although some people have studied them within a strong-coupling approach. Of course, correlations should not be ruled out but these might be small or moderate. DFT-based approaches give the right FS and band structure for the FeSC but not for cuprates, especially in the undoped and underdoped regime. The second important difference regards the normal state. Underdoped cuprates show a pseudogap behavior, there are also diverse competing orders. Hole doped cuprates show a strange metal phase with a resistivity linear in T near optimal doping. In the FeSC, different power laws have been observed near the optimal doping, these have been interpreted as happening due to multiband physics and interband scattering [22]. The FeSC do not have a pseudogap behavior.

1.2 Conceptual importance

The discovery of the FeSC was not a big step towards the applications of superconductors, their T_c is only $15K$ higher than the one of MgB_2, they are expensive to make and difficult to work with, as cuprates. On the other hand, the conceptual step is fairly large. It had been thought by many people that phonon driven superconductivity would never go beyond 50-60K and that high-T_c superconductivity was a strong correlation phenomenon uniquely limited to the family of layered cuprates. It was pointed out that CuO_2 layers have many unique properties, largely due to the fact that Cu is the last $3d$ transition metal of the fourth period of the periodic table and by far the most correlated [35]. What the FeSC brought to the table was that, however unique cuprates may be, their properties are not a prerequisite for non-phonon high-T_c superconductivity. This means that there may be other crystallochemical families with even higher T_c more suitable for applications. So somehow it is actually good that FeSC are so different from cuprates and one should look for the commonalities and assume, not necessarily with a deep theoretical insight, that these are important for high T_c superconductivity. Some of these are proximity to magnetism and quantum criticality, or substantial anisotropy of the Fermi surface (quasi-2D).

1.3 Electronic structure and phase diagram

The parent compound of FeSC is a semimetal in the normal state. Fig. 1.1, shows schematically the band structures of a semiconductor and a semimetal. The lower band is the valence band and the upper band is the conduction band. In a semimetal, those bands are separated in k vector and they slightly overlap in energy. Hence, the electrons at the top of the valence band jump to the conduction band, until the electrons at the top of the valence band have the same energy as the ones in the conduction band. The charge carriers at the top of the valence band are holes and the ones in the conduction band are electrons; that is why people speak of hole pockets and electron pockets in the literature.

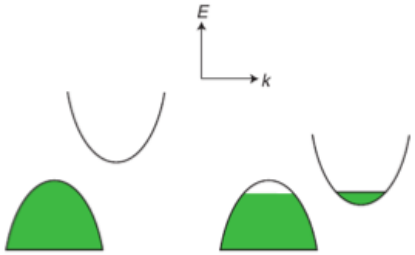

Figure 1.1: Band structures of a semiconductor (left) and a semimetal (right). The parts of the band filled by electrons are shown as green. In the semiconductor (semi because we assume the gap is small), there is a gap between the lower and the upper band, thus at $T = 0$ it is an insulator. In the semimetal, the two bands overlap in energy thus, at $T = 0$, it is a metal with a finite conductivity.

The common feature of all known FeSC is an FeX' square lattice, where X' may be a pictogen (As or P), or a chalcogen(Te, Se or S). Between these FeX' layers, there may be an additional oxide layer('1111' materials), ionic layer ('122' or '111' materials), more complex intermediaries (e.g. '42622' materials) or nothing ('11' materials). Some representative structures are shown in Fig. 1.2.

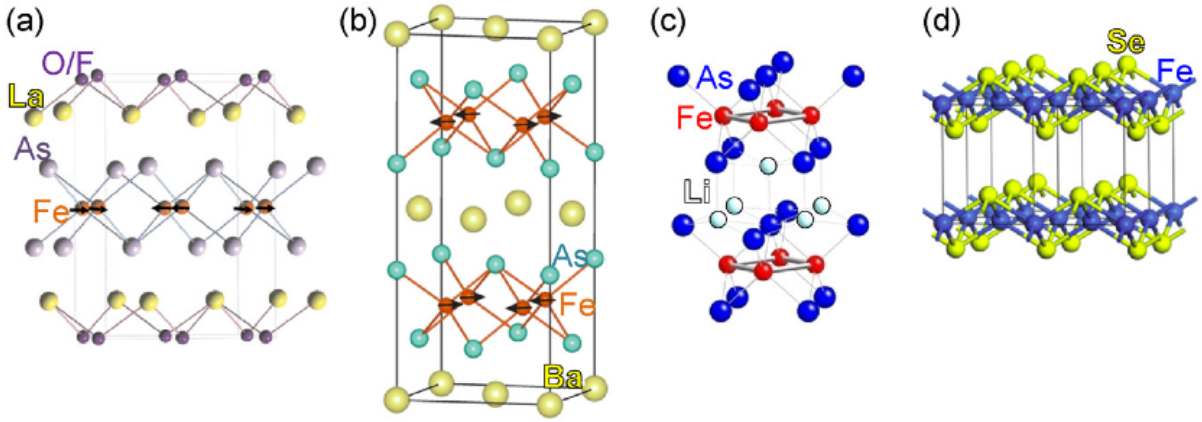

Figure 1.2: Strucutres of (a)1111($LaFeAs_{1-x}F_x$), (b)122($BaFe_2As_2$), (c)111($LiFeAs$) and (d) 11($FeSe$). Figure taken from [36].

In three of the FeSC families, namely 1111, 122 and 111, the basic crystallographic element is the FeX' plane with an axa square plane of Fe and a $\tilde{a}$x$\tilde{a}$ of X' above and below ($\tilde{a}$=$\sqrt{2}a$) (see Fig. 1.3(a)). Therefore, the minimal unit cell of the entire Fe and X' plane is $\tilde{a}$x$\tilde{a}$.

The low energy part the electronic structure can be unfolded to a Brillouin zone (BZ) which is twice as large as the folded one, corresponding to the axa unit cell, so that the real band structure can be recovered by folding the 2D BZ in such a way that the "unfolded" X and Y points fold on top of each other, forming the $\tilde{M}$ point in the small BZ (see Fig. 1.3(c)). Throughout the thesis, we will always use the untilded notation in the one-Fe unit cell and the "unfolded" BZ, and the tilded notations in the crystallographic unit cell (the real one) and the corresponding BZ.

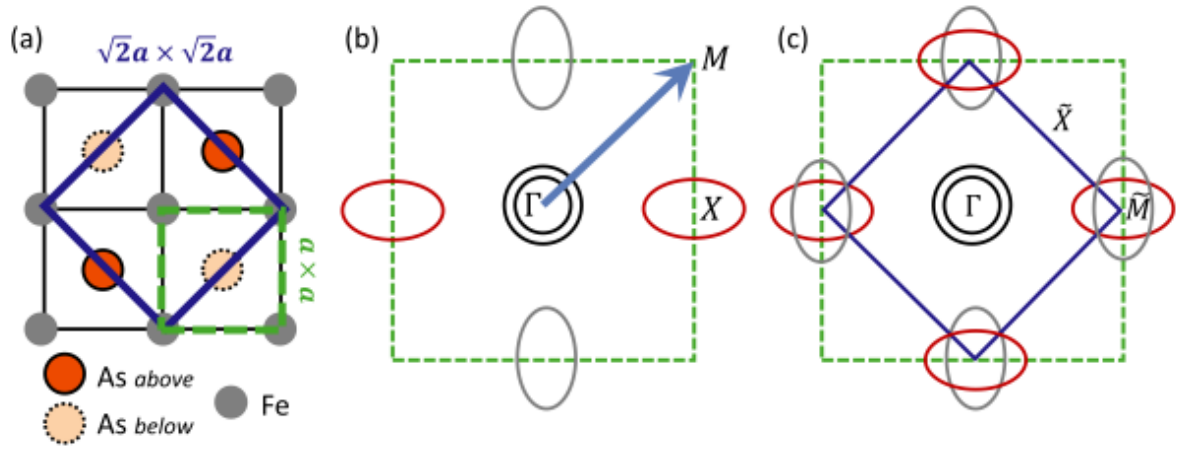

Figure 1.3: (a) FeX'(X'=As) lattice indicating As above and below the Fe plane. Dashed green and solid blue squares indicate 1- and 2-Fe unit cells, respectively. (b) Schematic 2-dimensional Fermi surface in the 1-Fe Brillouin zone whose boundaries are indicated by a green dashed square. Arrow indicates folding wave vector Q_F. (c) Fermi sheets in the folded Brillouin zone whose boundaries are now shown by a solid blue square. Figure taken from [35].

All FeSC show similar gross features in the electronic structure. These can be listed as follows:

1. In the non magnetic state, the band structure is semimetallic, two or more hole bands cross the Fermi level near the Γ point and two electron bands cross it near the $\tilde{M}$.

2. Two hole bands are present at the FS, derived from the d_{xz} and d_{yz} Fe orbitals. They are degenerate at the symmetric Γ point but they split apart in a smooth way away from it. The two electron bands come from the downfolding described above; these are mainly d_{xz} and d_{yz}, but also partly d_{xy}.

3. As a result, there are always at least two electron and two hole bands well separated in the momentum space. In general, because the Fermi surfaces have different shapes, one cannot speak of nesting but only quasi-nesting.

The degree of charge doping varies among the different materials, it ranges from $0.5h$ to $0.15e$ per Fe. Although the shape of the FS changes upon doping by enlarging or shrinking the sheets, they never disappear within the superconducting range of doping, even though the nesting gets completely deteriorated.

The FeSC exhibit a dome shaped phase diagram with an antiferromagnetic parent compound, like the cuprates. They undergo a structural phase transition which is often but not always simultaneous with the magnetic phase transition. Representative phase diagrams are shown in Fig. 1.4.

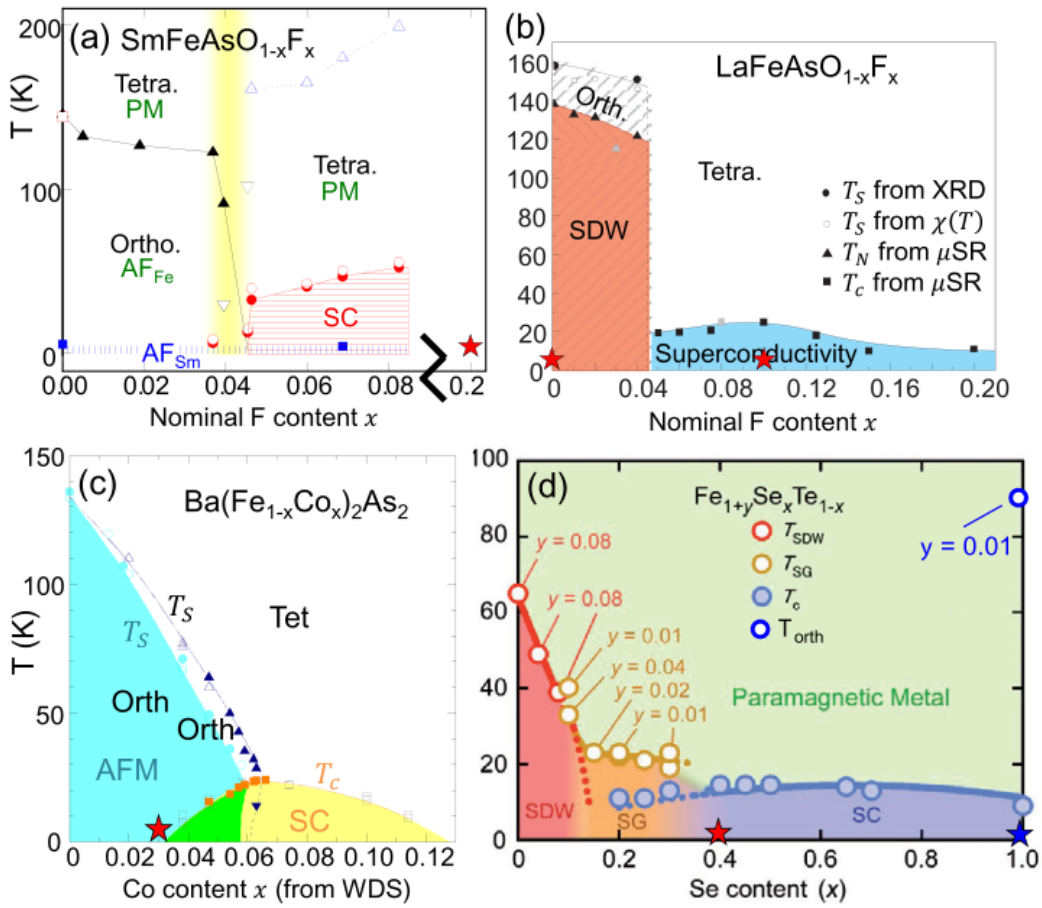

Figure 1.4: Some phase diagrams of several FeSC, representative of the 1111, 122 and 11 families. Figure taken from [36].

1.4 The superconducting state

Currently, it is still not clear what is the mechanism which causes superconductivity in the high-T_c superconductors. Whereas in the BCS superconductors, the mechanism causing the pairing of the electrons is the electron phonon interaction, it was realized that this mechanism is not strong enough to produce the observed high T_c [51]. Evenso, once the system enters in the superconducting state, the BCS theory suffices to explain the phenomena with a quite high level of accuracy. Thus, we start by explaining the BCS theory.

1.4.1 The BSC theory

Probably the most important concept in BCS theory is the Cooper pair. Cooper found that an arbitrarily weak attraction between electrons would lead to a rearrangement of the Fermi surface and the formation of quasi-bound electron pairs, named Cooper pairs. The attractive interaction leading to the creation of Cooper pairs is mediated by phonons (in conventional superconductors). To get some intuition in the Cooper pair formation, we can think of the classical picture where an electron attracts the positively charged ions, polarizing the surrounding. When the electron moves away, the ions still keep being there because they are much heavier than the electrons and their time scale is much slower. So, this net positive charge, attracts another electron. This is how electrons have an effective attractive interaction despite the Coulomb

repulsion. They basically avoid the Coulomb repulsion by being at the same place at different times.

At $T = 0$, without interactions, the lowest energy state corresponds to the state where all the states below the Fermi surface are filled and the ones above are empty. This corresponds to the state where the kinetic energy is minimum and the potential energy zero. When interactions are present, namely, the attractive interactions between electrons, the contribution of this potential energy is negative, i.e. it lowers the energy. But this can only be possible if the pair is allowed to scatter from state (k_1, k_2) to $(k_1^{'}, k_2^{'})$, i.e. if state (k_1, k_2) is filled and state $(k_1^{'}, k_2^{'})$ empty before the scattering. Thus, the Fermi sphere with all the states below filled and all states above empty is not the ground state anymore. When the states above the Fermi surface are being filled up, it happens in pairs $k_\uparrow$ and $-k_\downarrow$. Why does this happen?

When a transition from (k_1, k_2) to $(k_1^{'}, k_2^{'})$ happens, there must be conservation of momenta, i.e. $k_1 + k_2 = k_1^{'} + k_2^{'}$. The more Cooper pairs are created the more the energy is lowered. Now consider, for example, $k_1 + k_2 = q$ as illustrated in Fig. 1.5. Here only the electrons occupying the k states in the dashed areas of momentum space are allowed to participate in the transitions. Now if we reduce q, the dashed areas will grow larger. Finally, at $q = 0$, all states within a band of width $2\hbar w_D$ around the Fermi surface will contribute to the reduction of the energy. Thus, this is why the Cooper pairs are formed by time reversed electrons.

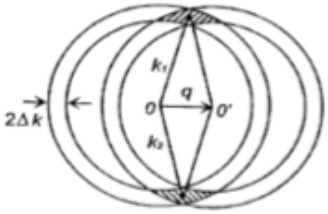

Figure 1.5: If coupled electrons have a total momentum q, the interaction involves only the electrons occupying k states within the dashed are.

The mean field BCS Hamiltonian is given by

$$H_{BCS}^{MF} = \sum_{k\sigma} \xi_k \hat{c}_{k\sigma}^\dagger \hat{c}_{k\sigma} - \sum_k (\Delta_k \hat{c}_{k\uparrow}^\dagger c_{-k\downarrow}^\dagger + H.c.) \tag{1.1}$$

where the operators $\hat{c}_{k\sigma}^\dagger$ ($\hat{c}_{k\sigma}$) create (annihilate) an electron with momentum k and spin projection σ. ξ_k is the energy of the free electrons and $\Delta_k = -\sum_{k'} V_{kk'} \langle \hat{c}_{-k'\downarrow} \hat{c}_{-k'\uparrow} \rangle$ is the superconducting order parameter. The superconducting pairing $V_{kk'}$ is assumed to be negative leading to an attractive force between electrons, which in conventional superconductors is due to the electron-phonon interaction. By performing a Bogoliubov transformation

$$\hat{c}_{k\sigma} = u_{k\sigma} \hat{\gamma}_{k\sigma} + v_{k\sigma}^* \hat{\gamma}_{\bar{\sigma}}^\dagger \tag{1.2}$$

$$\hat{c}_{k\sigma}^\dagger = u_{k\sigma}^* \hat{\gamma}_{k\sigma}^\dagger + v_{k\sigma} \hat{\gamma}_{\bar{\sigma}} \tag{1.3}$$

the Hamiltonian is brought into a quadratic form

$$H_{BCS}^{MF} = \sum_k E_k (\gamma_{k\uparrow}^\dagger \gamma_{k\uparrow} + \gamma_{k\downarrow}^\dagger \gamma_{k\downarrow}) + GS. \tag{1.4}$$

The Bogoliubov quasiparticle excitation spectrum is given by $E_k = \sqrt{\xi_k^2 + |\Delta_k|^2}$, which implies that there is no fermion excitations with energies less than $|\Delta_k|$. Thus, the supercon-

ducting order parameter (SCOP) provides the so called superconducting gap. In a uniform superconductor, the interaction depends only on the relative position of the electrons $V(\rho)$, with $V(\rho) \equiv r - r'$ in real space. Therefore, in the absence of inhomogeneities like impurities or vortices, the structure of the SCOP depends on the symmetry properties of $V(\rho)$. If the attraction is local, $V(\rho) = V_0\delta(\rho)$, the Fourier transform of the interaction is a constant $\Delta_k = \Delta_0$, which is the structure of an isotropic s-wave superconductor.

1.4.2 Gap symmetry and gap structure

The superconducting order parameter (SCOP) or "gap function" Δ, is a complex quantity which describes the macroscopic quantum state of the Cooper pairs. Its amplitude and phase are sensitive to the details of the pairing interactions. Thus, understanding the symmetry and structure of Δ should provide clues to the microscopic origin of the pairing mechanism in the FeSC.

The first question to address is the symmetry of the gap of the FeSC. Because the electrons are fermions, the full wave function of the Cooper pairs must be antisymmetric. The pair wave function $\Psi_{\sigma\sigma'}(k) = g(k)\chi_{\sigma\sigma'}$ contains a spin part $\chi_{\sigma\sigma'}$ and a spatial part $g(k)$. Therefore, the spatial part of $\Psi_{\sigma\sigma'}(k)$ must be even if the spin part is odd (spin-singlet), and odd if the spin part is even (spin-triplet). Expanding in eigenfunctions of orbital angular momentum, it follows that spin singlet pairing corresponds to an even spatial function of k and hence we call it s-wave (for $l = 0$), d-wave (for $l = 2$), etc. superconductor in analogy to the eigenstates of the Hydrogen atom. It follows similarly for triplet superconductors, as we refer to them as p-wave (for $l = 1$), f-wave (for $l = 3$) etc. So far, experiments seem to rule out spin triplet superconductivity, thus the spatial part must be even. We are left then with the following singlet pairing possibilities: s-wave, d-wave, g-wave etc. according to how the order parameter transforms under rotations by $\pi/2$ and other operations of the tetragonal group. For example, in the s-wave case there is no sign change under $\pi/2$ rotation whereas in the d-wave case, there is.

It should be noted that the symmetry and the structure of Δ are two different things. Within a given symmetry class, there are different k dependences of the gap, to which we refer as different structures (see Fig. 1.6). These different structures might include anisotropy of the amplitude, nodes, changes of sign etc. These are driven by the details of the pairing interaction and are not dictated by symmetry. Due to the complexity of the FS in FeSC (see Fig. 1.3(b)), there are many different ways in which the superconducting gap might open in each band, even for the simple s-wave symmetry. The simplest case, is the so called s_{++} state where the gap has the same amplitude and phase in all the pockets (see Fig. 1.6(s_{++})). But there could also be the case where there is a relative π phase (sign change) between the pockets. This is called the extended s or $s_{\pm}$ state (see Fig. 1.6($s_{\pm}$)) and even though there is an inter pocket sign change, this state is still invariant under $\pi/2$ rotations. Another possibility is that, apart from the sign change between the pockets, there is also a sign change within the pockets (nodes). This state is called the nodal $s_{\pm}$ (see Fig. 1.6(nodal $s_{\pm}$)). These three examples have the same symmetry, i.e. the s symmetry, but they all have different structures. The three cases and d-wave case are illustrated in Fig.1.6.

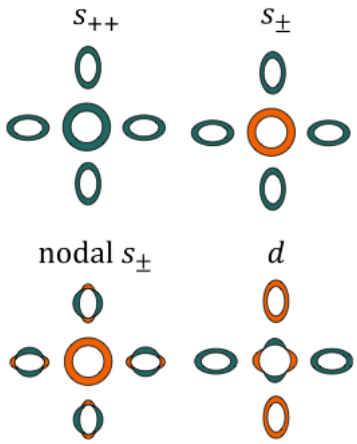

Figure 1.6: Cartoon of order parameters under discussion in the FeSC represented in the 2-dimensional, 1-Fe BZ. Different colors stand for different signs of the gap. Figure taken from [35].

Representative gap functions in a tetragonal lattice for both s-wave and d-wave symmetries are discussed below and shown in Fig. 1.7.

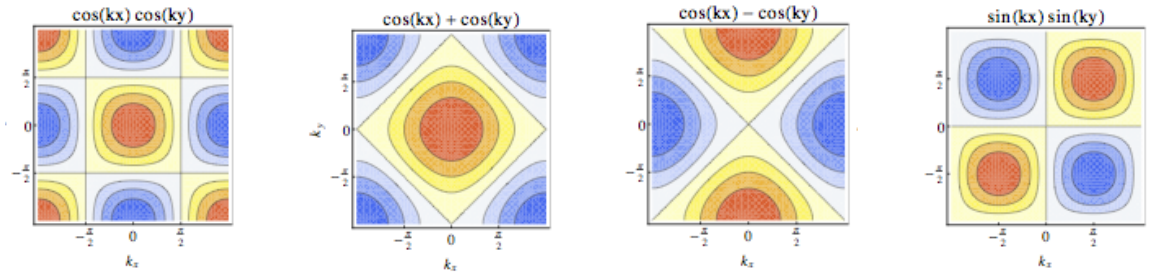

(a) (b) (c) (d)

Figure 1.7: Representative gap functions for the tetragonal lattice(red=+,blue=-). From left to right: (a) $\Delta_k^{s\pm}$, (b) $\Delta_k^{s\pm *}$, (c) $\Delta_k^{d_{x^2-y^2}}$ and (d) $\Delta_k^{d_{xy}}$. The nodes are expressed by black lines. Figure taken from [21].

In the following, we consider pairing up to next-nearest neighbors in a square lattice.

$s_{\pm}$ symmetry

Pairing each site (real space) with its four next-nearest neighbors and with the same sign of the pairing, leads to an $s_{\pm}$ state with structure:

$$\Delta_k^{s\pm} = 4\Delta_0 \cos k_x \cos k_y, \tag{1.5}$$

which is shown in Fig. 1.7(a).

nodal $s_{\pm}$ symmetry($s_{\pm}^*$)

Pairing each site with its four nearest neighbors and with same sign of the pairing, leads to an $s_{\pm}^*$ state with structure:

$$\Delta_k^{s_\pm^*} = 2\Delta_0(\cos k_x + \cos k_y), \tag{1.6}$$

which is shown in Fig. 1.7(b). By looking at Fig. 1.3(b) and 1.7(b), one can see that there is a sign change of the gap within the electron pockets at X and Y giving rise to nodes.

$d_{x^2-y^2}$ symmetry

Pairing each site with its four nearest neighbors and with sign change under $\pi/2$ rotation, leads to a $d_{x^2-y^2}$ state:

$$\Delta_k^{d_{x^2-y^2}} = 2\Delta_0(\cos k_x - \cos k_y), \tag{1.7}$$

which is shown in Fig. 1.7(c).

d_{xy} symmetry

Pairing each site with its four next-nearest neighbors and with sign change under $\pi/2$ rotation, leads to a d_{xy} state:

$$\Delta_k^{d_{xy}} = 4\Delta_0 \sin k_x \sin k_y, \tag{1.8}$$

which is shown in Fig. 1.7(d).

Among all these possibilities, the leading candidate for the FeSC is the $s_\pm$ state. To understand why, let us look at the finite-temperature BCS gap equation,

$$\Delta_k = -\sum_{k'} V_{kk'} \frac{\Delta_{k'}}{2E_{k'}} tanh \frac{E_{k'}}{2T}. \tag{1.9}$$

From Eq.(1.9), we see that the sign of $V_{kk'}$ restricts the possible solutions for Δ_k. For conventional superconductors, the effective electron-electron interaction mediated by phonons is attractive and therefore $V_{kk'} < 0$. Then, the gap equation allows for an isotropic solution $\Delta_k = \Delta_0$. In the FeSC, the phonons are not enough to overcome the Coulomb repulsion, hence $V_{kk'} > 0$. Therefore, Eq.(1.9) only allows for solutions where the gap changes sign,

$$\Delta_k = -\Delta_{k+Q}. \tag{1.10}$$

Therefore, repulsive interactions might still lead to pairing only if the wave vector Q of such a fluctuation spans parts of the FS where the gap changes sign. Let us assume now, that what causes pairing in the FeSC is the exchange of spin fluctuations (see Chapter 4). The band structure gives rise to a spin susceptibility that peaks at $Q = (\pi, 0)$ and $Q = (0, \pi)$ [35], which implies that the effective interaction mediated by the exchange of spin fluctuations $V_{kk'}$ is peaked at this nesting vector. Thus, because this is the vector connecting the hole and electron pockets, the gap equation will only allow for solutions where the gap changes sign between the hole and electron pockets, i.e. a $s_\pm$ state (see Fig. 1.8).

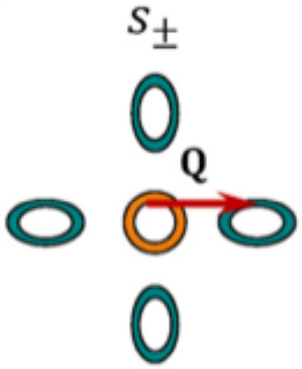

Figure 1.8: Illustrative figure of the nesting vector connecting the hole and electron pockets. Figure taken from [35].

1.5 Important experimental methods

In this section we will give first a brief explanation of the main experimental methods relevant to our work.

Scanning tunneling microscopy (STM) and Quasiparticle interference (QPI)

A scanning tunneling microscope consists of a sharp metallic tip which is rastered several Ångstroms above an electrically conducting sample surface (see Fig. 1.9 (a)). The position of the tip can be varied with sub-Å precision by means of a piezoelectric scanner. When a voltage V is applied between the tip and the sample, a current flow takes place. This current I can be measured as a function of position and bias voltage V [36]. This is done by sweeping V while keeping the distance between the tip and the sample unchanged. By differentiating $I(V)$, the conductance dI/dV is found to be proportional to the sample density of states (DOS).

$$\frac{dI}{dV} = -\frac{4\pi e^2}{\hbar} e^{-d\sqrt{\frac{8m\varphi}{\hbar^2}}} \rho_{tip}(0) DOS(eV) \tag{1.11}$$

where m is the mass of the electron, d is the tip-sample separation, φ is the height of the vacuum barrier (typically $\sim 3 - 5eV$) and ρ_{tip} is the density of states of the tip. Thus, this technique allows to measure the energy spectra in both the filled and the empty states. That is how for example, the superconducting gap can be measured (see Figures 1.9 (b) and (c)).

When materials are inhomogeneous and electrons are highly correlated, a full understanding of their properties requires knowledge of both the real-space and momentum-space behavior of quasiparticles. Whereas STM provides real space information about the energy spectrum (the tip is moved in real space), QPI provides momentum space dependent information. When quasiparticles scatter off defects or other structures within the crystal, energy dependent standing waves form. The resulting interference patterns in the quasiparticle DOS can be imaged with STM. The Fourier transform of the real-space interference patterns highlights the dominant sets of quasiparticle momenta (see Fig. 1.10). This information can be used to distinguish between candidate SCOP [36].

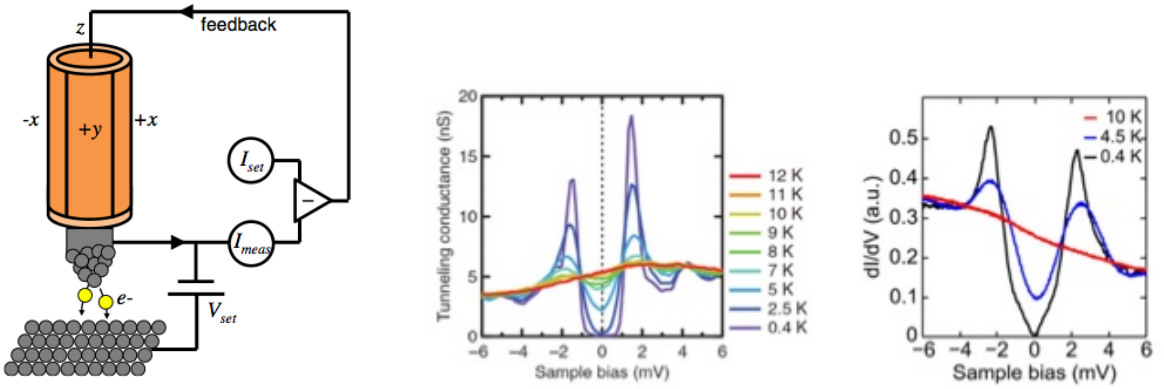

(a) (b) (c)

Figure 1.9: (a) Schematic of a scanning tuneling microscope. A voltage is applied between the conducting sample surface and a sharp metallic tip, leading to a measurable tunneling current whose magnitude decays exponentially with tip-sample separation. dI/dV measured in (a) $FeTe_{1-x}Se_x$ and (b) $FeSe$. Figure taken from [36].

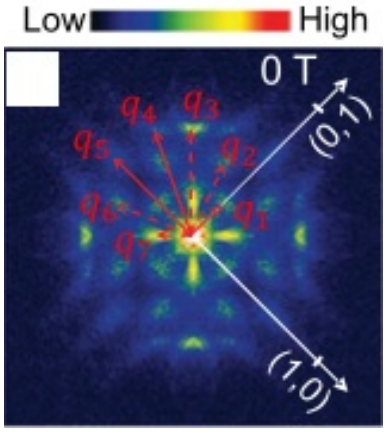

Figure 1.10: Measurements by QPI technique on FeSC materials. Figure taken from [36].

Angle-Resolved Photoelectron Spectroscopy (ARPES)

ARPES is a direct experimental technique to observe the distribution of the electrons (more precisely, the density of single-particle electronic excitations) in the reciprocal space of solids [21]. This method, apart from the band structure, probes the superconducting gap structure(see Fig. 1.11).

ARPES is a photon-in electron-out spectroscopy based on the photoelectric effect. An incoming photon, generated in x-ray sources or laser systems, is directed at a sample where it is absorbed. If the photon supplies sufficient energy to the electron it can overcome the work function and exit the sample as a photoelectron. A movable detector, equiped with an energy filter, captures the photoelectrons in a specific energy range and solid angle. Using conservation of momentum and energy, one can then deduce information about the electron's initial momentum, energy and lifetime and therefore information about the underlying electronic structure. Applying this technique to many body systems, where the electronic structure is not well described by conventional band theory, has provided important insights into many-body physics [1]. ARPES can be interpreted as a direct measure of the single particle spectral function $A(\mathbf{k}, w)$.

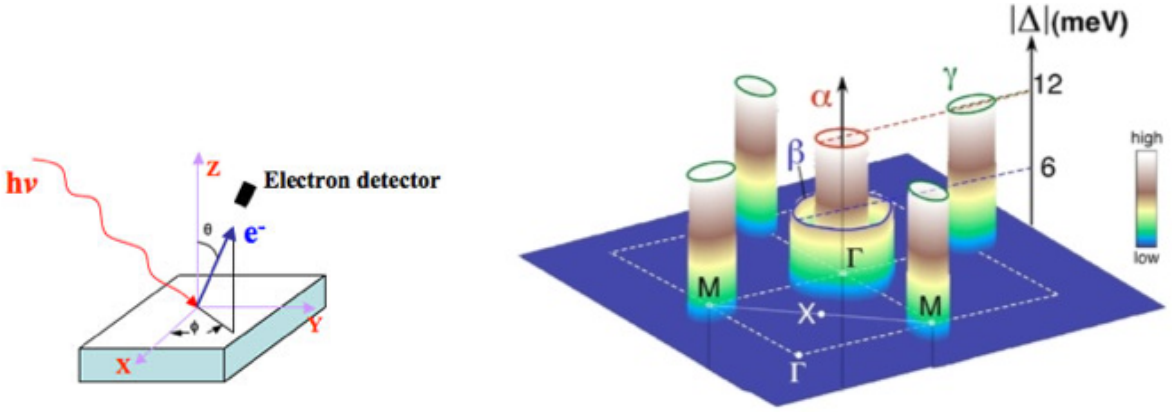

(a) (b)

Figure 1.11: (a) A cartoon of the photoemission process and experimental setup of a typical ARPES experiment. (b) Fermi sheets and superconducting gaps of hole-doped $Ba_{0.6}K_{0.4}Fe_2As_2$, measured by ARPES. Figures taken from [36] and [1] respectively.

Inelastic neutron scattering

The scattering of slow neutrons off crystals provides a very powerful probe of the quantum states in solids because the energy and wavelength of the neutrons are comparable to the excitations in the crystal. The neutrons interact with solids via 1) the nuclear force leading to neutron-ion scattering with possible emission and absorption of phonons, and 2) the magnetic dipole-dipole interaction between the very weak magnetic moment of the neutron and the magnetic moments in the solid [47]. In the following we focus on the dipole interaction which leads to enhanced neutron scattering signals from systems where magnetic fluctuations are present.

The magnetic neutron scattering cross section per formula unit is given by

$$\left(\frac{d^2\sigma}{d\Omega dE}\right) = (\gamma r_e)^2 \frac{k_f}{k_i} |F(\mathbf{q})|^2 S(\mathbf{q}, w), \tag{1.12}$$

where $k_i(k_f)$ is the initial(final) wave vector of the neutron, $\mathbf{q} = \mathbf{k_i} - \mathbf{k_f}$ the scattering vector, w the energy loss, γ is the gyromagnetic ratio and $r_e = e^2/m_e c^2$. $F(\mathbf{q})$ denotes the magnetic form factor of the ions (Cu^{2+} in cuprates...). The magnetic structure factor, $S(\mathbf{q}, w)$, is the Fourier transform of the spin-spin correlation function. $S(\mathbf{q}, w)$ is related to the imaginary part of the spin susceptibility $\chi''(\mathbf{q}, w)$ through the fluctuation-dissipation theorem

$$S(\mathbf{q}, w) = \frac{\chi''(\mathbf{q}, w)}{1 - e^{-w\beta}}. \tag{1.13}$$

1.6 Experiments on vortices

In this section, we will focus mostly on STM experiments. The relevant inelastic neutron scattering experiments will be explained in Chapters 5 and 7.

Since the first experiments done by Hess *et al* [32], STM has provided abundant information about vortices. It is only by this technique that it is possible to directly access the internal vortex structure to provide the coherence length ξ and even fundamental information about electron pairing [28, 62].

In 1964, Caroli *et al* predicted that in the core of the vortices there would be low energy bound states separated by $\sim \Delta^2/E_F$ [10] (see Fig. 1.12(a)). Since E_F is typically much larger than Δ for conventional superconductors, the excitation spectra will appear as a continuous of states peaked at E_F, as it is shown in Fig. 1.12(b).

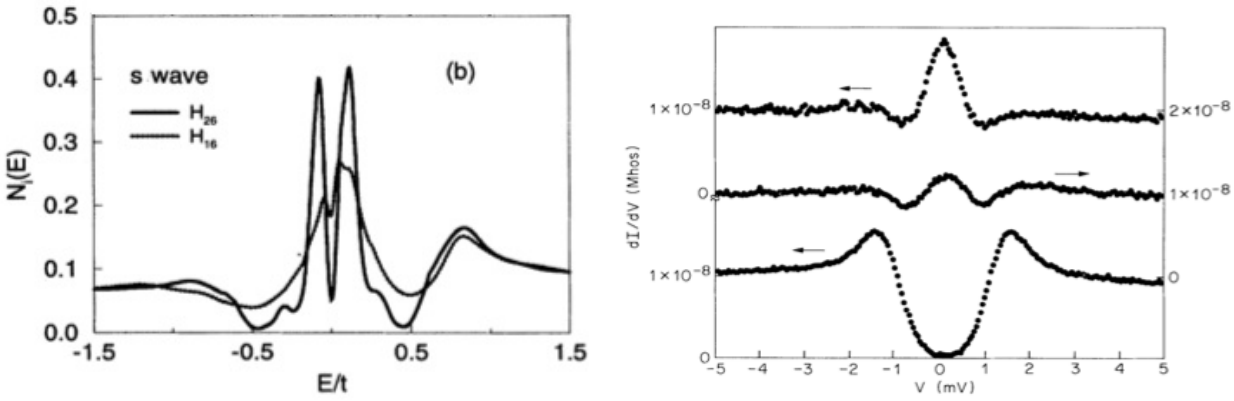

(a) (b)

Figure 1.12: (a) Quasiparticle LDOS at the center of the vortex core for an s-wave model. (b) dI/dV vs V for $NbSe_2$ taken at three positions: at the vortex center, about 75 Å from a vortex and 2000 Å from a vortex. Figures taken from [70] and [32].

On the other hand, in FeSC, due to a small carrier density (small E_F) and high T_c (large Δ), Δ^2/E_F is relatively large and the spectra are no longer continuous. Thus, the quantum limit regime might be anticipated, in which, the thermal smearing is narrower than the discrete bound states levels. Theoretical analysis of the quantum-limit vortex for a one band s-wave superconductor predicts strong particle-hole asymmetry in a LDOS spectrum at the vortex center [29].

STM experiments found low energy bound states at the vortex core of stoichiometric $FeSe$ [62] and $LiFeAs$ [28], as well as hole-doped $Ba_{0.6}K_{0.4}Fe_2As_2$ [40]. In $FeSe$, the core states where found exactly at E_F, as shown in Fig. 1.13(a). These peaks split into two symmetric subpeaks and eventually merge into the coherence peaks along the Fe-Fe orthorhombic b axis, in a similar manner to $NbSe_2$ [33]. Along the a axes, there is also a splitting but the subpeaks do not merge into the coherence peaks but rather fade away. This gives evidence of the two fold symmetry of the electron pairing in this material. In contrast, in $LiFeAs$ and $Ba_{0.6}K_{0.4}Fe_2As_2$, the LDOS was found to be particle-hole asymmetric as the vortex states were found below E_F (see Figures 1.13(b) and (c)).

In addition, STM revealed different vortex shapes in different materials. In $FeSe$, the vortex appears elongated along the a-axis (see Fig. 1.14(a)) despite the fact that the lattice is 99.5% tetragonal, leading to the suggestion that the electron pairing is two-fold symmetric in $FeSe$ [40]. In contrast, LDOS in $LiFeAs$ shows a four-fold star shape with tails oriented at 45° to the nearest Fe-Fe direction, as it shown in Fig. 1.14(b). We will elaborate on this in Chapter 6. In nonstoichiometric FeSCs, single vortices often appear irregularly shaped and it is challenging to identify the vortex structure. To overcome this issue, Song *et al* registered the vortex centers and then averaged the density of states from 48 vortices in $Sr_{0.75}K_{0.25}Fe_2As_2$ [17]. Although the material is in the orthorhombic phase, the averaged vortex appears nearly isotropic (see Fig. 1.14(c)), in contrast to the two- and four-fold symmetric vortices in FeSe and LiFeAs. This fact supports the claim that the orthorombicity is not the responsible for the anisotropic vortices in $FeSe$ [40].

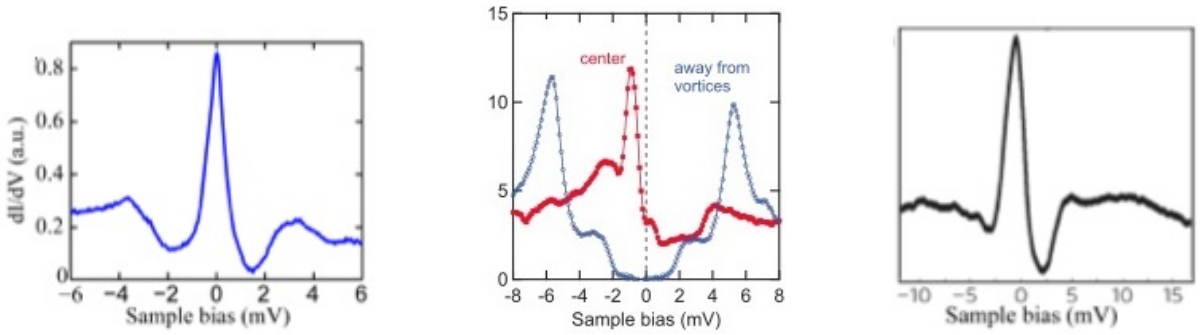

(a) (b) (c)

Figure 1.13: Vortex bound states. dI/dV spectra taken at the vortex center in (a) $FeSe$ [62], (b) $LiFeAs$ [28] and (c) $Ba_{0.6}K_{0.4}Fe_2As_2$ [40].

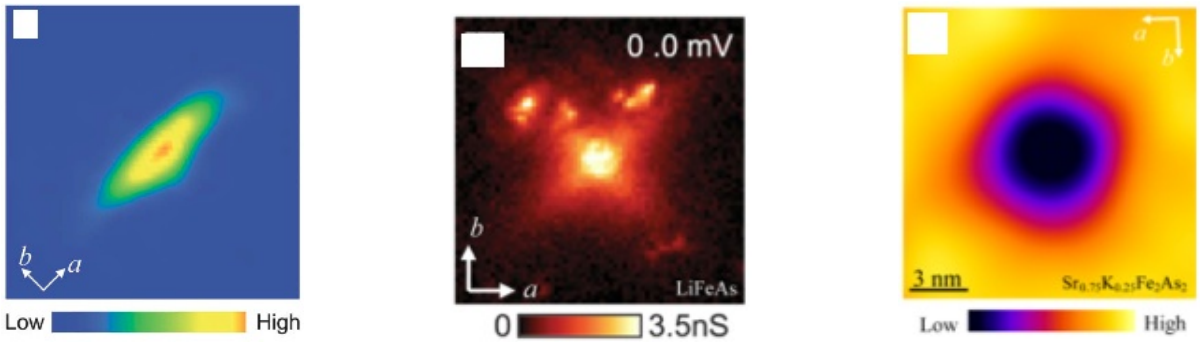

(a) (b) (c)

Figure 1.14: Vortex structure in (a) $FeSe$ [40], (b) $LiFeAs$ [28](c) $Sr_{0.75}K_{0.25}Fe_2As_2$ [17].

Chapter 2

Five-orbital model

Density functional theory (DFT) is the standard modeling method used to calculate the electronic structures of many materials, including the FeSC superconductors. Within DFT, interactions cannot be included exactly and several approximate schemes exist. In the case of FeSC, DFT calculations actually give a Fermi surface and band structure that seems to be in reasonable agreement with many experiments. These calculations have shown that the spectral weight near the Fermi level is mainly coming from Fe states, and that the states belonging to other elements are 2 eV below the Fermi level as shown in Fig. 2.1.

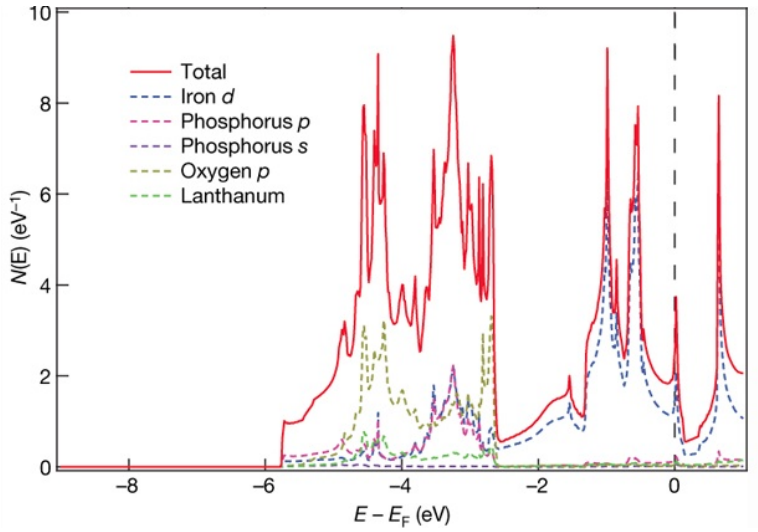

Figure 2.1: LDA DOS calculation for LaOFeP. The full red curve represents the total DOS. The Fe d-states (dashed blue line) dominate around E_F, whereas the rest of the states (the other dashed curves) lie several eV below. Graphic taken from [13].

In our modeling below we restrict the theory to include only the Fe states, and use the quasi-2D nature of these systems to work with a 2D lattice where each site corresponds to one Fe atom. Exclusion of the pnictogen ions from the model naturally leads to the 1-Fe unit cell (see Section 1.3 in Chapter 1).

Because the Fermi surface consists of both hole and electron pockets, a minimal model must include both. In previous works, further assumptions have been done, reducing the number of orbitals in the model from five to two [73, 74, 66]. This approximation takes only the Fe d_{xz} and d_{yz} degenerate orbitals into account, which gives rise to the Fermi surface shown in Fig. 2.2(a). However, the two-orbital model has many disadvantages. It produces the wrong Fermi surface

with the larger hole pocket at (π, π) (see Fig. 2.2). In addition, the d_{xy} contribution along the Fermi surface is missing which appears to be important for the structure and modulation of the superconducting gap [49].

In our model, we include all five Fe orbitals: d_{xz}, d_{yz}, $d_{x^2-y^2}$, d_{xy} and $d_{3z^2-r^2}$.

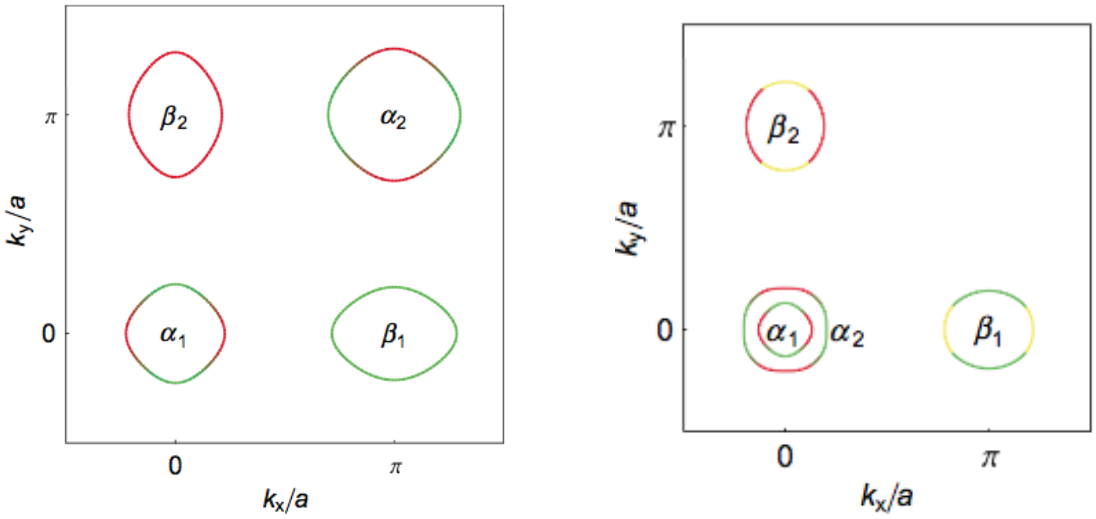

(a) (b)

Figure 2.2: Fermi surface with the main orbital contributions in the 1-Fe unit cell of a (a) two-orbital model and (b) five-orbital model. α_1 and α_2 represents the hole pockets and β_1 and β_2 the electron pockets. Note the position of the larger hole pocket α_2 at (π, π) in (a). After folding back to the 2-Fe zone, it is centered at (0,0), but the fact that α_1 and α_2 are not degenerate at (0,0) in the 1-Fe zone contradicts the symmetry of the DFT wave functions. In addition, the two-orbital model is missing the small d_{xy} patches at the tips of the electron pockets that exist in the five-orbital model. [red=d_{xz}, green=d_{yz} and yellow= d_{xy}]. Graphic taken from [59].

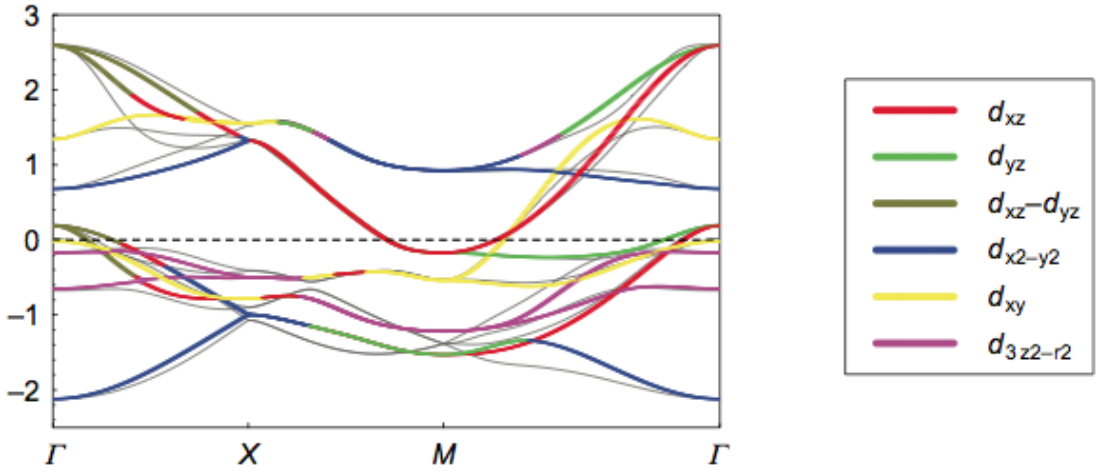

Figure 2.3: The band structure for the five-orbital model back folded to the 2-Fe zone. The main orbital contributions are shown by different colors. A substantial overlap between the orbitals can be seen. The gray lines show the DFT band structure to which the five-orbital model is fitted. Graphic taken from [59].

2.1 Hamiltonian

Our real-space five orbital Hubbard model Hamiltonian contains four terms: the kinetic energy term H_0, the number of particles operator H_N multiplied by the chemical potential, which is the term we introduce because we are working in the grand canonical ensemble, the Coulomb interaction term H_{int} containing the two-body onsite interactions between the electrons, the BCS term H_{BCS} which accounts for superconductivity and the Zeeman term H_Z which accounts for the potential energy of the electrons due to the interaction of the magnetic moment of the electrons with the external magnetic field,

$$H = H_0 + H_N + H_{int} + H_{BCS} + H_Z. \tag{2.1}$$

In the following sub-sections, we explain each term of this microscopic Hamiltonian.

2.1.1 Kinetic energy

The kinetic energy term is given by

$$H_0 = \sum_{ij,\mu\nu,\sigma} t_{ij}^{\mu\nu} e^{i\varphi_{ij}} \hat{c}_{i\mu\sigma}^{\dagger} \hat{c}_{j\nu\sigma} \tag{2.2}$$

where $\hat{c}_{i\mu\sigma}^{\dagger}(\hat{c}_{i\mu\sigma})$ creates (annihilates) an electron in site i, orbital μ and spin projection σ. The orbital indexes μ and ν run from 1 to 5 for d_{xz}, d_{yz}, $d_{x^2-y^2}, d_{xy}$ and $d_{3z^2-r^2}$. The hoppings $t_{ij}^{\mu\nu}$ are calculated from a fit to a DFT band structure. Depending on the material we study, we choose the hoppings such that we have the suitable band structure. This will be explained at the beginning of each chapter. $\varphi_{ij} = \frac{-e}{\hbar} \oint_j^i \mathbf{A} \cdot \mathbf{ds}$ is the Peierls phase which accounts for the magnetic field as explained in Chapter 3. All the band structures we use for the FeSC, contain hoppings up to fifth nearest neighbors. Therefore, we calculate the line-integral in the Peierls phase for five different hoppings, i.e. nearest, next nearest, third nearest, fourth nearest and fifth nearest neighbors.

2.1.2 Number of particles

Through out this work, we work in the grand canonical ensemble, thus apart from the kinetic energy and the interactions, the term H_N must be included in the Hamiltonian [30]

$$H_N = -\mu_0 \sum_{i\mu\sigma} \hat{n}_{i\mu\sigma}, \tag{2.3}$$

where $\hat{n}_{i\mu\sigma} = \hat{c}^\dagger_{i\mu\sigma}\hat{c}_{i\mu\sigma}$ is the number of particles operator.

We tune the chemical potential μ_0, such that we have the average number of particles we want.

2.1.3 Interactions

Since the $3d$ electrons are generally tightly bound, the crystallographic effects (the effects of the static electric field produced by the neighbor anions) of the interactions between them should be quite small. We neglect these effects, so that the interaction on site i is rotationally invariant and has the form $V(\mathbf{r},\mathbf{r}') = V(|\mathbf{r}-\mathbf{r}'|)$. Furthermore, because of the mentioned localization, inter-site interactions will be much weaker than the ones taking place at the same site, thus we only consider onsite Coulomb interactions. With $\Psi_{i\sigma}(\mathbf{r}) = \sum_\mu \phi_{i\mu}(\mathbf{r})\hat{c}_{i\mu\sigma}$ being the quantum field operator for an electron at lattice site i with spin projection σ, the general Coulomb interaction term of the Hamiltonian is

$$H_{int} = \frac{1}{2}\sum_i \sum_{\sigma\sigma'} \int d\mathbf{r}d\mathbf{r}' \Psi^\dagger_{i\sigma}(\mathbf{r})\Psi^\dagger_{i\sigma'}(\mathbf{r}')\frac{e_0^2}{|\mathbf{r}-\mathbf{r}'|}\Psi_{i\sigma'}(\mathbf{r}')\Psi_{i\sigma}(\mathbf{r}). \tag{2.4}$$

We assume the first quantization wave function to be a Hydrogen-like atomic orbital $\phi_{i\mu}(\mathbf{r}) = R_{32}(r)Y_{2\mu}(\Omega)$, where it has been used that the quantum numbers are $n=3$ and $l=2$ from the electronic configuration of Fe. The Coulomb interaction will then have the form

$$H_{int} = \frac{1}{2}\sum_i \sum_{\mu\nu\mu'\nu'} \sum_{\sigma\sigma'} V(\mu,\nu;\mu',\nu')\hat{c}^\dagger_{i\mu\sigma}\hat{c}^\dagger_{i\nu\sigma'}\hat{c}_{i\nu'\sigma'}\hat{c}_{i\mu'\sigma}, \tag{2.5}$$

with the matrix elements being

$$V(\mu,\nu;\mu',\nu') = \int d\mathbf{r}d\mathbf{r}' \phi^*_{i\mu}(\mathbf{r})\phi^*_{i\nu}(\mathbf{r}')\frac{e_0^2}{|\mathbf{r}-\mathbf{r}'|}\phi_{i\nu'}(\mathbf{r}')\phi_{i\mu'}(\mathbf{r}). \tag{2.6}$$

In this expression $\mu,\ \nu,\ \mu'$ and ν' refer to azimuthal quantum numbers of $l=2$ spherical harmonics for Fe d-states. The main contribution arises from elements involving just two different orbitals. Those matrix elements give rise to four different kind of terms:

$$H^{(1)}_{int} = U\sum_{i\mu} \hat{n}_{i\mu\uparrow}\hat{n}_{i\mu\downarrow} \tag{2.7}$$

$$H^{(2)}_{int} = U'\sum_{i,\mu<\nu,\sigma} (\hat{n}_{i\mu\sigma}\hat{n}_{i\nu\bar{\sigma}} + \hat{n}_{i\mu\sigma}\hat{n}_{i\nu\sigma}) \tag{2.8}$$

$$H^{(3)}_{int} = -J\sum_{i,\mu<\nu,\sigma} (\hat{n}_{i\mu\sigma}\hat{n}_{i\nu\sigma} + \hat{c}^\dagger_{i\mu\sigma}\hat{c}_{i\mu\bar{\sigma}}\hat{c}^\dagger_{i\nu\bar{\sigma}}\hat{c}_{i\nu\sigma}) \tag{2.9}$$

$$H^{(4)}_{int} = J'\sum_{i,\mu<\nu,\sigma} \hat{c}^\dagger_{i\mu\sigma}\hat{c}^\dagger_{i\mu\bar{\sigma}}\hat{c}_{i\nu\bar{\sigma}}\hat{c}_{i\nu\sigma} \tag{2.10}$$

The first two are direct integrals, $U = V(\mu,\mu;\mu,\mu)$ and $U' = V(\mu,\nu;\mu,\nu)$, and the last two are exchange integrals, $J = V(\mu,\nu;\nu,\mu)$ and $J' = V(\mu,\mu;\nu,\nu)$. A physical explanation for each term will be given later in this section. Rearranging the terms, we arrive to the multi-orbital Hubbard-type model:

$$\begin{aligned} H_{int} =& U\sum_{i\mu}\hat{n}_{i\mu\uparrow}\hat{n}_{i\mu\downarrow} + U'\sum_{i,\mu<\nu,\sigma}\hat{n}_{i\mu\sigma}\hat{n}_{i\nu\bar{\sigma}} + (U'-J)\sum_{i,\mu<\nu,\sigma}\hat{n}_{i\mu\sigma}\hat{n}_{i\nu\sigma} \\ &+ J\sum_{i,\mu<\nu,\sigma}\hat{c}^{\dagger}_{i\mu\sigma}\hat{c}^{\dagger}_{i\nu\bar{\sigma}}\hat{c}_{i\mu\bar{\sigma}}\hat{c}_{i\nu\sigma} + J'\sum_{i,\mu<\nu,\sigma}\hat{c}^{\dagger}_{i\mu\sigma}\hat{c}^{\dagger}_{i\mu\bar{\sigma}}\hat{c}_{i\nu\bar{\sigma}}\hat{c}_{i\nu\sigma} \end{aligned} \tag{2.11}$$

.

From the symmetry of the spherical harmonics in the Coulomb matrix elements Eq.(2.6), the relations $U' = U - 2J$ and $J = J'$ hold [25]. These relations have also been explained as a spin and orbital rotational invariance [16]. One can rewrite the interaction Hamiltonian in terms of the orbital angular momentum and spin operators L^2 and S^2, except one term which is proportional to $(U - U' - 2J)$. The invariance condition then requires that $U - U' - 2J = 0$.

In order to have a physical idea of each term, we rearrange Eq.(2.11) in an alternative way

$$\begin{aligned} H_{int} =& U\sum_{i\mu}\hat{n}_{i\mu\uparrow}\hat{n}_{i\mu\downarrow} + (U'-\frac{J}{2})\sum_{i,\mu<\nu,\sigma}(\hat{n}_{i\mu\sigma}\hat{n}_{i\nu\bar{\sigma}} + \hat{n}_{i\mu\sigma}\hat{n}_{i\nu\sigma}) \\ &- 2J\sum_{i,\mu<\nu}\vec{S}_{i\mu}\cdot\vec{S}_{i\nu} + J'\sum_{i,\mu<\nu,\sigma}\hat{c}^{\dagger}_{i\mu\sigma}\hat{c}^{\dagger}_{i\mu\bar{\sigma}}\hat{c}_{i\nu\bar{\sigma}}\hat{c}_{i\nu\sigma} \end{aligned} \tag{2.12}$$

.

The first term accounts for the Coulomb interaction between electrons in the same orbital (intra-orbital interactions). The second term accounts for the Coulomb interaction between electrons in different orbitals (inter-orbital). The third term is a Hund's coupling interaction which, since $J > 0$, favors the parallel alignment of electron spins on the same site, and the last interaction term is the pair hopping energy J'. All these terms were generated from a multi-orbital Coulomb interaction between electrons on the same site.

2.1.4 BCS Hamiltonian

The term H_{BCS} accounts for superconductivity. Even if the BCS theory does not explain the origin of the pairing mechanism in FeSC (it is not driven by the exchange of phonons), it works quite well once the superconducting state is settled down. We assume that at low energies, superconductivity is adequately described by the BCS theory in FeSC, and include a BCS term in our Hamiltonian of the form,

$$H_{BCS} = -\sum_{ij,pqst}\Gamma^{st}_{pq}(r)\hat{c}^{\dagger}_{ip\uparrow}\hat{c}^{\dagger}_{jt\downarrow}\hat{c}_{js\downarrow}\hat{c}_{iq\uparrow}. \tag{2.13}$$

2.1.5 Zeeman

The term H_Z accounts for the potential energy of the electrons due to the interaction between the magnetic moments and the external magnetic field. By definition, $H_Z = -\boldsymbol{\mu}\cdot\mathbf{B}$. Now, $\boldsymbol{\mu} = -\frac{\mu_B g_s}{\hbar}\mathbf{S}$, where we assume that the only contribution to the magnetic moment comes from spin. Now if $\mathbf{B} = B(-\hat{\mathbf{k}})$, we only have S_z in the term and $S_{zi} = \frac{\hbar}{2}\sum_{\mu}(\hat{n}_{i\mu\uparrow} - \hat{n}_{i\mu\downarrow})$, hence

$$H_Z = \mathcal{Z}\sum_{\mu}(\hat{n}_{i\mu\uparrow} - \hat{n}_{i\mu\downarrow}). \tag{2.14}$$

Here, $\mathcal{Z} \equiv -\frac{\mu_B g_s B}{2}$, μ_B is the Bohr magneton and g_s the electron spin g-factor (also called dimensionless magnetic moment).

2.2 Mean Field treatment

Now that we have our model Hamiltonian, we can study it by the use of numerical methods. First, since it is not quadratic, we face the standard problem of interacting many-particle quantum mechanics. However, the evidence for weak-coupling of the FeSC systems motivates us to try and understand their behavior from this less correlated perspective. Thus, in the following we perform a mean-field decoupling of the quartic interaction terms H_{BCS} and H_{int}. We first decouple H_{int} in the density channel, after doing some algebra (see Appendix A.1),

$$H_{int}^{MF} = \sum_{i,\mu\neq\nu,\sigma} [U\langle\hat{n}_{i\mu\bar{\sigma}}\rangle + U'\langle\hat{n}_{i\nu\bar{\sigma}}\rangle + (U'-J)\langle\hat{n}_{i\nu\sigma}\rangle]\hat{n}_{i\mu\sigma} \tag{2.15}$$

where $\langle\hat{n}_{i\mu\sigma}\rangle$ is the average electron density. Second, we decouple H_{BCS} in the "Cooper" channel introducing a pairing field between different sites i (orbital μ) and j (orbital ν), assuming that in the superconducting state, the thermal average of the creation of a Cooper pair is non-zero. Hence, again doing some algebra (see Appendix A.1)

$$H_{BCS}^{MF} = -\sum_{ij,\mu\nu} (\Delta_{ij}^{\mu\nu}\hat{c}_{i\mu\uparrow}^{\dagger}\hat{c}_{j\nu\downarrow}^{\dagger} + H.c.) \tag{2.16}$$

where we define the superconducting order parameter (SCOP) as,

$$\Delta_{ij}^{\mu\nu} = \sum_{qs} \Gamma_{\mu q}^{s\nu}(r)\langle\hat{c}_{js\downarrow}\hat{c}_{iq\uparrow}\rangle. \tag{2.17}$$

Now, we have our quadratic mean field Hamiltonian

$$\begin{aligned} H^{MF} = &\sum_{ij,\mu\nu,\sigma} t_{ij}^{\mu\nu} e^{i\varphi_{ij}}\hat{c}_{i\mu\sigma}^{\dagger}\hat{c}_{j\nu\sigma} - \mu_0\sum_{i\mu\sigma}\hat{n}_{i\mu\sigma} \\ &+ \sum_{i,\mu\neq\nu,\sigma} [U\langle\hat{n}_{i\mu\bar{\sigma}}\rangle + U'\langle\hat{n}_{i\nu\bar{\sigma}}\rangle + (U'-J)\langle\hat{n}_{i\nu\sigma}\rangle]\hat{n}_{i\mu\sigma} \\ &- \sum_{ij,\mu\nu}[\Delta_{ij}^{\mu\nu}\hat{c}_{i\mu\uparrow}^{\dagger}\hat{c}_{j\nu\downarrow}^{\dagger} + H.c.] + \mathcal{Z}\sum_{\mu}(\hat{n}_{i\mu\uparrow} - \hat{n}_{i\mu\downarrow}). \end{aligned} \tag{2.18}$$

2.3 The Bogoliubov-de Gennes equations

Now that we have a Hamiltonian which is quadratic in the electron operators, it is possible to diagonalize it. To do so, we perform the spin generalized Bogoliubov transformation in the electron operators

$$\begin{aligned} \hat{c}_{i\mu\sigma} &= \sum_{n}(u_{i\mu\sigma}^{n}\hat{\gamma}_{n\sigma} + v_{i\mu\sigma}^{n*}\hat{\gamma}_{n\bar{\sigma}}^{\dagger}) \\ \hat{c}_{i\mu\sigma}^{\dagger} &= \sum_{n}(u_{i\mu\sigma}^{n*}\hat{\gamma}_{n\sigma}^{\dagger} + v_{i\mu\sigma}^{n}\hat{\gamma}_{n\bar{\sigma}}). \end{aligned} \tag{2.19}$$

Here, n is the index of eigenvalues and eigenvectors of the Hamiltonian. The diagonalized Hamiltonian is $H = GS + \sum_{n\sigma} E_{n\sigma}\hat{\gamma}^{\dagger}_{n\sigma}\hat{\gamma}_{n\sigma}$ and thus it only runs for those states which have positive energy.

Comparing $[H^{MF}, \hat{c}_{i\mu\sigma}]$ calculated by explicitly commuting H^{MF} (shown in Eq. (2.18)), to the one calculated using the Bogoliubov transformation, we arrive at the BdG equations,

$$\begin{pmatrix} \hat{H}_{\uparrow} & \hat{\Delta}^{\mu\nu}_{ij} \\ \hat{\Delta}^{\nu\mu *}_{ji} & -H^{*}_{\downarrow} \end{pmatrix} \begin{pmatrix} u^{n} \\ v^{n} \end{pmatrix} = E_{n\uparrow} \begin{pmatrix} u^{n} \\ v^{n} \end{pmatrix}, \tag{2.20}$$

where

$$\hat{H}_{\sigma} u_{i\mu} = \sum_{j\nu} t^{\mu\nu}_{ij} u^{n}_{j\nu} + \sum_{\nu(\nu\neq\mu)} (-\mu_0 + U n_{i\mu\bar{\sigma}} + U' n_{\nu\bar{\sigma}} + (U' - J) n_{i\nu\sigma}) u^{n}_{i\mu} + \mathcal{Z}\ u_{i\mu} \tag{2.21}$$

and

$$\hat{\Delta}^{\mu\nu}_{ij} = -\sum_{j\nu} \Delta^{\mu\nu}_{ij} u_{j\nu}. \tag{2.22}$$

The mean field quantities (self-consistent fields) can be expressed in terms of the eigenvalues and eigenvectors as (see Appendix A.3)

$$n_{i\mu\uparrow} = \sum_{l} |u^{l}_{i\mu\uparrow}|^2 f(E_l) \tag{2.23}$$

$$n_{i\mu\downarrow} = \sum_{l} |v^{l}_{i\mu\downarrow}|^2 (1 - f(E_l)) \tag{2.24}$$

$$\Delta^{\mu\nu}_{ij} = \sum_{qs} \Gamma_{\mu qs\nu}(r) \sum_{l} v^{l*}_{js\downarrow} u^{l}_{iq\uparrow} f(E_l) \tag{2.25}$$

where $f(E_n)$ is the Fermi distribution function. We usually drop the spin induces of $u^{l}_{i\mu\uparrow}$ and $v^{l}_{i\mu\downarrow}$ because they are not necessary. As one can see, the matrix Eq.(2.20) contains quantities that depend on the eigenvectors and eigenvalues. Thus, we calculate them self-consistently, i.e. we give an initial guess for the mean fields and then we calculate them iteratively until their value converge.

Once the self-consistent fields have converged, we can build the single-particle Greens function, $G^{R}_{i\sigma j\sigma'}(t) = -i\theta(-t\langle[\hat{c}_{i\mu\sigma}(0), \hat{c}^{\dagger}_{j\mu\sigma'}(t)]\rangle)$, from the eigenstates (u^n, v^n) and eigenvalues E_n,

$$G^{R}_{ij,\mu}(w) = \sum_{n\sigma} \left(\frac{u^{n}_{i\mu} u^{n*}_{j\mu}}{w - E_n + i\eta} + \frac{v^{n}_{i\mu} v^{n*}_{j\mu}}{w + E_n + i\eta} \right), \tag{2.26}$$

from which we obtain the expression of the orbital resolved local density of states (LDOS) $N_{i\mu}(w) = \frac{-1}{\pi} Im G^{R}_{ii,\mu}(w)$.

Chapter 3

Magnetic Field

When starting from a microscopical Hamiltonian, the introduction of the magnetic field is very tricky and one has to understand and treat very carefully the fact that the entrance of the B field through the vector potential, breaks the translational invariance of the Hamiltonian. Therefore, it is worth to devote an entire chapter to explain all the subtleties related to the treatment of the B field.

3.1 The Peierls phase

The way the magnetic field enters the Hamiltonian is through the Peierls phases in the kinetic energy term

$$H_0 = \sum_{ij,\sigma} t_{ij} e^{-i\frac{e}{\hbar}\oint_j^i \mathbf{A}\cdot\mathbf{ds}} \hat{c}^\dagger_{i\sigma}\hat{c}_{j\sigma}. \tag{3.1}$$

The Peierls phase in the hopping terms comes from the fact that the Lagrangian of an electron in a magnetic field contains a dynamical term $q\mathbf{v}\cdot\mathbf{A}$, which gives rise to the phase accumulation in the propagator of the electron describing the hopping process between two lattice sites.

From the path integrals formalism [4], we know that a quantum mechanical transition amplitude from site j at time t_j to site i at time t_i is given by

$$\langle \mathbf{r_i}, t_i | \mathbf{r_j}, t_j \rangle = \int_{\mathbf{r}(t_j)=\mathbf{r_j}}^{\mathbf{r}(t_i)=\mathbf{r_i}} \mathcal{D}[\mathbf{r}(t)] e^{\frac{i}{\hbar}S(\mathbf{r})}, \tag{3.2}$$

which is the sum the infinite paths from $\mathbf{r}(t_j)$ to $\mathbf{r}(t_i)$ and $S(\mathbf{r})$ is the classical action of each path. The Lagrangian that gives rise to the Lorentz force in the equations of motion is

$$L = L^{(0)} + q\mathbf{v}\cdot\mathbf{A}, \tag{3.3}$$

where $L^{(0)}$ is the Lagrangian in the absence of a B field. The corresponding action $S = \int_{t_j}^{t_i} dt' L$ reads

$$S(\mathbf{r_i}, \mathbf{r_j}) = S^{(0)}(\mathbf{r_i}, \mathbf{r_j}) + q\int_{t_j}^{t_i} dt \left(\frac{\mathbf{dr}}{dt}\right)\cdot\mathbf{A} = S^{(0)}(\mathbf{r_i}, \mathbf{r_j}) + q\int_{\mathbf{r_j}}^{\mathbf{r_i}} \mathbf{A}\cdot\mathbf{dr} \tag{3.4}$$

Now, if we ignore all the possible paths but the one joining i and j by a straight line and denote the differential line element of the path $\mathbf{ds}$,

$$S(\mathbf{r_i}, \mathbf{r_j}) = S^{(0)}(\mathbf{r_i}, \mathbf{r_j}) + q\oint_{r_j}^{\mathbf{r_i}} \mathbf{A}\cdot\mathbf{ds}. \tag{3.5}$$

Thus, we conclude that the transition amplitude corresponding to having an external B field is simply, the one in the absence of B, times a phase

$$\langle \mathbf{r_i}, t_i | \mathbf{r_j}, t_j \rangle = \int_{\mathbf{r}(t_j)=\mathbf{r_j}}^{\mathbf{r}(t_i)=\mathbf{r_i}} \mathcal{D}[\mathbf{r}(t)] e^{\frac{i}{\hbar} S^{(0)}(\mathbf{r_i},\mathbf{r_j})} . \underbrace{e^{i\frac{q}{\hbar}\oint_{\mathbf{r_j}}^{\mathbf{r_i}} \mathbf{A}\cdot\mathbf{ds}}}_{Peierls\ phase} . \tag{3.6}$$

This phase is the so called Peirels phase.

3.2 Magnetic Translations

When an external magnetic field is present, this enters in the Hamiltonian through the vector potential $\mathbf{A}(\mathbf{r})$. Because of its presence, the Hamiltonian does not commute with the usual translation operators, regardless of its symmetries. Evenso, it is possible to find a new operator called the *Magnetic Translation Operator* (MTO) which commutes with lattice periodic Hamiltonians [71].

Let us take the simplest case of spinless electrons in a 2D square lattice with an external homogeneous magnetic field $\mathbf{B} = \nabla \times \mathbf{A}$, described by the tight-binding Hamiltonian with nearest-neighbor hopping (for convenience, we explicitly write the x and y coordinates of each site, opposite to the previous section where we used the i,j notation)

$$H_0 = \sum_{m,n} t e^{i\varphi^x_{m,n}} \hat{c}^\dagger_{m+1,n} \hat{c}_{m,n} + t e^{i\varphi^y_{m,n}} \hat{c}^\dagger_{m,n+1} \hat{c}_{m,n}, \tag{3.7}$$

where (m, n) correspond to the x and y coordinates respectively, and the phases are the Peierls phases given by

$$\varphi^x_{m,n} = \frac{-\pi}{\Phi_0} \oint_m^{m+1} \mathbf{A}\cdot\mathbf{dr}, \quad \varphi^y_{m,n} = \frac{-\pi}{\Phi_0} \oint_n^{n+1} \mathbf{A}\cdot\mathbf{dr} \tag{3.8}$$

where $\Phi_0 = h/2e$ is the half flux quantum.

Let's define the lattice derivatives as

$$\Delta_x f_{m,n} = f_{m+1,n} - f_{m,n}, \quad \Delta_y f_{m,n} = f_{m,n+1} - f_{m,n} \tag{3.9}$$

The lattice curl of the Peierls phases is related to the flux per plaquette $\phi_{m,n}$

$$\nabla_{m,n} \cdot (\varphi^y_{m,n}, \varphi^x_{m,n}) = \Delta_x \varphi^y_{m,n} - \Delta_y \varphi^x_{m,n} = \frac{-\pi}{\Phi_0} \oint_{unitcell} \mathbf{A}\cdot\mathbf{dl} = \frac{-\pi}{\Phi_0} \oint_{unitcell} \mathbf{B}\cdot\mathbf{dS} = -\pi \frac{\Phi_{unitcell}}{\Phi_0} = -\pi\phi_{mn} \tag{3.10}$$

Let us show now that the Hamiltonian does not commute with the usual translation operator $T_{\mathbf{R}} = \sum_{\mathbf{r}} \hat{c}^\dagger_{\mathbf{r}+\mathbf{R}} \hat{c}_{\mathbf{r}}$. In order to do that, we look at the x part of the Hamiltonian:

$$
\begin{aligned}
&[H_x, T_x] = [\sum_{mn} t e^{i\varphi^x_{m,n}} \hat{c}^\dagger_{m+1,n}\hat{c}_{m,n}, \sum_{ij} \hat{c}^\dagger_{i+1,j}\hat{c}_{i,j}] = \\
&\sum_{mn,ij} t e^{i\varphi^x_{m,n}} [\hat{c}^\dagger_{m+1,n}\hat{c}_{m,n}, \hat{c}^\dagger_{i+1,j}\hat{c}_{i,j}] = \\
&\sum_{mn,ij} t e^{i\varphi^x_{m,n}} (\hat{c}^\dagger_{i+1,j}[\hat{c}^\dagger_{m+1,n}\hat{c}_{m,n}, \hat{c}_{i,j}] + [\hat{c}^\dagger_{m+1,n}\hat{c}_{m,n}, \hat{c}^\dagger_{i+1,j}]\hat{c}_{i,j}) = \\
&\sum_{mn,ij} t e^{i\varphi^x_{m,n}} (-\hat{c}^\dagger_{i+1,j}\hat{c}_{m,n}\delta_{i,m+1}\delta_{n,j} + \hat{c}^\dagger_{m+1,n}\hat{c}_{i,j}\delta_{m,i+1}\delta_{n,j}) = \\
&-\sum_{ij} t e^{i\varphi^x_{i-1,j}} \hat{c}^\dagger_{i+1,j}\hat{c}_{i-1,j} + \sum_{ij} t e^{i\varphi^x_{i+1,j}} \hat{c}^\dagger_{i+2,j}\hat{c}_{i,j} = \\
&\sum_{ij} t(e^{i\varphi^x_{i,j}} - e^{i\varphi^x_{i-1,j}}) \hat{c}^\dagger_{i+1,j}\hat{c}_{i-1,j} \neq 0
\end{aligned}
\tag{3.11}
$$

and similarly for the y part. As it has been shown, the presence of the Peierls phases makes the Hamiltonian not commute with the usual translation operator.

Let us find the new translation operator that commutes with the Hamiltonian. It has to be an one-body operator because the Hamiltonian is an one-body operator. So, let's begin with MTOs which correspond to translations by one lattice constant and define them as

$$
M_x = \sum_{mn} e^{i\chi^x_{m,n}} \hat{c}^\dagger_{m+1,n}\hat{c}_{m,n} \quad , \quad M_y = \sum_{mn} e^{i\chi^y_{m,n}} \hat{c}^\dagger_{m,n+1}\hat{c}_{m,n}. \tag{3.12}
$$

We now determine $\chi_{m,n}$ by requiring that $[H, M] = 0$,

$$
\begin{aligned}
&[H_x, M_x] = [\sum_{mn} t e^{i\varphi^x_{m,n}} \hat{c}^\dagger_{m+1,n}\hat{c}_{m,n}, \sum_{ij} e^{i\chi^x_{i,j}} \hat{c}^\dagger_{i+1,j}\hat{c}_{i,j}] = \\
&\sum_{mn,ij} t e^{i(\varphi^x_{m,n}+\chi^x_{i,j})} [\hat{c}^\dagger_{m+1,n}\hat{c}_{m,n}, \hat{c}^\dagger_{i+1,j}\hat{c}_{i,j}] = \\
&\sum_{mn,ij} t e^{i(\varphi^x_{m,n}+\chi^x_{i,j})} (\hat{c}^\dagger_{i+1,j}[\hat{c}^\dagger_{m+1,n}\hat{c}_{m,n}, \hat{c}_{i,j}] + [\hat{c}^\dagger_{m+1,n}\hat{c}_{m,n}, \hat{c}^\dagger_{i+1,j}]\hat{c}_{i,j}) = \\
&-\sum_{mn} t e^{i(\varphi^x_{m,n}+\chi^x_{m+1,n})} \hat{c}^\dagger_{m+2,n}\hat{c}_{m,n} + \sum_{mn} t e^{i(\varphi^x_{m,n}+\chi^x_{m-1,n})} \hat{c}^\dagger_{m+1,n}\hat{c}_{m-1,n} = \\
&\sum_{mn} t(e^{i(\varphi^x_{m+1,n}+\chi^x_{m,n})} - e^{i(\varphi^x_{m,n}+\chi^x_{m+1,n})}) \hat{c}^\dagger_{m+2,n}\hat{c}_{m,n},
\end{aligned}
\tag{3.13}
$$

and this is zero if

$$
\begin{aligned}
\varphi^x_{m+1,n} + \chi^x_{m,n} &= \varphi^x_{m,n} + \chi^x_{m+1,n}, \\
\Delta_x \chi^x_{m,n} &= \Delta_x \varphi^x_{m,n}.
\end{aligned}
\tag{3.14}
$$

We also require $[H_y, M_x] = 0$,

$$[H_y, M_x] = [\sum_{mn} te^{i\varphi^y_{m,n}} \hat{c}^\dagger_{m,n+1}\hat{c}_{m,n}, \sum_{ij} e^{i\chi^x_{i,j}} \hat{c}^\dagger_{i+1,j}\hat{c}_{i,j}] =$$
$$\sum_{mn,ij} te^{i(\varphi^y_{m,n}+\chi^x_{i,j})}[\hat{c}^\dagger_{m,n+1}\hat{c}_{m,n}, \hat{c}^\dagger_{i+1,j}\hat{c}_{i,j}] =$$
$$\sum_{mn,ij} te^{i(\varphi^y_{m,n}+\chi^x_{i,j})}(\hat{c}^\dagger_{i+1,j}[\hat{c}^\dagger_{m,n+1}\hat{c}_{m,n}, \hat{c}_{i,j}] + [\hat{c}^\dagger_{m,n+1}\hat{c}_{m,n}, \hat{c}^\dagger_{i+1,j}]\hat{c}_{i,j}) =$$
$$-\sum_{mn} te^{i(\varphi^y_{m,n}+\chi^x_{m,n+1})}\hat{c}^\dagger_{m+1,n+1}\hat{c}_{m,n} + \sum_{mn} te^{i(\varphi^y_{m,n}+\chi^x_{m-1,n})}\hat{c}^\dagger_{m,n+1}\hat{c}_{m-1,n}$$
$$\sum_{mn} t(e^{i(\varphi^y_{m+1,n}+\chi^x_{m,n})} - e^{i(\varphi^y_{m,n}+\chi^x_{m,n+1})})\hat{c}^\dagger_{m+1,n+1}\hat{c}_{m,n},$$

therefore

$$\begin{aligned} \varphi^y_{m+1,n} + \chi^x_{m,n} &= \varphi^y_{m,n} + \chi^x_{m,n+1}, \\ \Delta_y \chi^x_{m,n} &= \Delta_x \varphi^y_{m,n}. \end{aligned} \tag{3.15}$$

By further requiring $[H_x, M_y] = [H_y, M_y] = 0$, we also get

$$\Delta_y \chi^y_{m,n} = \Delta_y \varphi^y_{m,n}, \tag{3.16}$$
$$\Delta_x \chi^y_{m,n} = \Delta_y \varphi^x_{m,n}. \tag{3.17}$$

Now, by using Eq.(3.10), the equations (3.15) and (3.17) can be rewritten as

$$\Delta_y \chi^x_{m,n} = \Delta_y \varphi^x_{m,n} - \pi\phi_{mn} = \Delta_y(\varphi^x_{m,n} - \pi\phi_{mn}n), \tag{3.18}$$
$$\Delta_x \chi^y_{m,n} = \Delta_x \varphi^y_{m,n} + \pi\phi_{mn} = \Delta_x(\varphi^y_{m,n} + \pi\phi_{mn}m). \tag{3.19}$$

Thus,

$$\chi^x_{m,n} = \varphi^x_{m,n} - \pi\phi_{mn}n, \tag{3.20}$$

$$\chi^y_{m,n} = \varphi^y_{m,n} + \pi\phi_{mn}m. \tag{3.21}$$

We have found operators that commute with the Hamiltonian, but in general, two MTOs do not commute. We can easily verify that by acting on single particle states

$$M_x M_y c^\dagger_{mn}|0\rangle = M_x \sum_{ij} e^{i\chi^y_{i,j}} \hat{c}^\dagger_{i,j+1}\hat{c}_{i,j}c^\dagger_{mn}|0\rangle = M_x e^{i\chi^y_{m,n}}\hat{c}^\dagger_{m,n+1}|0\rangle =$$
$$\sum_{ij} e^{i\chi^x_{i+1,j}}\hat{c}^\dagger_{i,j}\hat{c}_{i,j}\hat{c}^\dagger_{m,n+1}|0\rangle = e^{i(\chi^x_{m,n+1}+\chi^y_{m,n})}\hat{c}^\dagger_{m+1,n+1}|0\rangle, \tag{3.22}$$

and

$$M_y M_x \hat{c}^\dagger_{mn}|0\rangle = e^{i(\chi^y_{m+1,n}+\chi^x_{m,n})}\hat{c}^\dagger_{m+1,n+1}|0\rangle =$$
$$e^{i(\chi^x_{m,n+1}+\chi^y_{m,n})}e^{-i(\chi^x_{m,n+1}+\chi^y_{m,n}-\chi^x_{m,n}-\chi^y_{m+1,n})}\hat{c}^\dagger_{m+1,n+1}|0\rangle, \tag{3.23}$$

and by use of equations (3.20), (3.21) and (3.10) (we drop the m and n indices of ϕ_{mn})

$$\chi^x_{m,n+1} + \chi^y_{m,n} - \chi^x_{m,n} - \chi^y_{m+1,n} = -\varphi^y_{m+1,n} + \varphi^y_{m,n} + \varphi^x_{m,n+1} - \varphi^x_{m,n} - 2\pi\phi = -\pi\phi. \quad (3.24)$$

Thus

$$M_x M_y = e^{-i\pi\phi} M_y M_x, \quad (3.25)$$

and by applying M_x q times

$$M_x^q M_y = e^{-i\pi\phi q} M_y M_x^q. \quad (3.26)$$

In general, no power of the MTOs commute. However, there is a special case where $\phi = 2p/q$ is a rational number, where they do commute. Then, I may define a new unit cell called the Magnetic unit cell(MUC) which is q times larger in the x direction than the usual unit cell and it is penetrated by an integer number of $2p$ half flux quantums Φ_0. Once we choose the pair of MTOs in the x and y directions, we fix the flux ϕ so that they commute. The choice of the couple of the MTOs, fixes the size of MUC, for example, if we analogously apply M_x q times and M_y q' times, we get

$$M_x^q M_y^{q'} = e^{-i\pi\phi qq'} M_y^{q'} M_x^q. \quad (3.27)$$

then the MTOs will commute for $\phi = 2p/qq'$ and the MUC will be q times larger in the x direction and q' in the y direction. The MUC will be penetrated by $2p$ half flux quantums again.

Thus, the translations under which the MTOs commute with each other and the Hamiltonian, are those which are composed of the primitive vectors of the MUC, thus, $\mathbf{R}_m = m_x\mathbf{b_x} + m_y\mathbf{b_y} = (R^x_m, R^y_m)$ with m_x, m_y integers, $\mathbf{b_i}$ being the primitive vectors of the MUC. We are free to choose the MUC but then we need to fix the flux accordingly.

These MTOs also fulfill the composition law $M_{\mathbf{R}_m} M_{\mathbf{R}_n} = M_{\mathbf{R}_m+\mathbf{R}_n}$. In order to show that, in the following derivation, we stick to $\mathbf{b_x} = q\mathbf{a_x}$ and $\mathbf{b_y} = \mathbf{a_y}$ for simplicity and we choose the Landau gauge $\mathbf{A} = (-By, 0)$. For this choice, the Peierls phases in Eq. (3.8) become

$$\varphi^x_{m,n} = 0, \quad \varphi^y_{m,n} = \pi\phi_{mn}, \quad (3.28)$$

which gives (see equations (3.20) and (3.21)),

$$\chi^x_{m,n} = 0, \quad (3.29)$$
$$\chi^y_{m,n} = \pi\phi_{mn} m. \quad (3.30)$$

and thus (see Eq. (3.12))

$$M_x = \sum_{mn} \hat{c}^\dagger_{m+1,n}\hat{c}_{m,n} \ , \quad M_y = \sum_{mn} e^{i\pi\phi m}\hat{c}^\dagger_{m,n+1}\hat{c}_{m,n}. \quad (3.31)$$

By acting with products of MTOs (Eq.(3.31)) on the single particle states, one can verify that

$$M_x^q = M_{qx} = \sum_{mn} \hat{c}^\dagger_{m+q,n}\hat{c}_{m,n}, \quad (3.32)$$
$$M_y^q = M_{qy} = \sum_{mn} e^{i\pi\phi qm}\hat{c}^\dagger_{m,n+q}\hat{c}_{m,n}. \quad (3.33)$$

Now, let us define the vectors $\mathbf{R}_m = m_x(q\mathbf{a}_x) + m_y\mathbf{a}_y$ and $\mathbf{R}_n = n_x(q\mathbf{a}_x) + n_y\mathbf{a}_y$. By acting on single particle states

$$M_{\mathbf{R}_m}\hat{c}^\dagger_{i,j}|0\rangle = M_y^{m_y}M_x^{qm_x}\hat{c}^\dagger_{i,j}|0\rangle = M_y^{m_y}\hat{c}^\dagger_{i+qm_x,j}|0\rangle = e^{i\pi\phi m_y(i+qm_x)}\hat{c}^\dagger_{i+qm_x,j+m_y}|0\rangle = e^{i\pi\phi m_y i}\hat{c}^\dagger_{i+qm_x,j+m_y}|0\rangle, \tag{3.34}$$

$$\begin{aligned} M_{\mathbf{R}_n}M_{\mathbf{R}_m}\hat{c}^\dagger_{i,j}|0\rangle = & \\ & M_{\mathbf{R}_n}e^{i\pi\phi m_y(i+qm_x)}\hat{c}^\dagger_{i+qm_x,j+m_y}|0\rangle = M_y^{n_y}e^{i\pi\phi m_y(i+qm_x)}\hat{c}^\dagger_{i+q(m_x+n_x),j+m_y}|0\rangle = \\ & \sum_{mn} e^{i\pi\phi n_y m}\hat{c}^\dagger_{m,n+n_y}\hat{c}_{m,n}e^{i\pi\phi m_y i}\hat{c}^\dagger_{i+q(n_x+m_x),j+m_y}|0\rangle = \\ & e^{i\pi\phi(n_y+m_y)i}\hat{c}^\dagger_{i+q(n_x+m_x),j+(n_y+m_y)}|0\rangle = M_{\mathbf{R}_n+\mathbf{R}_m}\hat{c}^\dagger_{i,j}|0\rangle. \end{aligned} \tag{3.35}$$

Hence we conclude that

$$M_{\mathbf{R}_n}M_{\mathbf{R}_m} = M_{\mathbf{R}_n+\mathbf{R}_m}. \tag{3.36}$$

This equation defines the group multiplication in the group of the magnetic translations. Then we can get the vector representation for the magnetic translation group. The representation matrix, which is one dimensional and very similar to the usual translation group, reads [23, 55]

$$D^{\mathbf{k}}(\mathbf{R}_m) = e^{-i\mathbf{k}\cdot\mathbf{R}_m}, \tag{3.37}$$

where

$$\mathbf{k} = \sum_i \frac{l_i}{N_i}\left(\frac{2\pi}{\mathrm{a}_i}\right)\hat{\mathbf{k}}_\mathbf{i}, \quad 0 \le l_i \le N_i - 1 \ (i = x, y). \tag{3.38}$$

Here $\hat{\mathbf{k}}_i$ are the reciprocal unit vectors and N_i are the number of lattice points in each direction of the finite crystal satisfying the periodic boundary conditions, i.e. the MUC, in our case $N_x = q$ and $N_y = 1$.

Let's denote the common eigenstates of the Hamiltonian and the MTOs (which we call the magnetic Bloch functions) $|\psi_\mathbf{k}\rangle$. Then, the generalized Bloch theorem is (we act on the ket)

$$\langle\mathbf{r}|M_{\mathbf{R}_m}|\psi_\mathbf{k}\rangle = \langle\mathbf{r}|e^{-i\mathbf{k}\cdot\mathbf{R}_m}|\psi_\mathbf{k}\rangle = e^{-i\mathbf{k}\cdot\mathbf{R}_m}\psi_k(\mathbf{r}) \tag{3.39}$$

where $|\mathbf{r}\rangle = \hat{c}^\dagger_{i,j}|0\rangle$. Now, from Eq.(3.34), we also have (we act on the bra)

$$\langle\mathbf{r}|M_{\mathbf{R}_m}|\psi_\mathbf{k}\rangle = \langle\mathbf{r}-\mathbf{R}_m|e^{i\pi\phi R_m^y x}|\psi_\mathbf{k}\rangle = e^{i\pi\phi R_m^y x}\psi_k(\mathbf{r}-\mathbf{R}_m), \tag{3.40}$$

where we used that $(\mathbf{M}_{\mathbf{R_m}}|\mathbf{r}\rangle = |\mathbf{r}'\rangle \ \Leftrightarrow \ \langle\mathbf{r}|\mathbf{M}^\dagger_{\mathbf{R_m}} = \langle\mathbf{r}'|)$.

Therefore, the way the eigenfunctions transform under spacial translations is

$$\psi_k(\mathbf{r}+\mathbf{R}_m) = e^{i\mathbf{k}\cdot\mathbf{R}_m}e^{i\pi\phi R_m^y x}\psi_k(\mathbf{r}) = e^{i\mathbf{k}\cdot\mathbf{R}_m}e^{-i\frac{\pi}{\Phi_0}\mathbf{A}(\mathbf{R_m})\cdot\mathbf{r}}\psi_k(\mathbf{r}) \equiv e^{-i\chi(\mathbf{r},\mathbf{R_m})/2}\psi_k(\mathbf{r}), \tag{3.41}$$

where we defined $\chi(\mathbf{r},\mathbf{R_m}) \equiv \frac{2\pi}{\Phi_0}\mathbf{A}(\mathbf{R_m})\cdot\mathbf{r}$. This result is completely general, and generalizes to any choice of MUC.

In our calculations, we always choose our MUC to be the whole system and fix the flux to two half flux quantum ($\Phi = 2\Phi_0$). This is done because we are interested in having realistic magnetic fields. For a five-band model, it is computationally unaffordable to use a realistic field (note that, since the flux is fixed, low magnetic field means big system and the other way around), it is usually much larger.

3.2.1 Generalization to the superconducting state

If we now include superconductivity, the Hamiltonian becomes (we return to i,j notation)

$$H = \sum_{ij} t_{ij} e^{i\varphi_{i,j}} \hat{c}_i^\dagger \hat{c}_j + \sum_{ij} (\Delta_{ij} \hat{c}_i^\dagger \hat{c}_j^\dagger + H.c.). \tag{3.42}$$

which written in the BdG form reads

$$H = \begin{pmatrix} H_0 & \Delta_{ij} \\ \Delta_{ji}^* & -H_0^* \end{pmatrix}. \tag{3.43}$$

The eigenstates of the Hamiltonian are the Bogoliubov quasiparticles and have two components,

$$\hat{\psi}(\mathbf{r}) = \begin{pmatrix} u(\mathbf{r}) \\ v(\mathbf{r}) \end{pmatrix}. \tag{3.44}$$

The SCOP transforms as

$$\Delta(\mathbf{r} + \mathbf{R_m}) = \Delta_{i+\mathbf{R_m}, j+\mathbf{R_m}} = e^{-i\chi(\mathbf{r},\mathbf{R_m})} \Delta(\mathbf{r}). \tag{3.45}$$

In order to apply the idea of the magnetic translations group derived above, we introduce the magnetic translation operators for the Bogoliubov quasiparticles in the vortex lattice as follows [23]

$$\mathcal{T}_{\mathbf{R_m}} \hat{\psi}(\mathbf{r}) = e^{-i\frac{1}{2}\chi(\mathbf{r},\mathbf{R_m})\sigma_z} \hat{\psi}(\mathbf{r} - \mathbf{R_m}), \tag{3.46}$$

where σ_z is the third Pauli matrix. This operator commutes with the Hamiltonian and fulfills the composition law

$$\mathcal{T}_{\mathbf{R}_n} \mathcal{T}_{\mathbf{R}_m} = \mathcal{T}_{\mathbf{R}_n + \mathbf{R}_m}. \tag{3.47}$$

Thus, the eigenstates of H are Blochlike and are characterized by a quantum number $\mathbf{k}$. Hence, similar to Eq.(3.41), it is possible to formulate the generalized Bloch theorem for the Bogoliubov states

$$\begin{pmatrix} u_k(\mathbf{r} + \mathbf{R_m}) \\ v_k(\mathbf{r} + \mathbf{R_m}) \end{pmatrix} = e^{i\mathbf{k}\cdot\mathbf{R}_m} \begin{pmatrix} e^{-i\chi(\mathbf{r},\mathbf{R_m})/2} u_k(\mathbf{r}) \\ e^{i\chi(\mathbf{r},\mathbf{R_m})/2} v_k(\mathbf{r}) \end{pmatrix}. \tag{3.48}$$

Since we will be working in the superconducting state, this is the relation we will use in our boundary conditions in all the calculations where there is a magnetic field,

3.3 Gauge invariance of the theory

The importance of gauge invariance has long be recognized. Right after the development of quantum mechanics, the Schrödinger equation was shown by Fock to be invariant under local gauge transformations.

In this chapter, we show that our theory, in which we introduce the magnetic field through the Peierls phases, is gauge invariant. The gauge invariance was a source of confusion for us, until we cleared it out.

Let us start from the Hamiltonian

$$H = \sum_{ij} t_{ij} e^{-i\frac{e}{\hbar}\oint_j^i \mathbf{A}\cdot\mathbf{ds}} \hat{c}_i^\dagger \hat{c}_j + V_0 \sum_i (\langle \hat{c}_i \hat{c}_i \rangle_H \hat{c}_i^\dagger \hat{c}_i^\dagger + H.c.), \tag{3.49}$$

where we only consider onsite superconductivity for simplicity and $\langle \hat{c}_i \hat{c}_i \rangle_H$ is the thermal average with respect to H. If we now perform the following gauge transformation

$$\mathbf{A} \to \mathbf{A}' = \mathbf{A} - \nabla\Lambda, \tag{3.50}$$

$$\hat{c}_i \to \hat{c}'_i = e^{i\frac{e}{\hbar}\Lambda_i} \hat{c}_i \tag{3.51}$$

then we have for the gauge transformed H'

$$\begin{aligned}
H' &= \sum_{ij} t_{ij} e^{-i\frac{e}{\hbar}\oint_j^i \mathbf{A}'\cdot\mathbf{ds}} \hat{c}'^\dagger_i \hat{c}'_j + V_0 \sum_i (\langle \hat{c}'_i \hat{c}'_i \rangle_{H'} \hat{c}'^\dagger_i \hat{c}'^\dagger_i + H.c.) \\
&= \sum_{ij} t_{ij} e^{-i\frac{e}{\hbar}(\oint_j^i \mathbf{A}'\cdot\mathbf{ds} + \Lambda_i - \Lambda_j)} \hat{c}_i^\dagger \hat{c}_j + V_0 \sum_i (\langle \hat{c}_i \hat{c}_i \rangle_{H'} \hat{c}_i^\dagger \hat{c}_i^\dagger + H.c.) \\
&= \sum_{ij} t_{ij} e^{-i\frac{e}{\hbar}(\oint_j^i \mathbf{A}'\cdot\mathbf{ds} + (\oint_j^i \nabla\Lambda\cdot\mathbf{ds}))} \hat{c}_i^\dagger \hat{c}_j + V_0 \sum_i (\langle \hat{c}_i \hat{c}_i \rangle_{H'} \hat{c}_i^\dagger \hat{c}_i^\dagger + H.c.) \\
&= \sum_{ij} t_{ij} e^{-i\frac{e}{\hbar}\oint_j^i (\mathbf{A}'+\nabla\Lambda)\cdot\mathbf{ds}} \hat{c}_i^\dagger \hat{c}_j + V_0 \sum_i (\langle \hat{c}_i \hat{c}_i \rangle_{H'} \hat{c}_i^\dagger \hat{c}_i^\dagger + H.c.) \\
&= \sum_{ij} t_{ij} e^{-i\frac{e}{\hbar}\oint_j^i \mathbf{A}\cdot\mathbf{ds}} \hat{c}_i^\dagger \hat{c}_j + V_0 \sum_i (\langle \hat{c}_i \hat{c}_i \rangle_{H'} \hat{c}_i^\dagger \hat{c}_i^\dagger + H.c.) \\
&= \sum_{ij} t_{ij} e^{-i\frac{e}{\hbar}\oint_j^i \mathbf{A}\cdot\mathbf{ds}} \hat{c}_i^\dagger \hat{c}_j + V_0 \sum_i (\langle \hat{c}_i \hat{c}_i \rangle_H \hat{c}_i^\dagger \hat{c}_i^\dagger + H.c.) \\
&= H.
\end{aligned} \tag{3.52}$$

Thus, it has been shown that our theory is gauge invariant.

Even though it is naturally deduced above, we should remind ourselves that (because it was source of confusion for us), when superconductivity is introduced to the Hamiltonian, the result should not be the same for two different gauges after one single iteration, unless we gauge transform $\Delta_i = \langle \hat{c}_i \hat{c}_i \rangle_H$ as well.

Let's take the simplest case where the SCOP is homogeneous in space and thus $\Delta_i = \Delta$. We now define $H(\mathbf{A}^1, \Delta^1)$ and $H(\mathbf{A}^2, \Delta^2)$, where

$$H(\mathbf{A}, \Delta) = \sum_{ij} t_{ij} e^{-i\frac{e}{\hbar}\oint_j^i \mathbf{A}\cdot\mathbf{ds}} \hat{c}_i^\dagger \hat{c}_j + V_0 \sum_i (\Delta \hat{c}_i^\dagger \hat{c}_i^\dagger + H.c.), \tag{3.53}$$

and

$$\mathbf{A^2} = \mathbf{A^1} - \nabla\Lambda. \tag{3.54}$$

We now diagonalize this Hamiltonian and get the set of eigenvalues ϵ_1 and ϵ_2, corresponding to $H(\mathbf{A}^1, \Delta^1)$ and $H(\mathbf{A}^2, \Delta^2)$ respectively. So, ϵ_1 and ϵ_2 will be the same, only if

$$\Delta^2 = \Delta^1 e^{i\frac{2e}{\hbar}\Lambda}. \tag{3.55}$$

3.4 Electrons in a 2D lattice with a perpendicular uniform magnetic field

In this section, we analyze the kinetic energy term in the presence of a magnetic field, which will allow us to understand some of the later calculations. Thus we diagonalize

$$H_0 = \sum_{ij} t_{ij} e^{-i\frac{e}{\hbar}\oint_j^i \mathbf{A}\cdot\mathbf{ds}} \hat{c}_i^\dagger \hat{c}_j. \tag{3.56}$$

As shown in Fig. 3.1, the square of the modulus of the eigenstates of H_0 are not homogeneous in space. We also find this in the absence of the magnetic field, but in this case ($B = 0T$), the eigenstates are degenerate in such a way that, the sum of the square of all the states corresponding to a same eigenenergy, gives an homogeneous distribution in space. In the presence of a magnetic field, in case we choose the MUC to be the whole system (which implies that the eigenstates of the system are characterized by a single $\mathbf{k}$ vector which is zero), as we usually do, the eigenstates of H_0 are not degenerate. As a consequence, since the electron density is just the sum of the states multiplied by the Fermi function ($n_i = \sum_n |\psi_i^n|^2 f(E_n)$), in general, n_i will not be homogeneous in the presence of a magnetic field, for example see Fig. 3.1(d). This modulation of the densities decreases quite rapidly as the system size is increased.

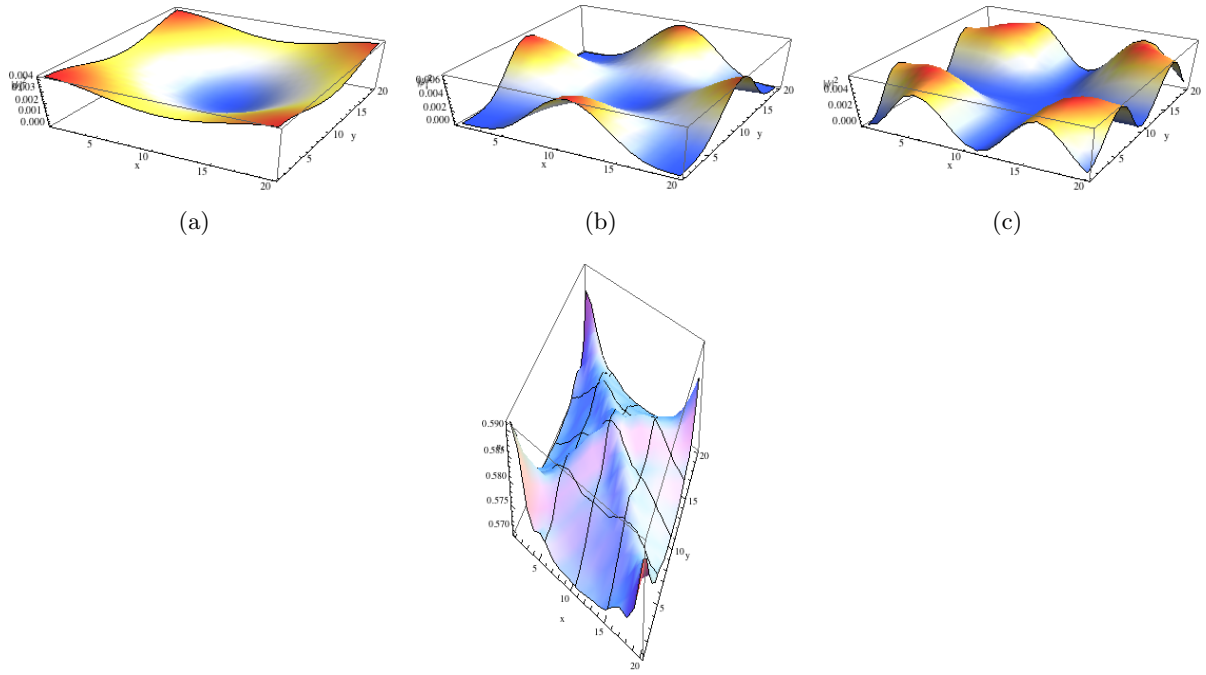

(a) (b) (c)

(d)

Figure 3.1: (a), (b), (c)Square of the modulus of the three lowest energy eigenstates of H_0. (d) Electron density n_i for $\mu = 0.3$.

As a curiosity and a check on our numerics, the spectra of H_0 plotted for different values of the magnetic flux versus the flux density $\alpha = \Phi/N_xN_y$, gives the famous $Hofstadter\ Butterfly$, as shown in Fig. 3.2.

Figure 3.2: The $Hofstadter\ Butterfly$. The entire spectra is plotted for fluxes going from $2\Phi_0$ at the very left to $2N_xN_y\Phi_0$ at the right.

3.5 Phenomenology of the superconducting state in the presence of an external magnetic field: the mixed state

An important feature of superconductors is that in the superconducting phase (below the temperature dependent critical field $B_{c1}(T)$), they are perfect diamagnets, they the expel magnetic field completely (this also called the $Meissner - Ochsenfeld\ Effect$). In *type I* superconductors, the transition between the superconducting and the normal state takes place abruptly at B_c. Instead, in *type II* superconductors, the change is not abrupt. There are two critical values of the field, such that when $B_{c1} \leq B \leq B_{c2}$, the magnetic field penetrates in certain regions called vortices, where superconductivity is strongly suppressed. This state is called *the mixed state*.

In 1950, Ginzburg and Landau created a phenomenological theory where they generalized the Landau theory of second-order phase transitions to the normal-superconducting transition. They assumed that the superconducting phase can be characterized by a order parameter that takes a finite value in the superconducting phase and goes to zero in the normal state. They also assumed that this order parameter is related to the wave function of the superconducting electrons. In this theory, there are two characteristic lengths; the *coherence length* ξ which characterizes the length of the region where the order parameter varies at a normal-superconducting interface, and the *penetration depth* λ_L which characterizes the length of the region where the magnetic field can penetrate the superconductor. In this theory, the two types of superconductors are classified by the $Ginzburg - Landau(G-L)$ parameter κ. When $\kappa < \frac{1}{\sqrt{2}}$, the surface energy of the normal-superconducting interface is positive and we have a *type I* superconductor. When $\kappa > \frac{1}{\sqrt{2}}$, the energy of the interface is negative and we have a *type II* superconductor. In $G-L$ *theory* it is also showed that the flux penetrating each vortex is equal to an integer number of half flux quanta $\Phi_0 = \frac{h}{2e}$. Actually, each vortex is penetrated by a single Φ_0 because, the fact that the energy of the interface between normal and superconducting state is negative, makes it energetically favorable to have as many vortices as possible.

3.6 Supercurrents

In our microscopic theory, the way we see whether superconductivity is suppressed is by looking at the SCOP (see Eq.(2.17)). Its modulus is shown in Fig.3.3.

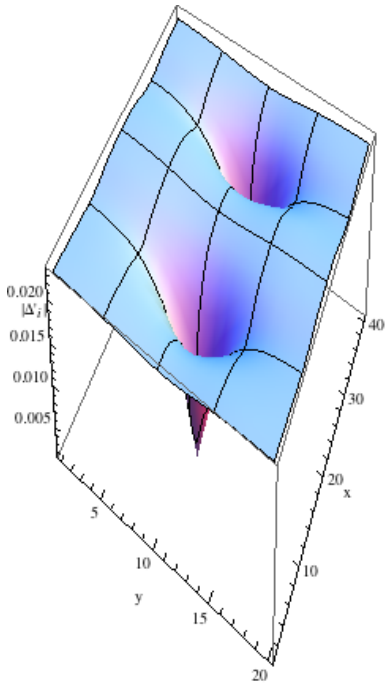

Figure 3.3: Plot of the modulus of the SCOP of LiFeAs. It is calculated within the RPA approximation (see Chapter 4) for the parameters, $U_{RPA} = 0.9$, $U = 0$. Two half flux quantum cross the system (one half is $\Phi_0 = h/2e$). Each vortex encapsulates one Φ_0.

Furthermore, in order to verify that the modulation of the SCOP shown in Fig.3.3 is due to vortices, we calculate the supercurrents induced in the system as the magnetic field penetrates it.

We start out from the continuity equation

$$\frac{\partial \hat{\rho}_i}{\partial t} + (\nabla \cdot \hat{\mathbf{j}})_i = 0, \tag{3.57}$$

where $\hat{\rho}_i = -e\hat{n}_i$ and $\hat{\mathbf{j}}$ are the electron density and current operators respectively. The time derivative of the density operator at site i is given by

$$\dot{\hat{n}}_i = \frac{i}{\hbar}[H^{MF}, \hat{n}_i], \tag{3.58}$$

where H^{MF} is given in Eq. (2.18) of Chapter 2. Since $\hat{n}_i = \sum_\mu \hat{n}_{i\mu}$, the time derivative of the density operator at site i and orbital μ is given by

$$\dot{\hat{n}}_{i\mu} = \frac{i}{\hbar}[H^{MF}, \hat{n}_{i\mu}]. \tag{3.59}$$

Thus, we need to commute each term of H^{MF}. The commutations $[H_N, \hat{n}_{i\mu}] = [H^{MF}_{int}, \hat{n}_{i\mu}] = [H_Z, \hat{n}_{i\mu}] = 0$ are trivially zero. The commutation $[H^{MF}_{BCS}, \hat{n}_{i\mu}] \neq 0$ is non zero but this is one of the anomalies of the BCS mean-field theory (there is no particle number cobservation). The

correct thing to do is to instead commute H_{BCS} (see Eq. (2.13) in Chapter 2). After doing some algebra, we find $[H_{BCS}, \hat{n}_{i\mu}] = 0$. Hence, we are left with H_0. Thus,

$$\dot{\hat{n}}_{i\mu} = \frac{i}{\hbar}[H_0, \hat{n}_{i\mu}]. \tag{3.60}$$

$$\begin{aligned}
[H_0, \hat{n}_{k\alpha}] &= \sum_{ij,\mu\nu,\sigma\sigma'} t_{ij}^{\mu\nu} e^{i\varphi_{ij}} [\hat{c}_{i\mu\sigma}^\dagger \hat{c}_{j\nu\sigma}, \hat{c}_{k\alpha\sigma'}^\dagger \hat{c}_{k\alpha\sigma'}] \qquad (3.61)\\
&= \sum_{ij,\mu\nu,\sigma\sigma'} t_{ij}^{\mu\nu} e^{i\varphi_{ij}} (\hat{c}_{k\alpha\sigma'}^\dagger [\hat{c}_{i\mu\sigma}^\dagger \hat{c}_{j\nu\sigma}, \hat{c}_{k\alpha\sigma'}] + [\hat{c}_{i\mu\sigma}^\dagger \hat{c}_{j\nu\sigma}, \hat{c}_{k\alpha\sigma'}^\dagger] \hat{c}_{k\alpha\sigma'})\\
&= \sum_{ij,\mu\nu,\sigma\sigma'} t_{ij}^{\mu\nu} e^{i\varphi_{ij}} (-\hat{c}_{k\alpha\sigma'}^\dagger \hat{c}_{j\nu\sigma}^\dagger \delta_{ik}\delta_{\mu\alpha}\delta_{\sigma\sigma'} + \hat{c}_{i\mu\sigma}^\dagger \hat{c}_{k\alpha\sigma'}^\dagger \delta_{jk}\delta_{\nu\alpha}\delta_{\sigma\sigma})\\
&= \sum_{j\nu\sigma} (-t_{kj}^{\alpha\nu} e^{i\varphi_{kj}} \hat{c}_{k\alpha\sigma}^\dagger \hat{c}_{j\nu\sigma} + t_{jk}^{\nu\alpha} e^{i\varphi_{jk}} \hat{c}_{j\nu\sigma}^\dagger \hat{c}_{k\mu\sigma}).
\end{aligned}$$

Thus,

$$-e\dot{\hat{n}}_{i\mu} + \frac{ie}{\hbar} \sum_{j,\nu,\sigma} (-t_{ij}^{\mu\nu} e^{i\varphi_{ij}} \hat{c}_{i\mu\sigma}^\dagger \hat{c}_{j\nu\sigma} + t_{ji}^{\nu\mu} e^{i\varphi_{ji}} \hat{c}_{j\nu\sigma}^\dagger \hat{c}_{i\mu\sigma}) = 0, \tag{3.62}$$

$$(\nabla \cdot \hat{\mathbf{j}})_{i\mu} = -\frac{ie}{\hbar} \sum_{j,\nu,\sigma} (-t_{ij}^{\mu\nu} e^{i\varphi_{ij}} \hat{c}_{i\mu\sigma}^\dagger \hat{c}_{j\nu\sigma} + t_{ji}^{\nu\mu} e^{i\varphi_{ji}} \hat{c}_{j\nu\sigma}^\dagger \hat{c}_{i\mu\sigma}). \tag{3.63}$$

We define the current going from site j and orbital ν to site i and orbital μ as

$$j_{j\nu\to i\mu} = -\frac{ie}{\hbar} \sum_\sigma t_{ij}^{\mu\nu} e^{i\varphi_{ij}} \hat{c}_{i\mu\sigma}^\dagger \hat{c}_{j\nu\sigma}, \tag{3.64}$$

so that we can define the divergence of the current at site i and orbital μ as (it is just a rewriting of Eq. (3.63))

$$(\nabla \cdot \hat{\mathbf{j}})_{i\mu} = \sum_{j,\nu} j_{i\mu\to j\nu} - j_{j\nu\to i\mu}, \tag{3.65}$$

which is very intuitive. This equation tells us that the divergence of the current at site i and orbital μ is equal to the current going out minus the current going in. Also, that the total current going out from site i and orbital μ is equal to the divergence $(\nabla \cdot \hat{\mathbf{j}})_{i\mu}$. The index ν runs for the five orbitals of our model and j goes up to fifth nearest neighbors.

In the next step, we take the thermal average of Eq. (3.64) and perform the Bogoliubov transformation given in Eq. (A.20) of Chapter 2. Thus we arrive to

$$\langle j_{j\nu\to i\mu} \rangle = -\frac{ie}{\hbar} \sum_n t_{ij}^{\mu\nu} e^{i\varphi_{ij}} (u_{i\mu}^{n*} u_{j\nu}^n f(E_n) + v_{i\mu}^n v_{j\nu}^{n*} f(-E_n)) \tag{3.66}$$

$$\langle (\nabla \cdot \hat{\mathbf{j}})_{i\mu} \rangle = -\frac{ie}{\hbar} \sum_{j,\nu,n} [t_{ji}^{\nu\mu} e^{i\varphi_{ji}} (u_{j\nu}^{n*} u_{i\mu}^n f(E_n) + v_{j\nu}^n v_{i\mu}^{n*} f(-E_n)) - \tag{3.67}$$

$$t_{ij}^{\mu\nu} e^{i\varphi_{ij}} (u_{i\mu}^{n*} u_{j\nu}^n f(E_n) + v_{i\mu}^n v_{j\nu}^{n*} f(-E_n))] \tag{3.68}$$

where n runs over all the eigenenergies.

By calculating $\langle(\nabla \cdot \hat{\mathbf{j}})_{i\mu}\rangle$ at each site, it is possible to see the orbital resolved supercurrents shown in Fig. 3.4.

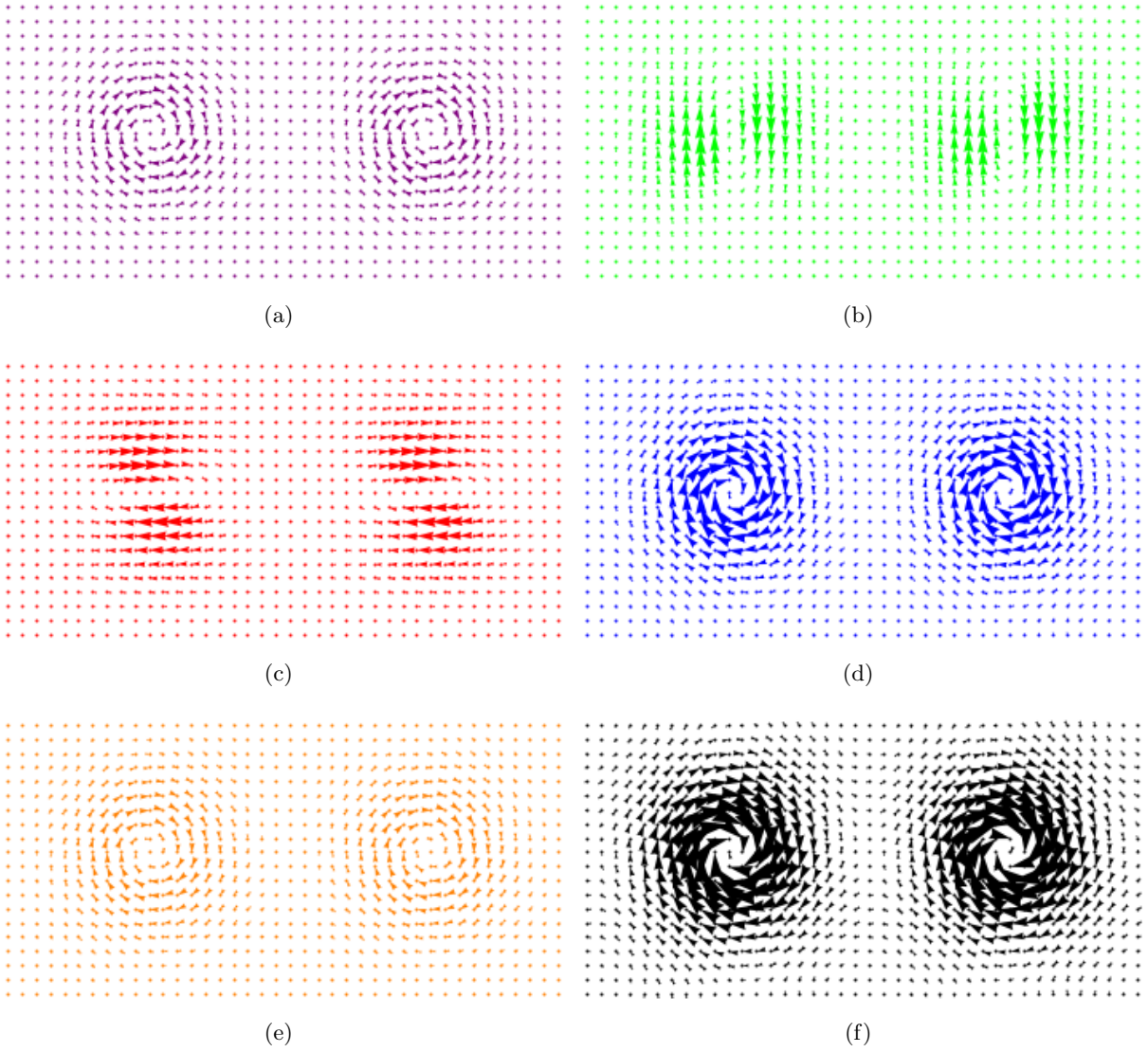

Figure 3.4: Orbital resolved supercurrents: (a) $d_{3z^2-r^2}$, (b) d_{yz}, (c) d_{xz}, (d) d_{xy}, (e) $d_{x^2-y^2}$ and (e) the total supercurrent (the sum of all the orbitals).

It is interesting to see how the supercurrents shown in Fig.3.4, have the symmetry of the orbitals (as they should), and also the intensity (expressed with the size of the head of the arrows) in agreement with the weight of each orbital at the Fermi surface, where among the five orbitals present, d_{yz}, d_{xz} and d_{xy} are the ones with the largest weight. Actually the supecurrents belonging to the orbitals $d_{3z^2-r^2}$ and $d_{x^2-y^2}$ have had to be enlarged by hand to make them visible in Fig. 3.4.

Chapter 4

Effective pairing

Regarding the superconductivity in our model expressed by the BCS term in our Hamiltonian, we take two very different approaches throughout our work. We sometimes treat it phenomenologically and put superconductivity by hand without taking into account each microscopic origin but some other times we take a more sophisticated approach explained in this chapter. We will assume that the origin of superconductivity in FeSC is the spin fluctuation mechanism and we will calculate the effective pairing within this approach. The calculation of the pairing was done using a code developed by Maria Navarro Gastiasoro, a member of our group.

4.1 The spin fluctuation glue

The electron-phonon interaction is not enough as to explain the high T_c in this materials [51]. The theory for the pairing is constructed based on the idea that the BCS theory is essentially valid to explain high T_c superconductivity but a different ingredient is necessary to substitute the role of the phonons, which cannot explain high temperature superconductivity. Then, one can think that the "glue" emerges from the interacting electron system itself. Magnetism is usually nearby in these materials and the most popular candidate is the spin fluctuation theory. It is similar to the conventional superconductivity mechanism in that the exchange of paramagnons, instead of phonons, results in an effective attractive interaction of electrons.

The effective electron-electron interaction is calculated by use of perturbation theory, summing a series of diagrams to infinite order. An example of such diagrammatic series is shown in Fig. 4.1. The first term in the series expresses the simple Coulomb interaction between two Fermion lines (black lines) with opposite spin, and it is a first order term since it has one interaction line (red dashed line). The next term is a third order term and it stands for the simplest diagram of exchange of longitudinal spin fluctuations. It involves two particle-hole bubbles χ_0 (bare spin susceptibility involving two single-particle propagators) connected by interacting U lines. The Hamiltonian to which these interactions correspond in the one band case is shown in Eq.(4.1). Because we restrict the Coulomb interaction to onsite interactions, U must connect Fermion lines of opposite spins, thus, we can only have an even number of bubbles. Hence, the higher order terms expressed by "..." have an even number of bubbles. The second line series express the exchange of transverse spin fluctuations. The sum of all these diagrams to infinite order gives rise to the effective spin-fluctuation mediated electron-electron interaction V_s.

$$H_{int} = U \sum_{kk'q} \hat{c}^{\dagger}_{k\uparrow} \hat{c}^{\dagger}_{k'+q\downarrow} \hat{c}_{k-q\uparrow} \hat{c}_{k'\downarrow} \tag{4.1}$$

This theoretical approach has been studied in depth for single band systems by [15], among others.

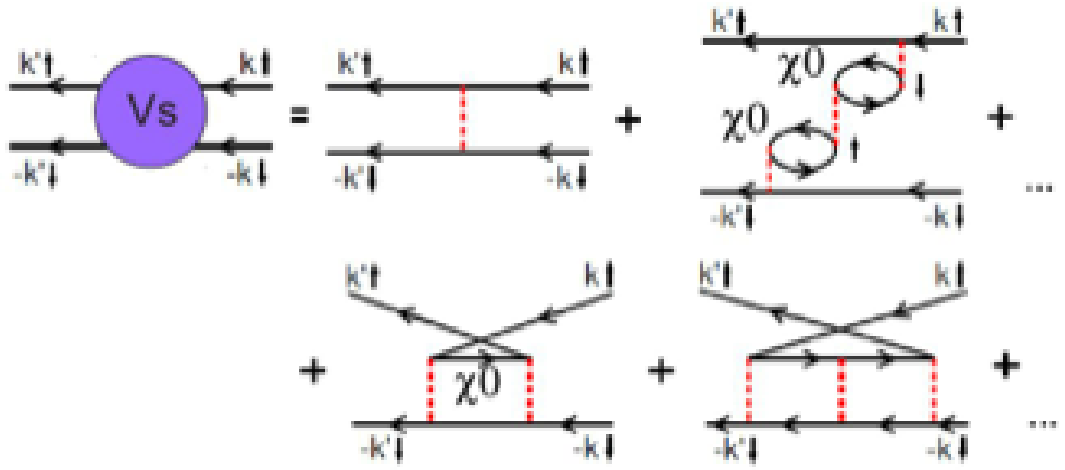

Figure 4.1: Effective pairing interaction between opposite spins. Solid lines are single-particle propagators, and red dashed lines the interaction U between opposite spins in the single-band system. Figure taken from [20].

4.2 The spin and charge susceptibilities

In this chapter we explain how the charge and spin susceptibilities are calculated in the paramagnetic regime. We will work in momentum space. The kinetic energy term is given by

$$H_0 = \sum_{k\sigma}\sum_{\mu\nu}\xi_{\mu\nu}\hat{c}^{\dagger}_{\mu\sigma}(k)\hat{c}_{\nu\sigma}(k) - \mu_0\sum_{k\mu\sigma}\hat{c}^{\dagger}_{\mu\sigma}(k)\hat{c}_{\mu\sigma}(k) \tag{4.2}$$

The first step consists on calculating the two-particle correlation function of the non-interacting Hamiltonian. The general expression for a multi orbital system is

$$\chi_{0st}^{pq}(q,\tau) = \frac{1}{N}\sum_{kk',\sigma\sigma'}\left\langle T_\tau \hat{c}^{\dagger}_{p\sigma}(k,\tau)\hat{c}_{q\sigma}(k+q,\tau)\hat{c}^{\dagger}_{t\sigma'}(k',0)\hat{c}_{s\sigma'}(k'-q,0)\right\rangle_0 \tag{4.3}$$

where p, q, s, t are orbital indices. By Wick's theorem this is given by a product of single-particle Matsubara Green's functions with all possible pairings and with the sign given by the number of times we interchange two fermion operators

$$\chi_{0st}^{pq}(q,\tau) = \frac{1}{N}\sum_{kk',\sigma\sigma'}(\underbrace{\mathcal{G}_{q\sigma,p\sigma}(k+q,k;\tau,\tau)\mathcal{G}_{s\sigma',t\sigma'}(k'-q,k';0,0)}_{=0} - \mathcal{G}_{s\sigma',p\sigma}(k'-q,k;0,\tau)\mathcal{G}_{q\sigma,t\sigma'}(k+q,k';\tau,0)) \tag{4.4}$$

$$= -\frac{1}{N}\sum_{kk',\sigma\sigma'}\mathcal{G}_{s\sigma',p\sigma}(k'-q,k;0,\tau)\mathcal{G}_{q\sigma,t\sigma'}(k+q,k';\tau,0)$$

$$= -\frac{1}{N}\sum_{k,\sigma}\mathcal{G}_{sp\sigma}(k,-\tau)\mathcal{G}_{qt\sigma}(k+q,\tau)$$

where

$$\mathcal{G}_{\mu\nu}(k,k';\tau,\tau') = \left\langle T_\tau \hat{c}_\mu(k,\tau)\hat{c}^{\dagger}_{\nu}(k',\tau')\right\rangle_0 \tag{4.5}$$

In the last equality of Eq.(4.4) we made use of the knowledge about the explicit time dependence of $\mathcal{G}$ and the form of H_0.

Then, we calculate the Fourier transform

$$\begin{aligned}\chi_{0st}^{pq}(q,ik_n) &= \int_0^\beta d\tau e^{ik_n\tau}\chi_{0st}^{pq}(q,\tau) \\ &= -\frac{1}{\beta N}\sum_{k\sigma}\sum_{iw_n,iq_n}\mathcal{G}_{sp\sigma}(k,iw_n)\mathcal{G}_{qt\sigma}(k+q,iq_n)(\frac{1}{\beta}\int_0^\beta d\tau e^{i(k_n+w_n-q_n)\tau}) \\ &= -\frac{1}{\beta N}\sum_{k\sigma}\sum_{iw_n}\mathcal{G}_{sp\sigma}(k,iw_n)\mathcal{G}_{qt\sigma}(k+q,iw_n+ik_n)\end{aligned} \tag{4.6}$$

In order to get an analytical expression of the susceptibility, we diagonalize the Hamiltonian to get an expression for the Matsubara Green's functions in the spectral representation. We perform the unitary transformation $\hat{c}_{\mu\sigma}(k) = \sum_n u_\mu^n(k)\hat{\gamma}_{n\sigma}(k)$.

$$\begin{aligned}H_0 &= \sum_{k,\sigma}\sum_{\mu\nu}(\xi_{\mu\nu}(k)-\mu_0\delta_{\mu\nu})\hat{c}_{\mu\sigma}^\dagger(k)\hat{c}_{\nu\sigma}(k) \\ &= \sum_{k,\sigma}\sum_{nm}\sum_{\mu\nu}u_\mu^{n*}(k)(\xi_{\mu\nu}(k)-\mu_0\delta_{\mu\nu})u_\nu^m(k)\hat{\gamma}_{n\sigma}^\dagger(k)\hat{\gamma}_{m\sigma}(k) \\ &= \sum_{k,\sigma}\sum_{nm}(U^\dagger(k)(\xi(k)-\mu_0\delta)U(k))_{nm}\hat{\gamma}_{n\sigma}^\dagger(k)\hat{\gamma}_{m\sigma}(k) \\ &= \sum_{k,\sigma}\sum_{n}(E_n(k)-\mu_0)\hat{\gamma}_{n\sigma}^\dagger(k)\hat{\gamma}_{n\sigma}(k)\end{aligned} \tag{4.7}$$

where $U(k)$ is a matrix with the eigenvectors of $\xi(k)$ put in rows and $E_n(k)$ are the eigenvalues of $\xi(k)$. n is the band index. Now, performing the same transformation in the Matsubara Green's functions

$$\begin{aligned}\mathcal{G}_{\mu\nu\sigma}(k,-\tau) &= -\left\langle T_\tau\hat{c}_{\mu\sigma}(k,0)\hat{c}_{\nu\sigma}^\dagger(k,\tau)\right\rangle_0 \\ &= -\left\langle T_\tau\hat{c}_{\mu\sigma}(k)e^{\tau H_0}\hat{c}_{\nu\sigma}^\dagger(k)e^{-\tau H_0}\right\rangle_0 \\ &= -\sum_n u_\mu^n(k)u_\nu^{n*}(k)\left\langle T_\tau\hat{\gamma}_{n\sigma}(k,0)\hat{\gamma}_{n\sigma}^\dagger(k,\tau)\right\rangle_0 \\ &\equiv \sum_n u_\mu^n(k)u_\nu^{n*}(k)G_{n\sigma}(k,-\tau),\end{aligned} \tag{4.8}$$

which implies

$$\mathcal{G}_{\mu\nu\sigma}(k,iw_n) = \sum_n u_\mu^n(k)u_\nu^{n*}(k)G_{n\sigma}(k,iw_n) \tag{4.9}$$

and because H_0 is diagonal in the $\hat{\gamma}_{n\sigma}(k)$ operator,

$$G_{n\sigma}(k,iw_n) = \frac{1}{iw_n - E_n(k)}. \tag{4.10}$$

Thus,

$$\chi_{0st}^{pq}(q,ik_n) = \frac{-1}{N}\sum_{k\sigma}\sum_{nm} u_s^n(k)u_p^{n*}(k)u_q^m(k+q)u_t^{m*}(k+q)\left[\frac{1}{\beta}\sum_{iw_n}\frac{1}{iw_n - E_n(k)}\cdot\frac{1}{iw_n-(E_n(k+q)-ik_n)}\right], \tag{4.11}$$

and by performing the Matsubara sum, evaluating the bosonic frequency and doing the analytical continuation ($ik_n \to w + i\eta$), we finally get

$$\chi_{0st}^{pq}(q,ik_n) = \frac{-1}{N}\sum_{k\sigma}\sum_{nm} u_s^n(k)u_p^{n*}(k)u_q^m(k+q)u_t^{m*}(k+q)\left[\frac{f(E_n(k))-f(E_n(k+q))}{w+E_n(k)-E_n(k+q)+i\eta}\right]. \tag{4.12}$$

This is the well known Lindhard function of the non-interacting multi-band electron gas.

When the interactions are taken into account, the susceptibility changes. The interactions are included within the RPA approximation, in which the infinite sum of the most divergent diagrams for each order is performed (the ones with maximum number of pair-bubbles, which dominate the physics in the high-density limit). For a multi-band system, the RPA charge and spin susceptibilities are obtained in the form of Dyson-type equations as [60]

$$\chi_c^{RPA}(q,w) = \chi_0(q,w)[1+U^c\chi_0(q,w)]^{-1}, \tag{4.13}$$
$$\chi_s^{RPA}(q,w) = \chi_0(q,w)[1-U^s\chi_0(q,w)]^{-1}, \tag{4.14}$$

where for the five orbital model χ_0, U^c and U^s are 25x25 matrices. The matrices U^c and U^s are given as

$$(U^c)_{aa}^{aa} = U, \quad (U^c)_{aa}^{bb} = 2U-5J, \quad (U^c)_{ab}^{ab} = \frac{13}{4}J - U, \quad (U^c)_{ab}^{ba} = J, \tag{4.15}$$

and

$$(U^s)_{aa}^{aa} = U, \quad (U^s)_{aa}^{bb} = J, \quad (U^s)_{ab}^{ab} = -\frac{9}{4}J + U, \quad (U^s)_{ab}^{ba} = J. \tag{4.16}$$

4.3 Effective pairing

Assuming that the pairing interaction giving rise to superconductivity in the FeSC comes from the exchange of spin and charge fluctuations, the pairing is calculated using the fluctuation exchange approximation [60]

$$\Gamma_{pqst}(k-k',0) = \left[\frac{3}{2}U^s\chi_s^{RPA}(k-k',0)U^s + \frac{1}{2}U^s - \frac{1}{2}U^c\chi_c^{RPA}(k-k',0)U^c + \frac{1}{2}U^c\right]_{pq}^{st}. \tag{4.17}$$

In Fig. 4.2 first order scattering vertices for the multi orbital Hubbard model are shown. The effective interaction Hamiltonian H_{sc} of this singlet pairing vertex is given by

$$H_{sc} = \sum_{pqst}\sum_{kk'}\Gamma_{pqst}(k-k',0)c_{p\uparrow}^\dagger(k')c_{t\downarrow}^\dagger(-k')c_{s\downarrow}(-k)c_{q\uparrow}(k) \tag{4.18}$$

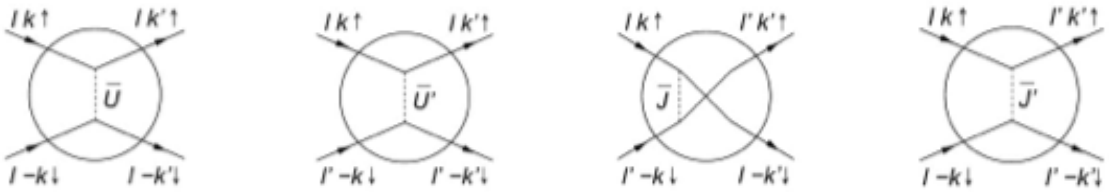

(a) (b) (c) (d)

Figure 4.2: First order scattering vertices corresponding to (a) intra-, (b)-(c) mixed- and (d) inter-orbital pair scattering processes. l and l' are orbital indexes and the interaction parameters $\bar{U} \equiv U$, $\bar{U}' \equiv U' - J$, $\bar{J} \equiv J$ and $\bar{J}' \equiv J'$. The Coulomb matrix elements were derived in equation (see Eq.(2.6) in Chapter 2).Graphic taken from [21].

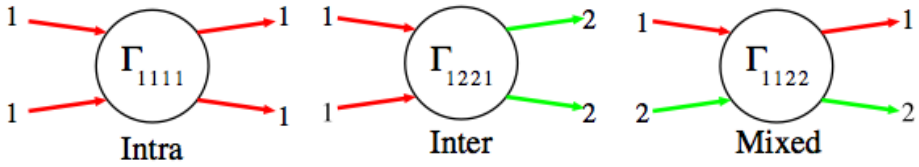

Figure 4.3: Some examples of orbital vertices for intra, inter and mixed orbital vertices. Figure taken from [35].

Fig. 4.3 shows some examples of scattering processes in multi orbital systems.

The last step consists on writing H_{sc} in a real space representation. Thus, by using the transformation $c_{\mu\sigma}(k) = \frac{1}{\sqrt{N}} \sum_r c_{\mu\sigma}(r) e^{ikr}$

$$
\begin{aligned}
H_{sc} &= \sum_{pqst} \sum_{kk'} \Gamma_{pqst}(k-k',0) \frac{1}{N^2} \sum_{r_p r_t r_s r_q} e^{i(r_p - r_t)k'} e^{i(r_q - r_s)k} c^\dagger_{p\uparrow}(r_p) c^\dagger_{t\downarrow}(r_t) c_{s\downarrow}(r_s) c_{q\uparrow}(r_q) \qquad (4.19) \\
&= \sum_{pqst} \sum_{r_i r_j} c^\dagger_{p\uparrow}(r_p) c^\dagger_{t\downarrow}(r_t) c_{s\downarrow}(r_s) c_{q\uparrow}(r_q) \sum_{kk'} e^{i(r_i - r_j)(k-k')} \Gamma_{pqst}(k-k',0) \\
&= \sum_{pqst} \sum_{ij} \Gamma_{pqst}(r,0) c^\dagger_{ip\uparrow} c^\dagger_{jt\downarrow} c_{js\downarrow} c_{iq\uparrow},
\end{aligned}
$$

where

$$
\Gamma_{pqst}(r,0) = \sum_q \Gamma_{pqst}(q,0) e^{iqr}, \quad q \equiv k - k', \quad r = r_i - r_j. \qquad (4.20)
$$

In the second equality, we defined $r_i \equiv r_p = r_q$ and $r_j \equiv r_s = r_t$, it comes from the fact that H_{sc} (see Eq.(4.18)) depends only k and k'.

Now, we only have calculate $\Gamma_{pqst}(r,0)$ for onsite($r = 0$), nearest neighbours($r = (0, \pm 1)$ and $r = (\pm 1, 0)$) and next nearest neighbors ($r = (\pm 1, \pm 1)$).

Chapter 5

Vortex-enhanced magnetization

In this chapter we will study the role of the magnetic field in the coexisting phase of the magnetic and superconducting state in 1111 superconductors. In doing so, we will try to qualitatively reproduce some recent experimental results from [63]. We will answer the following questions:

- How does the magnetic field enhance the Bragg peak? Do the magnetic moments become larger or does the magnetic structure change?

5.1 Band structure

LaFeAsO has a tetragonal layered structure, in which Fe atoms are arrayed on a square lattice (see Fig. 1.2(a). Because of the tetrahedral coordination of As, there are two Fe atoms per unit cell. Each Fe layer is then sandwiched between LaO layers (see Fig. 1.2(a) in Chapter 1). The band structure used for this calculation is the corresponding to LaFeAsO with the 1111 structure, taken from [37], where they first calculated the band structure and then constructed the maximally localized Wannier functions (MLWFs) spanning the Hilbert space of the $3d$ bands (see Fig. 5.1(a)). These MLWFs, centered at the two Fe sites in the unit cell, have five orbital symmetries ($d_{3Z^2-R^2}, d_{XZ}, d_{YZ}, d_{X^2-Y^2}$ and d_{XY}, where X, Y and Z refer to those for the original unit cell). It can be noted that the two Wannier orbitals in each unit cell are equivalent in that each Fe atom has the same local arrangement of other atoms. Thus, it is possible to take a unit cell that contains only one orbital per symmetry by unfolding the BZ, resulting in an effective five-band model on a square lattice, where x and y axes are rotated by 45° from $X - Y$. The FS is composed of two hole pockets (α_1, α_2) around the Γ point, two electron pockets (β_1, β_2) around the X and Y points of the unfolded BZ and a hole pocket (γ) around the M point of the unfolded BZ (see Fig. 5.1(b)).

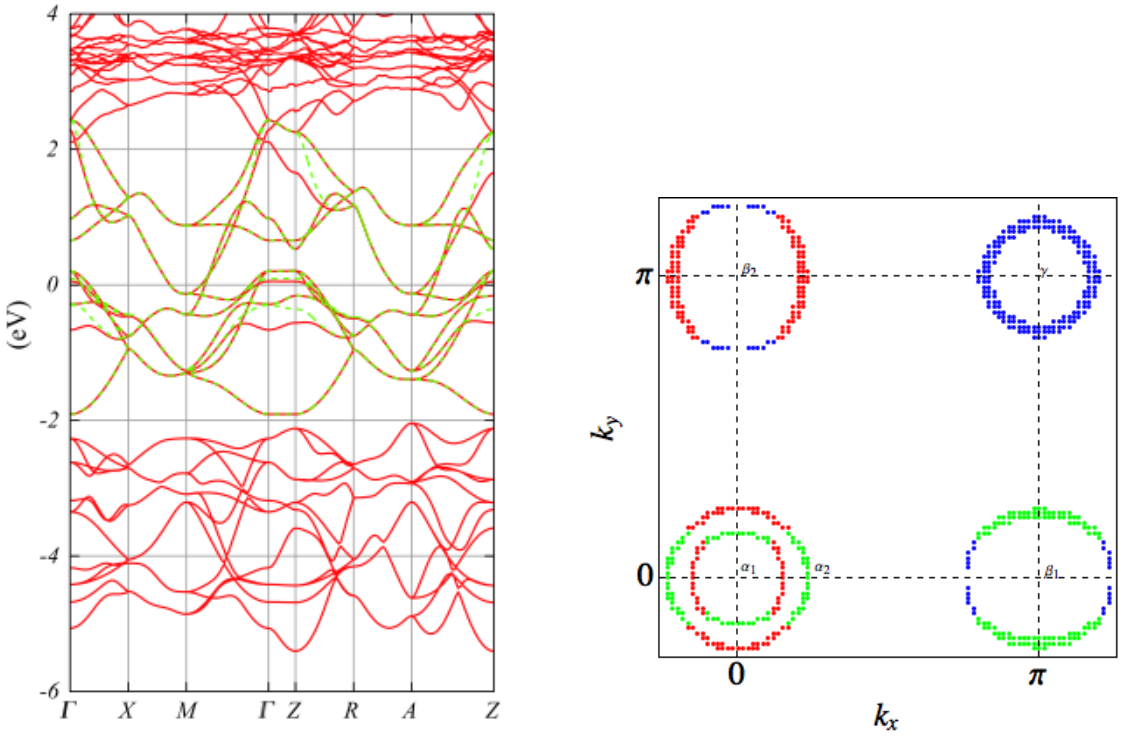

(a) (b)

Figure 5.1: (a) Red lines denote the electronic band structure of undoped LaFeAsO. Green dashed lines are the ten-band model obtained with the MLWFs method. (b) FS in the unfolded BZ (five-band model) for 1111 structure with electron filling n=6.0 and with colors indicating the main orbital character (red=d_{xz}, green=d_{yz}, blue=d_{xy}).

5.2 Magnetic order

The parent compounds of the 1111 materials are metals which exhibit spin density wave (SDW) order. This was first realized in LaFeAsO and the low temperature ordered magnetic moment was 0.36 μ_B which is much smaller than the one observed in metallic Fe 2.2 μ_B. In real-space the spins align antiferromagnetically along the elongated a axis and ferromagnetically along the b axis (see Fig. 5.2).

In order to study the magnetization of the system described by our model, we first look at the $H_0 + H_N + H_{int}^{MF}$ part of our model mean-field Hamiltonian (see Eq. 2.18 in Chapter 2)

$$H = H_0 + H_N + H_{int}^{MF} = \sum_{ij,\mu\nu,\sigma} t_{ij}^{\mu\nu} e^{i\varphi_{ij}} \hat{c}_{i\mu\sigma}^{\dagger} \hat{c}_{j\nu\sigma} - \mu_0 \sum_{i\mu\sigma} \hat{n}_{i\mu\sigma} + \sum_{i,\mu\neq\nu,\sigma} [U\langle\hat{n}_{i\mu\bar{\sigma}}\rangle + U'\langle\hat{n}_{i\nu\bar{\sigma}}\rangle + (U'-J)\langle\hat{n}_{i\nu\sigma}\rangle]\hat{n}_{i\mu\sigma} \tag{5.1}$$

and allow the parameters U, U', J and J' to be non zero. We calculate the magnetization $m_i = \sum_\mu (n_{i\mu\uparrow} - n_{i\mu\downarrow})$ self-consistently. In all our calculations, we assume spin and orbital rotational invariance so that $U' = U - 2J$ and $J' = J$ hold [25]. Thus, we only need to assign values to U and J.

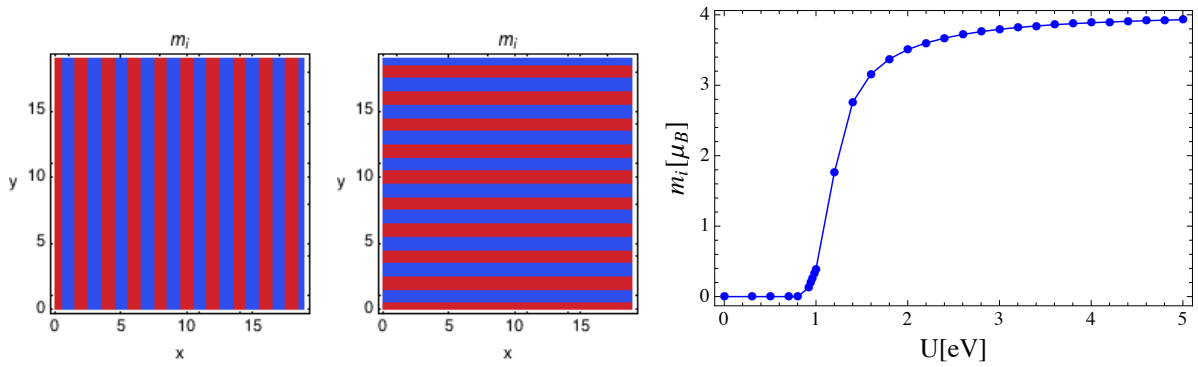

(a) (b) (c)

Figure 5.2: Magnetic structure (red $m_i = 0.3\mu_B$ and blue $m_i = -0.3\mu_B$) for $U = 0.97$ and $J = U/4$ in the (a) $\mathbf{Q} = (\pi, 0)$, (b) $\mathbf{Q} = (0, \pi)$ SDW states. (c) Magnetic moment at one site versus U for $J = U/4$.

We see that the resulting state is a SDW state, above a certain value of U (see Fig. 5.2). The direction of the stripes depends on the initial guess, because the model lattice is square and thus, both states are energetically degenerate.

What is the origin of the magnetism in this model? The FS is characterized by nesting with $\mathbf{Q} = (\pi, 0)$, which corresponds to stripe-type antiferromagnetic (AF) ordering. This nesting leads to the $(\pi, 0)$ AF spin fluctuation as the dominant fluctuation within RPA [44]. This fluctuation comes mainly from scattering between the β and γ pockets, which are shown in Fig. 5.1(b).

When studying such a complicated system as we are doing here, it is not possible to do analytics and the only option is to do numerics, which makes it not straight-forward to understand the origin of the calculated results. Even so, it is very useful to do analytics on simpler systems because these are in some cases related to the complicated ones or they might give a picture of what actually happens. Thus, to get an idea of how this works, it is helpful to think of the spin susceptibility of the simpler one-band model, which, within the RPA approximation, is given by

$$\chi^{RPA}(\mathbf{k}, w) = \frac{\chi_0(\mathbf{k}, w)}{1 - U\chi_0(\mathbf{k}, w)}. \tag{5.2}$$

The spin susceptibility diverges when the dynamical Stoner criterion

$$1 - U\mathrm{Re}\chi_0(\mathbf{k}, w) = 0 \quad \text{and} \quad \mathrm{Im}\chi_0(\mathbf{k}, w) \text{ small}, \tag{5.3}$$

is fulfilled. The divergence leads to an instability in the spin channel and the system undergoes a magnetic transition. The instability will in general appear for the wave vector $\mathbf{k}$ at which $\chi^{RPA}(\mathbf{k}, w)$ is peaked. A special shape of the FS or the nesting can also lead to the instability. Nested Fermi surfaces are such that different parts of them will coincide when shifted by a certain wave vector. In order to have nesting, we only need to have that the energy spectrum satisfies

$$\epsilon(\mathbf{k} + \mathbf{Q}) = -\epsilon(\mathbf{k}), \tag{5.4}$$

where energies are counted from the chemical potential. We say that we have perfect nesting when all the $\mathbf{k}$ points fullfil Eq. (5.4) and we say we have partial nesting when only some of them do. If the nesting is perfect, the non-interacting response function χ_0 itself diverges and the magnetic transition takes place for an arbitrarily small repulsion U. If the nesting is partial,

χ_0 will be peaked at some nesting vector $\mathbf{Q}$, but the Stoner criterion will then be satisfied for a certain critical U_c at this nesting wave vector, and the system will develop a SDW with ordering vector $\mathbf{Q}$.

Now, why is the nesting related to the magnetic instability? In order to get some intuition, we are going to look at the one dimensional electron gas.

An one-dimensional metal always has a nested Fermi surface, it consists of two points, one at $+k_F$ and one at $-k_F$, two sheets separated by $2k_F$. The dispersion relation for a 1d free electron gas is given by $\epsilon(k) = \hbar^2 k^2/2m$, and the Fermi energy by

$$\epsilon_F = \frac{\hbar^2}{2m}\left(\frac{N_0\pi}{2L}\right) = \frac{\hbar^2 k_F^2}{2m_e} \tag{5.5}$$

where N_0 is the total number of electrons, L is the length of the 1d chain, and m_e is the free electron mass. The Fermi wave vector is

$$k_F = \frac{N_0\pi}{2L} = N_e\pi \tag{5.6}$$

where N_e is the number of electrons per unit length and per spin direction. The density of states for one spin direction is

$$n(\epsilon) = \frac{L}{\pi\hbar}\left(\frac{m_e}{2\epsilon}\right)^{1/2} = \frac{L}{\pi\hbar v} \tag{5.7}$$

where the velocity v is given by $m_e v = \hbar k$.

The response of an electron gas to a time independent potential

$$\phi(r) = \int \phi(q) e^{iqr} dq \tag{5.8}$$

is usually treated within the framework of linear response theory. The rearrangement of the charge density, expressed in terms of an induced charge

$$\rho^{ind}(r) = \int \rho^{ind}(q) e^{iqr} dq \tag{5.9}$$

is related to $\phi(r)$ through

$$\rho^{ind}(q) = \chi_0(q)\phi(q) \tag{5.10}$$

where $\chi_0(q)$, is the Lindhard response function and for an infinite system it is given by

$$\chi_0(q) = \int \frac{dk}{2\pi} \frac{f(\epsilon_k) - f(\epsilon_{k+q})}{\epsilon_k - \epsilon_{k+q}} \tag{5.11}$$

where f is the Fermi function. For wave vectors near $2k_F$, $\chi_0(q)$ can be evaluated by assuming a linear dispersion relation around the ϵ_F

$$\epsilon_k - \epsilon_F = \hbar v_F (k - k_F) \tag{5.12}$$

The integral in Eq.(5.11) can readily be evaluated near $2k_F$ leading to

$$\chi_0(q) = -e^2 n(\epsilon_F) ln \left|\frac{q + 2k_F}{q - 2k_F}\right| \tag{5.13}$$

The fact that $\chi_0(q)$ diverges for $q = 2k_F$ implies that an external perturbation leads to a divergent charge redistribution; this suggests, through self-consistency, that at T=0 the electron

gas itself is unstable with respect to the formation of a charge density wave (CDW) or SDW [26]. The divergence of $\chi_0(q)$ at $q = 2k_F$ is due to the topology of the FS, which is perfectly nested. Looking at Eq.(5.11), the largest contribution comes from pairs of states, one full and the other empty, separated by $2k_F$ and with the same energy.

As in the 1d case, one may have similar situations also in 2d and 3d systems with special features of the electron energy spectrum . If the energy spectrum satisfies Eq. (5.4), the response functions will behave essentially similar to the 1d case. Therefore, such systems will be unstable with respect to a CDW formation and lattice distortion with wave vector **Q** (if the dominant interaction is the electron-phonon interaction; if instead, the dominant electron-electron interaction is repulsive, there will be a similar instability in the spin channel, and a SDW will be formed instead) [43].

5.3 Competing magnetic and superconducting order

Iron arsenide superconductors show rich phases where antiferromagnetic, tetragonal, orthorhombic and superconducting (SC) phases are found in close proximity (see Fig. 1.4 in Chapter 1). For some compounds, the transition from AFM to SC is of first order with regions of inhomogeneous coexistence. However, in $Ba(Fe_{1-x}Co_x)_2As_2$, experiments found a homogeneous coexistence of SC and AFM for intermediate doping (x) values [52] (see Fig. 1.4(c) in Chapter 1). As the system enters the SC state, the ordered magnetic moments decreases as temperature goes down and the strength of SC increases [56]. This strongly suggests that SC and magnetic order compete for the same electrons. Furthermore, there is some unpublished data [63], where this coexistence is studied for different values of external magnetic field using inelastic neutron scattering (see Fig. 5.4(b)). It is found that, while the position and width of the Bragg peak do not change, the intensity of the peak increases for higher external fields. Secondly, they also see how T_c decreases with an applied field and that the drop in intensity below T_c as T goes down, becomes smaller for increasing field strength.

5.4 Results

In this section we use the full mean-field Hamiltonian shown in Eq. 2.18 in Chapter 2

$$H^{MF} = H_0 + H_N + H_{int}^{MF} + H_{BCS}^{MF} + H_Z. \tag{5.14}$$

We first fix the interacting parameters U and J such that, we have reasonable magnetic moments within the range that the experimentalist measure for 1111 FeSC ($0.25 < \mathrm{m} < 0.8$ μ_B). For $U = 0.97$ and $J = U/4$, we have that the magnetic moments are $|m_i| = 0.37\mu_B$ at T=0.01eV/k_B, which we fix as our "zero temperature" reference. Then we include superconductivity and we fit the strength of the pairing so that, the superconductivity suppresses the moments to approximately half of the value of the non superconductivity case.

We first include the pairing within the RPA approximation explained in Chapter 4, for $B = 0T$. We find that in order to have the competition between the superconductivity and magnetism as it is found in [63], T_c needs to be larger than T_N, opposite to the experiments. On the other hand, if we tune the pairing such that T_c is below T_N, then superconductivity does not affect the magnetism.

Next, based on the idea that the RPA approximation is not justified in the magnetic state since the pairing is calculated in a non magnetic state, we forget about the microscopic origin of the superconducting pairing, and assume a non-zero attractive pairing that we introduce "by hand". In order to get the $s_\pm$ state, which has the $\cos(k_x)\cos(k_y)$ structure in momentum space,

we include only next nearest neighbor coupling pairings. We only include the intra-orbital terms because there are studies which find that the inter orbital gap amplitudes are negligible [59], and that the intra-orbital pairings are the ones tending to stabilize the $s_{\pm}$ state [42]. It turns out that we find a very similar behavior as in the RPA approach.

Next, we try to include again pairings only coupling next nearest neighbors giving rise to the $s_{\pm}$ state, but this time, we include both intra and inter terms (see Fig. 4.3 in Chapter 4). For the first time, we find the behavior we were looking for, i.e. both coexistence and competition of superconductivity and magnetism. Thus we proceed with this choice of pairings.

Then, we solve the BdG equations (see Eq. 2.20 in Chapter 2) for different temperatures and different values of the external magnetic field B. We obtain the magnetic moment of the system and the superconducting order parameter for each temperature. We then proceed by Fourier transforming the magnetization and we plot the modulus square $|M(\mathbf{Q})|^2$ at the ordering vector $\mathbf{Q}$, which is proportional to what neutrons measure.

We start with the $B = 0T$ case and calculate the magnetization at different temperatures in the absence of superconductivity. The calculations are carried out by first calculating self-consistently the densities (see equations 2.23 and 2.24 in Chapter 2) and then the magnetization at each site, given by $m_i = \sum_{\mu}(n_{i\mu\uparrow} - n_{i\mu\downarrow})$. As shown in Fig. 5.3(a)(red curve), $|M(\mathbf{Q})|^2$ decreases as the temperature increases following the usual mean-field behavior [61] until it vanishes at T_N.

In the next step, we include superconductivity, and again calculate the magnetization for different temperatures (see Fig. 5.3(a)(blue curve)). We also calculate the SCOP (see Eq. 2.25). We define the pair potential at site i as

$$\Delta'_i = \frac{1}{4}\sum_{\mu}(\Delta'_{i,i+\hat{x}+\hat{y},\mu} + \Delta'_{i,i-\hat{x}-\hat{y},\mu} + \Delta'_{i,i+\hat{x}-\hat{y},\mu} + \Delta'_{i,i-\hat{x}+\hat{y},\mu}) \tag{5.15}$$

where $\Delta'_{i,j,\mu} = \Delta_{i,j,\mu} e^{-i\frac{e}{\hbar}\oint_j^i \mathbf{A}\cdot\mathbf{ds}}$ and the phase is the Peierls phase (see Eq. 3.6 in Chapter 3). This makes it possible to plot the SCOP at each site, which is a quantity connecting two sites except for the case of onsite s-wave. This quantity gives a measure of the strength of superconductivity and it also provides T_c.

At $T = 0.01eV/k_B$, the size of the superconducting gap is approximately $45meV$ and it vanishes approximately at $T = 0.027eV/k_B$(see Fig. 5.3(b)). In Fig. 5.3(a) we see how, below T_c, the superconductivity suppresses the magnetization. But as the temperature increases, the strength of the superconductivity decreases (the size of the gap, see Fig. 5.3(b)). Thus, the suppression exerted by SC on m due to the competition of the two different orders, decreases, leading to an increase of the moments until T_c is reached (see Fig. 5.5) and superconductivity vanishes (see Fig. 5.7). Above this temperature, the magnetization decreases again in the previously mentioned mean-field way. Thus, we see that the magnetization and the superconductivity both coexist and compete below T_c, as they find in the experiments [63].

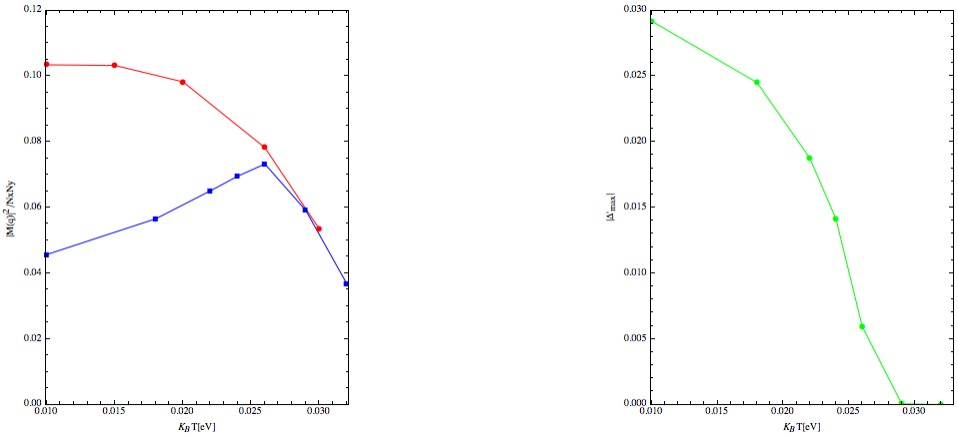

(a) (b)

Figure 5.3: (a)The red and blue lines denote the square of the $(\pi, 0)$ peak of the the Fourier transform of the magnetization $M(\mathbf{r})[\mu_B]$ versus temperature T$[eV/K_B]$. The red corresponds to $\Gamma_{\mu\mu\mu\mu} = \Gamma_{\mu\nu\nu\mu} = 0eV$ and the blue to $\Gamma_{\mu\mu\mu\mu} = \Gamma_{\mu\nu\nu\mu} = 0.117eV$. The other parameters are $U = 0.97eV$, $J = U/4$, and $B = 0T$. (b)The green line denotes the strength of superconductivity $|\Delta'_{max}|$ at different T for the same parameters and $\Gamma_{\mu\mu\mu\mu} = \Gamma_{\mu\nu\nu\mu} = 0.117eV$.

Nxt, we proceed by performing the same calculation for different values of the external magnetic field. As shown in Fig. 5.4(a), we find that below T_c, the magnetic field enhances the magnetic order and that above T_c, where there is no superconductivity and therefore no vortices, it follows the same behavior as the zero field case. We also find that, T_c is lower in the $B \neq 0$ cases than in the $B = 0$ case and that the higher the B field, the larger the enhancement of the magnetization, see Fig. 5.4(a).

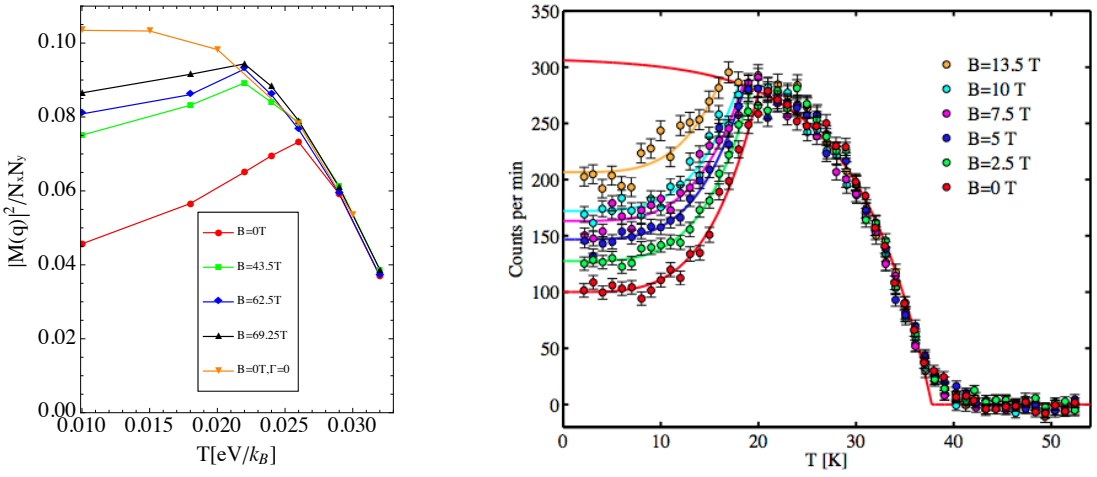

(a) (b)

Figure 5.4: (a)Amplitude of the $(\pi, 0)$ peak of the Fourier transform of the magnetization $M(\mathbf{r})[\mu_B]$ versus temperature T for $\Gamma_{\mu\mu\mu\mu} = \Gamma_{\mu\nu\nu\mu} = 0$ (orange curve) and $\Gamma_{\mu\mu\mu\mu} = \Gamma_{\mu\nu\nu\mu} = 0.117$ (red, green, blue and black curves). The other parameters are $U = 0.97eV$, $J = U/4$, and $B = (0, 43.5, 62.5, 69.25)T$ respectively. (b)Experimental measurement of the Bragg peak in $Ba(Fe_{0.95}Co_{0.05})_2As_2$ [63].

To understand this effect, we calculate the magnetization in real space m_i shown in Fig. 5.5.

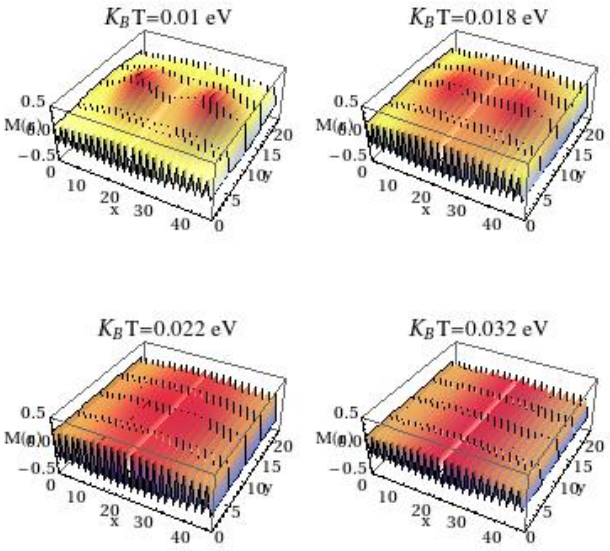

Figure 5.5: Real space plot of the total magnetization m_i at different temperatures T for $B = 43.5T$, $\Gamma_{\mu\mu\mu\mu} = \Gamma_{\mu\nu\nu\mu} = 0.117eV$, $U = 0.97eV$ and $J = U/4$.

In Fig. 5.5, one can see how the magnetization is enhanced in the vortices. Below T_c ($T_c \sim 0.027eV/k_B$), we see how as the temperature increases, the magnetization out of the vortex cores increases. This is because, as shown in Fig. 5.7, the strength of the superconductivity out of the vortices decreases, lowering its suppression on the magnetization. This is what makes $|M(\mathbf{Q})|^2$ increase, as T goes up below T_c, in Fig. 5.4(a). At $T = 0.032eV/k_B$, which is above T_c, there is no superconductivity at all (see Fig. 5.7) and the stripe ordered magnetization is again homogeneous(there is actually some small modulation of m but this is caused by finite size effects (see Section 3.4 in Chapter 3)). To see explicitely what the magnetic field does to the magnetization, we compare, for the same temperature, $B = 0T$ and $B = 69.25T$ in Fig. 5.6. Thus, what is causing the enhancement of the magnetic order as we increase the field, is the fact that the moments become larger in the vortex cores, and the enhancement increases as B goes up. There is some enhancement also outside the vortices but this is due to the not sufficiently large system size, the magnetic field penetrates through the whole system (even though it mainly penetrates in the vortex cores). If the system was large enough, the enhancement would be zero far enough from the vortex center.

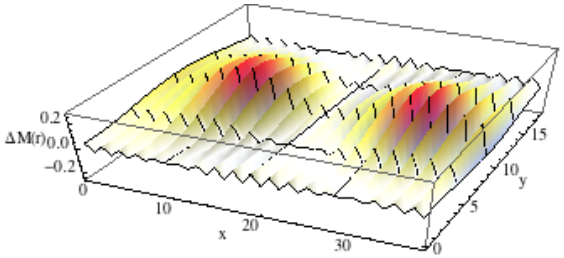

Figure 5.6: Real space plot of the vortex-enhanced magnetization $\Delta M(\mathbf{r}) = M(\mathbf{r}, B = 69.25T) - M(\mathbf{r}, B = 0T)$. The other parameters are $\Gamma_{\mu\mu\mu\mu} = \Gamma_{\mu\nu\nu\mu} = 0.117eV$, $U = 0.97eV$ and $J = U/4$.

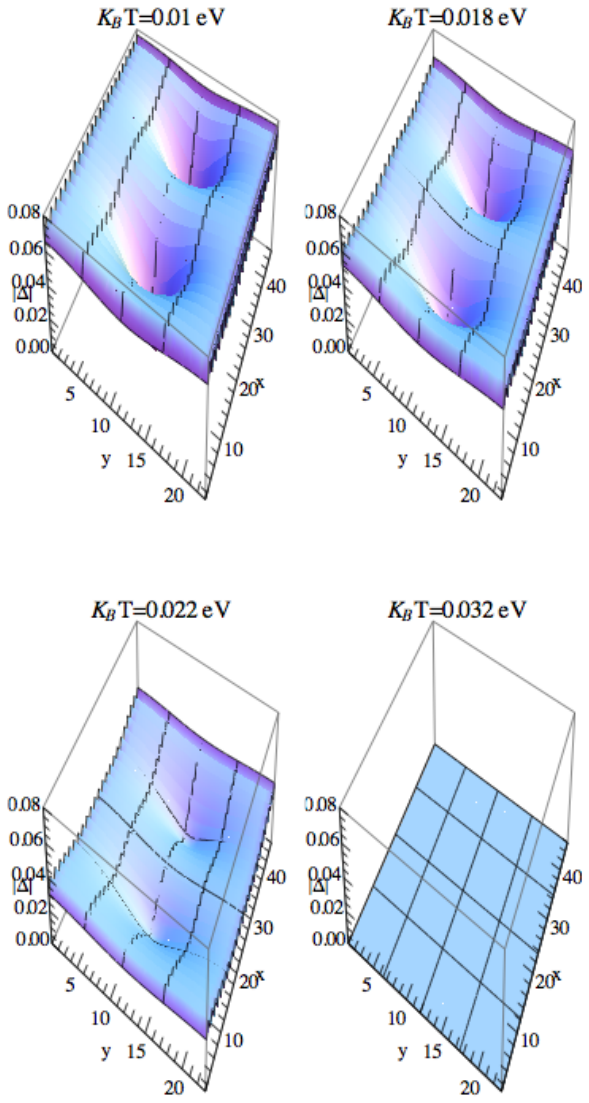

Figure 5.7: Modulus of the SCOP $|\Delta'_{max}|$ for different temperatures T (see Eq. 5.15). The other parameters are $B = 43.5T$, $\Gamma_{\mu\mu\mu\mu} = \Gamma_{\mu\nu\nu\mu} = 0.117eV$, $U = 0.97eV$ and $J = U/4$.

The reason why the magnetization is enhanced in the vortices, is that vortices strongly suppress the superconductivity in the vortex cores. Due to this suppression, low energy bound states arise in the superconducting gap around the Fermi level. Now, in a simpler one-band system, the spin susceptibility is given by Eq. (5.2), where the bare susceptibility (for an infinite 2d system) is

$$\chi_0(\mathbf{k}, w) = 2 \int \frac{d\mathbf{p}}{(2\pi)^2} \frac{f(\xi_{\mathbf{p}+\mathbf{k}}) - f(\xi_{\mathbf{p}})}{\xi_{\mathbf{p}+\mathbf{k}} - \xi_{\mathbf{p}} - (w + i\eta)} \tag{5.16}$$

.

In the static long-wave limit $q \to 0$ and $w = 0$, $\xi_{\mathbf{p}+\mathbf{q}} \to \xi_{\mathbf{p}}$ and performing a Taylor expansion in energy

$$\chi_0(\mathbf{k},0) \to -2\int \frac{d\mathbf{p}}{(2\pi)^2}\frac{(\xi_{\mathbf{p}+\mathbf{k}}-\xi_{\mathbf{p}})\frac{\partial f}{\partial \xi_{\mathbf{p}}}}{\xi_{\mathbf{p}+\mathbf{k}}-\xi_p} = \int d\xi_{\mathbf{p}} DOS(\mu_0+\xi_{\mathbf{p}})\left[-\frac{\partial f}{\partial \xi_{\mathbf{p}}}\right] \tag{5.17}$$
$$\simeq DOS(\epsilon_F), \quad \text{for} k_B T \ll \epsilon_F$$

where $DOS(\epsilon_F)$ is the density of states at the Fermi level. Thus, in this approximation, the one-band spin susceptibility reduces to

$$\chi^{RPA}(\mathbf{k},0) \to \frac{DOS(\epsilon_F)}{1-UDOS(\epsilon_F)}. \tag{5.18}$$

Hence, the increase of $DOS(\epsilon_F)$ in the vortex cores, might lead to the local crossing of the Stoner instability, giving rise to static magnetization.

5.5 Conclusions

The magnitude of the calculated gap is too large, compared to the one found in experiments. Some STM measurements on 1111 materials reported, that the size of the gap (half of the distance between the two coherence peaks of the DOS) is 9.3 meV for $NdFeAsO_{0.86}F_{0.14}$ [57] and 7 meV for $SmFeAsO_{0.8}F_{0.2}$ [18]. But, we know that we are not putting the right superconducting pairing, in the sense that we do not generate them using a microscopic theory and that we tune them such that the gap is approximately one order of magnitude larger than in the experiments. This is because, due to the computational limit, both regarding memory and calculation time, we cannot perform the calculations in systems as large as we would need. Thus, because we need room for the the vortices, we are forced to make them smaller (shorter coherence length ξ), and this is achieved by increasing the gap size. One could try and be more careful by trying to put a realistic pairing and see if we can get this coexistence and competition, but with a realistic gap size. Unfortunately, currently we do not know what is the pairing in the magnetic state, which is the suitable one for this calculation. Hence, we are not aiming for quantitative results but qualitative. Secondly, both the calculated T_c and T_N are almost one order of magnitude larger than the real ones, for example in the case of $NdFeAsO_{0.86}F_{0.14}$ $T_c = 48K$ [57] and our calculated T_c is approximately 0.026 eV/k_B, which corresponds to $\sim$ 302 K. But it is well known (Mermin-Wagner-Hohenberg theorem) that mean-field theory over-estimates the size of the order parameters (the mean-fields) by neglecting the fluctuations. This large quantitative disagreement of e.g. the critical temperatures is simply a consequence of this over-estimation.

Despite the quantitative disagreement, we have understood the results found by Stieper *et al.*[63].

- Below T_c, the magnetization increases as T increases because, as shown in Fig. 5.3(b) and Fig. 5.7, superconductivity decreases, thus the suppression exerted on the magnetism decreases. This enhancement is clearly seen around the vortices and below T_c in Fig. 5.5.
- When a magnetic field is applied, the magnetic moments in the vortex cores become larger as shown in Fig. 5.6, and the larger the field, the larger this enhancement is. It is due to this enhancement that $|M(\mathbf{Q})|^2$ is enhanced by the B field as shown in Fig. 5.4(b).
- Regarding the choice of pairings intra ($\Gamma_{\mu\mu\mu\mu}$) and inter ($\Gamma_{\mu\nu\nu\mu}$) only for next nearest neighbors, we have still not fully understood why this works and why the full RPA result does not. We are aware of the fact that, when we generate the RPA pairing, this corresponds to the non magnetic state, thus in principle this is wrong. But we do not know yet, what are the pairings in the magnetic state. The main differences between our choice and the full RPA are that we only couple next nearest neighbors (NNN) whereas RPA couples all up to NNN and

that we only take into account the intra and inter couplings whereas RPA takes into account all orbital combinations. Also, the inter pairings in our choice are larger (one and two orders of magnitude) than the ones in the RPA, they are actually as large as the intra ones. This is an ongoing project and we are currently trying to figure out what is the pairing structure that makes the superconductivity and magnetization couple in our model. It could be that the magnetic state enhances the inter pairings between next nearest neighbors. We strongly believe that, what is giving rise to the competition between superconductivity and magnetism is the enhanced inter pairings, compared to the RPA case. We are approaching to that conclusion.

Chapter 6

Vortices in LiFeAs

In this chapter we will study the low energy bound states in the vortex core of LiFeAs. In doing so, we will try to qualitatively reproduce some recent experimental results from [28]. The study of vortices is related to the study of impurities because one could consider a vortex a complex impurity. But there is a difference: whereas in the impurity study there is an ambiguity, namely, the strength of the scattering potential per orbital of the impurity which we do not know, in the vortex study, there is no such ambiguity, the vortex is what it is, once one introduces the magnetic field correctly in the Hamiltonian. This is great because it gives the opportunity to understand these materials. If we believe that we have the right band structure and that we understand what is the pairing mechanism leading to the quantitatively right gap structure, we should be able to reproduce the experimental results.

The LiFeAs is an 18 K superconductor that presents several novel features compared to other FeSC. Among others, it has neither magnetic nor structural transitions, as for example 122 and 1111 materials do, although there are very strong magnetic fluctuations [39]. It is also one of the few superconductors which does not require additional charge carriers to superconduct.

6.1 Band structure of LiFeAs

For LiFeAs, high-quality crystals with atomically flat non polar surfaces are possible to prepare. It has been shown that the electronic structure on the surface is the same as in the bulk [45]. This implies that this material, and in general 111 materials, are ideal for surface spectroscopies like angle-resolved photoemission (ARPES) and scanning tunneling microscopy (STM) [28]. ARPES experiments [8, 67, 27] and density functional theory (DFT) [45, 27] reported a Fermi surface very different from the conventional set of hole and electron pockets predicted by DFT for the other FeSC. Concretely, it was observed that the nesting of hole and electron pockets was not very strong, leading to the suggestion that this was the reason for the absence of magnetism in this parent compound [8]. One of the issues related to the agreement between theory and experiment is related to the size of the inner (α_1, α_2)(see Fig. 6.1(b)) hole pockets centered at $(0, 0)$ of the BZ. ARPES observations find they are very small and even negligible whereas DFT calculations find they are relatively large. ARPES observes a single holelike band (α_2) crossing the Fermi surface near Z ($\mathbf{k} = (0, 0, \pi)$), while a second holelike band (α_1) is pushed below the Fermi level [8]. This suggest that the spin-orbit coupling, which will split the two bands [68], may be relevant. Recently, local-density approximation (LDA) + dynamical mean-field theory (DMFT) calculations have presented a picture which suggests that the 111 are considerably more correlated than, e.g., the well-studied 122 materials and have argued that stronger interactions lead to a shrinkage of the inner hole pockets but maintenance of the electron pocket size and shape [19, 72, 46].

For our simulations, the band structure for LiFeAs was obtained using DFT in a plane wave basis set with ultrasoft pseudo potentials provided in the Quantum ESPRESSO package [24]. To obtain the five-orbital tight-binding band used, the bands in the vicinity of the Fermi energy where projected on the five Fe $3d$ orbitals using maximally localized Wannier functions following the method of Marzari and Vanderbilt [50]. The DFT given band was a 3D band. In order to have a 2D band, we take a cut of the FS at $k_z = 0$.

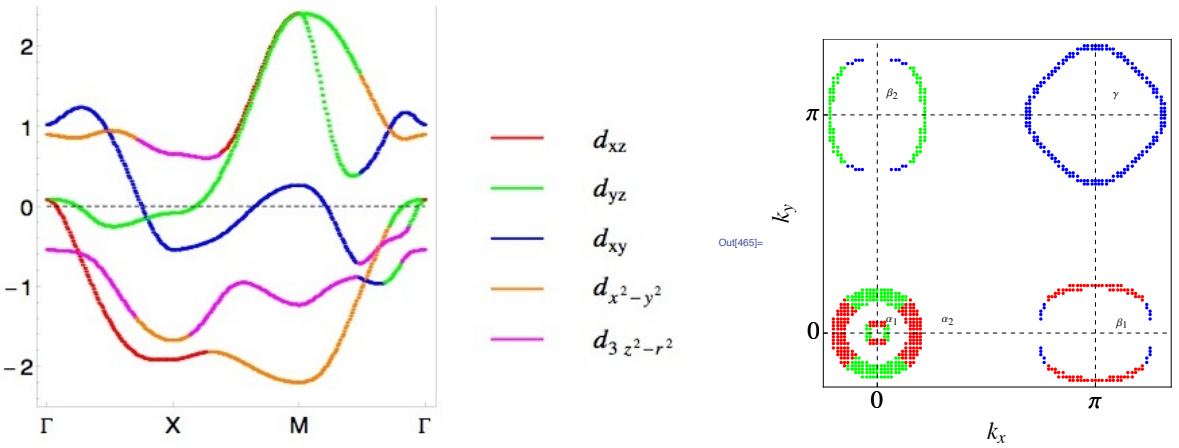

(a) (b)

Figure 6.1: (a) Orbitally resolved band structure with Γ, X and M denoting the symmetry points in the BZ corresponding to the one Fe unit cell [20].(b) FS in the unfolded BZ (five-band model) for LiFeAs at $k_z = 0$, electron filling n=6.0 and with colors indicating majority orbital character. The pockets at Γ and M are hole pockets and the ones at X and Y are electron pockets.

6.2 Gap structure of LiFeAs

ARPES measurements below T_c show that the superconducting gap in LiFeAs is the largest on one of the Γ centered α pockets (see Fig. 6.2(b), (c)), at the k_z where it exists. The gaps on the γ and β pockets are somewhat smaller, between 3 meV and 4 meV. As shown in Fig. 6.2, the gaps, even though they do not show true nodes, they do show anisotropy along the FS: the gap on the γ pocket has a $cos4\theta$ variation along the FS and the gaps on the two β pockets vary nearly as $\pm|cos2\theta|$[67, 9]. Probably, the gap on the α pocket also has an angular dependence, but the pocket is too small to detect the angular dependence along it in ARPES measurements [67][9](see Fig. 6.2)(a).

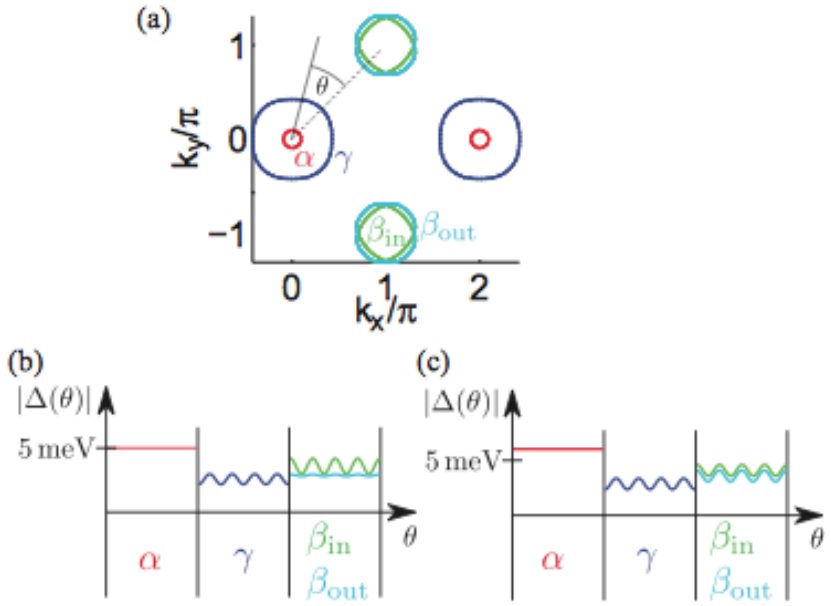

Figure 6.2: (a)The cut of the Fermi surface of the ARPES-derived tight-binding model in the 2 Fe BZ(folded BZ) (filling n=6.0) at $k_z = \pi$ to show the definition of the various pockets and the angle θ that parametrizes the surface points. Sketch of the results of the gap $|\Delta(\theta)|$ as seen in recent ARPES experiments compiled from the fits provided in (b)[67] and (c)[9]. This figure was taken from [68].

The absence of nodes, rules out a pure non s-wave state, as d-wave for example. Other states as $s + id$ or $p + ip$ are possible. However, the $\cos 4\theta$ gap modulated anisotropy on the γ pocket strongly suggests that the gap is s-wave [2]. The issue which ARPES cannot resolve, is whether the state is the conventional $s_\pm$ state with a sign change between the hole and electron pockets or another kind of s-wave state with for example a sign difference between the two Γ centered hole pockets, or not sign changes at all. The quasiparticle interference experiments can measure the relative sign between pockets, but so far there is no conclusive data for LiFeAs [3, 31, 11].

On the theoretical side, there is no agreement between the different studies of the gap structure in LiFeAs. Wang *et al* [68] studied the superconductivity in LiFeAs within the RPA approximation, using a ten orbital model fitted to match the FS measured by ARPES experiments. They found, a conventional $s_\pm$ state, driven by (π, π) interaction between fermions near hole and electron pockets. They calculated the ratios of the gaps found for the γ and β pockets, which agreed with the experimental results. On the other hand, their calculations disagreed with the experiment in that they found the smallest gap to be in the α pockets, which the ARPES experiments did not. Ahn *et al.*[2], used a different approach than RPA to analyze superconductivity in LiFeAs. They considered J/U as a parameter, converted from orbital to band basis, decoupled the interactions into orthogonal s-wave, $d_{x^2-y^2}$, and d_{xy} channels, and approximated each interaction by the leading and subleading angular harmonics, consistent with the given symmetry (see [2] for more details). They found four possible s-wave configurations (see Fig. 6.3) and concluded that the state which had the best overlap with ARPES, in which the largest gap occurred in the α pocket, was the one in which there was a sign change between the inner α hole pockets (see Fig. 6.3)(A).

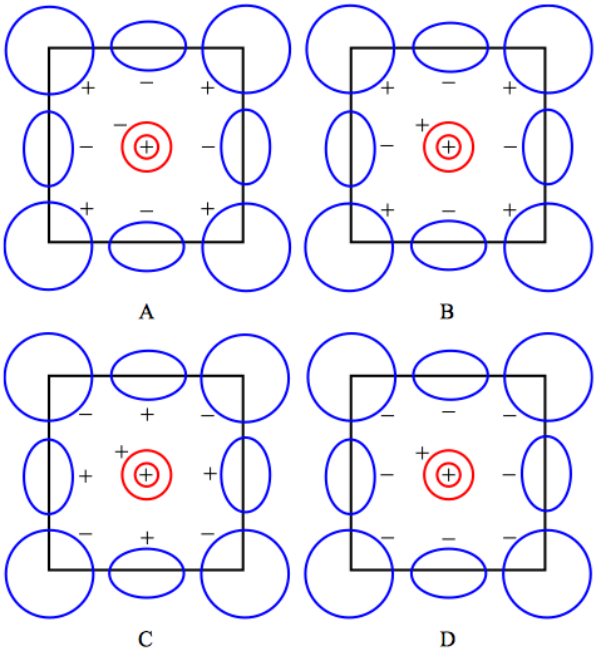

Figure 6.3: Four different s-wave solutions at $k_z = \pi$. Red color corresponds to the α pockets and blue correspond to the β and γ pockets. The "conventional" $s_{\pm}$ state is the state B. The gap structure of the state A has the best overlap with ARPES data.

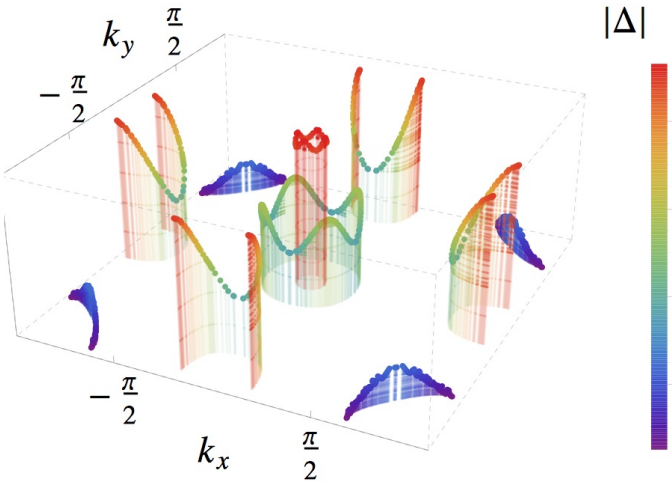

Figure 6.4: Size of the magnitude of the superconducting gap at the different pockets of the FS.

In our model, regarding the pairing, we take two different approaches. We first start by taking a more naive approach in which we put by hand some value for the superconducting pairing, just coupling the same orbitals and next nearest neighbors, giving rise to an $s_{\pm}$ state. In the second more realistic approach, we generate the pairings within the RPA approximation, following the steps in Chapter 4. The RPA susceptibilities are peaked near $(0, \pm\pi)$ and $(\pm\pi, 0)$ favoring an $s_{\pm}$ state and indeed the calculations yield a fully gapped $s_{\pm}$ state. Fig. 6.4 shows the magnitude of the gap on the various pockets.

6.3 Local density of states in LiFeAs

Because superconductivity is strongly suppressed or even destroyed at the core of the vortices, the vortex core can be regarded as a potential well surrounded by the superconducting gap (SG) and the circulating supercurrents. Therefore, the quasiparticle states in the vortex core can provide useful information about the SG structure.

Hanaguri *et al* [28] investigated vortices in LiFeAs using scanning tunneling microscopy/spectroscopy. For the zero-field case, the tunneling spectra show two superconducting gaps without detectable spectral weight near the Fermi energy, evidencing fully gapped multi-band superconductivity. For B=0.5T, the spectrum at the center of the vortex exhibits a pronounced peak just below E_F (-0.9 mV) as well as some other weaker peaks as shown in Fig. 6.5(a). They also looked at the spatial evolution of the tunneling spectrum along the Fe-Fe and As-As directions as shown in Fig. 6.5(b),(c). The LDOS peak at ∼-0.9 mV shifts farther away from E_F with increasing distance from the vortex center and smoothly approaches the smaller SG. The counter branch is also observed at symmetric energies above E_F, although the intensity is much weaker near the vortex center. There is an energy-gap-like feature apparent at E_F even at the vortex center. The spectral weight at low energies is higher along the As-As direction than along the Fe-Fe direction. They also looked at the real space evolution around a vortex of LDOS at different energies (see Fig. 6.6) and found that the vortex-core state at E_F exibits a four-fold star shape with high LDOS tails along the nearest As-As directions. Each tail splits in parallel with increasing energy.

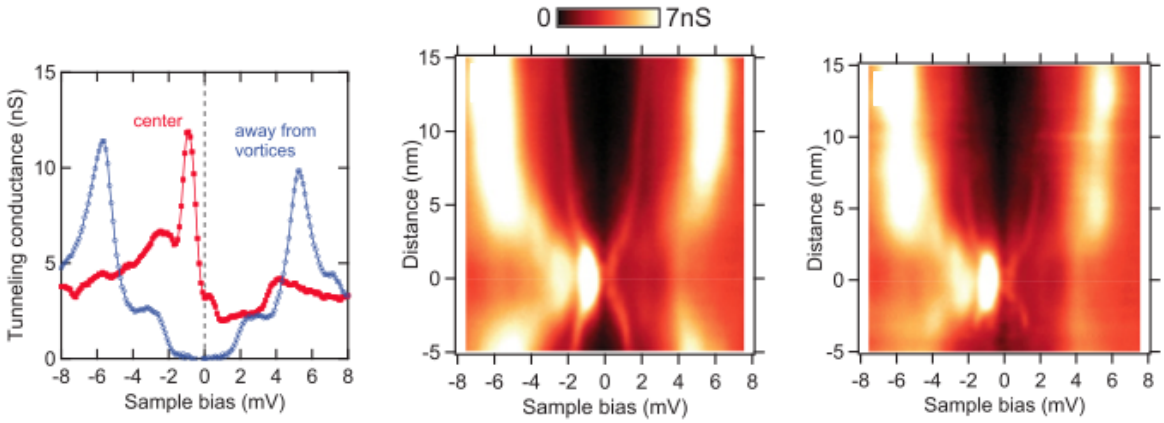

(a) (b) (c)

Figure 6.5: (a) Tunneling spectra taken at the center of the vortex (red) and away form vortices (blue).(b) Line profiles of tunneling conductance across the vortex center along the nearest Fe-Fe direction.(c) Along the nearest As-As.

This group claim that, the four-fold star shape is due to the shape of the Fermi surface. At low energies, the LDOS distribution around a vortex is mainly governed by the smallest SG and the Fermi surface where it opens. In LiFeAs, ARPES observed the smallest SG in the outermost hole cylinder [67] and this has a rounded square cross section with a flat region perpendicular to the As-As direction[8], which explains the four-fold star shape.

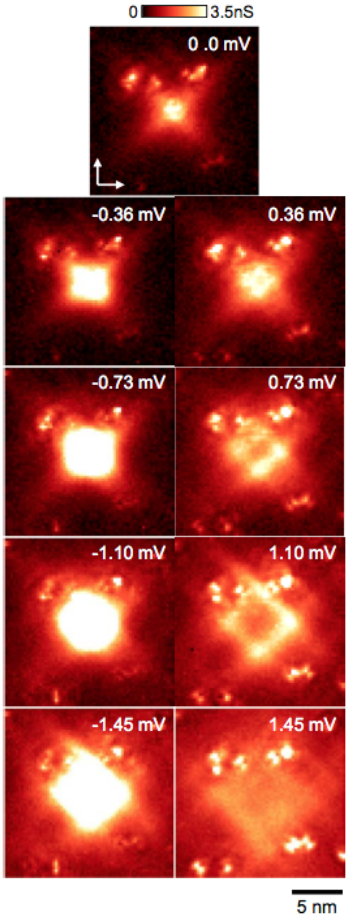

Figure 6.6: Tunneling- conductance images around a single vortex at different energies. Arrows denote the nearest Fe-Fe direction. The As-As direction is in 45° with respect to the Fe-Fe direction. (The negative energy spectrums are unpublished data.)

6.4 Results

In this section, we will show the results of our calculations of the local density of states in LiFeAs vortices. We perform the calculations for two different approaches regarding the pairing. We start by ignoring the microscopic origin of the interaction that pairs the electrons. Based on the experimental results which, although they do not show complete evidence, hint that the pairing symmetry in this material is $s_{\pm}$ [64], we put by hand next nearest neighbor attractive interactions which correspond to this symmetry of the SCOP in momentum space (see Section 1.4.2 in Chapter 1). In this first approach, we only consider the intra-orbital pairings and we do not include the Hubbard term H_{int}^{MF} (see Eq. 2.15 in Chapter 2). We then take a more sophisticated approach and we do the RPA approximation to calculate the pairing, following Chapter 4. In the last step, we include H_{int}^{MF} and study its effect on the LDOS, within the RPA approximation.

6.4.1 Intraorbital phenomenological pairing

In this section we do not include H_{int}^{MF} in the Hamiltonian, thus

$$H = H_0 + H_N + H_{BCS}^{MF} + H_Z. \tag{6.1}$$

As mentioned, the superconducting pairing used in this section, have a phenomenological origin and not microscopic (like RPA for example).

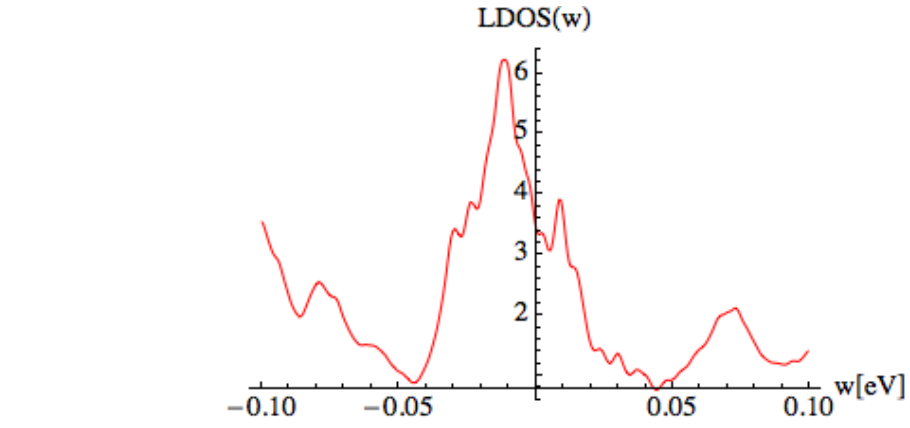

(a)

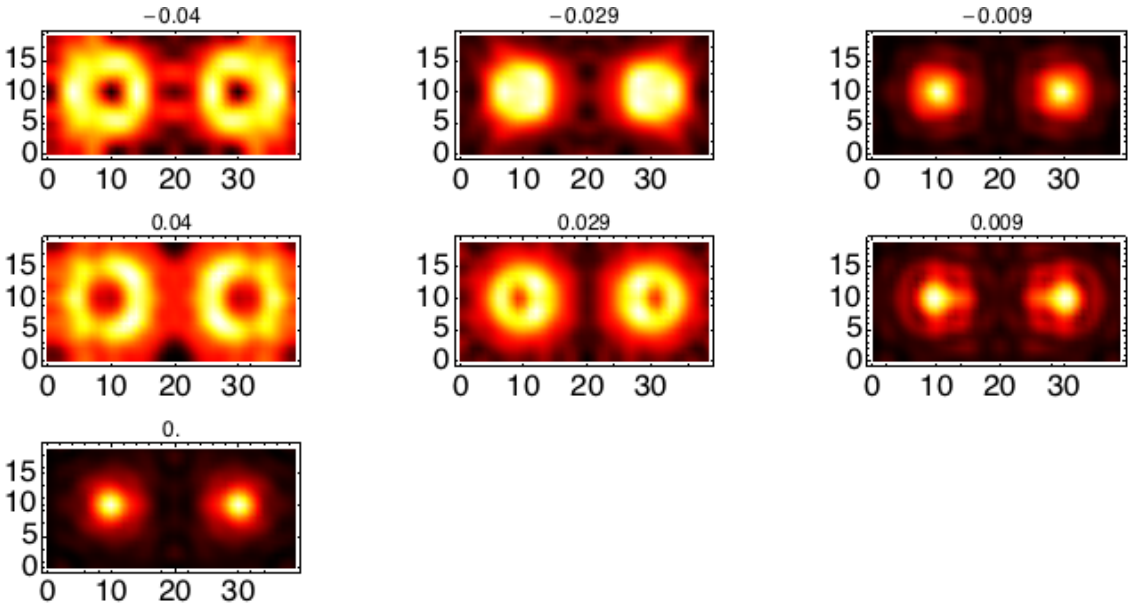

(b)

Figure 6.7: Total LDOS, with $B = 62.5T$, $\Gamma_{NNN} = 0.51eV$ and $U = J = 0eV$. The superconducting gap in the bulk, where the magnetic field does not penetrate(or the gap for $B = 0T$ case) is $\sim 50meV$.(a)Energy resolved LDOS at the vortex core with smearing $\eta = 0.5$.(b)Space resolved LDOS for different energies given above each plot in eV, with $\eta = 0.3$.

The spectra at the vortex core shown in Fig. 6.7(a), shows the main feature which is the highest intensity of LDOS just below the Fermi energy, similar to the experimental result in Fig. 6.5(a), as well as a smaller peak above the Fermi energy. The real space resolved LDOS in Fig. 6.7(b), are quite different from the ones in Fig. 6.6 but one can pick up some similarities. In the Fig. $6.7(b)(w = -29meV)$, LDOS is peaked at the center of the vortex and there are four density tails coming out with 45° with respect to the Fe-Fe direction, each of them split up into two tails, similar to the experimental result shown in Fig. $6.6(w = -1.45mV)$. There is an extra tail at the center of the plot in Fig. $6.7(b)(w = -29meV)$ overlapping the two vortices. Another similarity is that, similar to the couple Fig. $6.6(-1.10mV)$ and $(1.10mV)$, the couple

Fig. 6.7($w = -29meV$) and ($w = 29meV$), their LDOS peaks at the center of the vortex core, below the Fermi energy, whereas above the Fermi level, there is no spectral weight; the states surround the vortex core as a ring. But whereas in Fig. 6.6 ($1.10mV$) the states surrounding the core peak at the four corners of a square with edges with 45° with respect to the Fe-Fe directions, in Fig. 6.7($w = 29meV$) they rather peak in three points. At energies nearer from zero in Fig. 6.7(b), it is not possible to appreciate a four-fold star shape as in the experiment.

6.4.2 RPA pairing

$U = J = 0eV$

Next, we take a more sophisticated approach and use the RPA approximation to calculate the pairing, following Chapter 4. As a check (we put a non zero U for this check), we start by looking at the zero field case. We see that the LDOS in Fig. 6.8 qualitatively agrees with the experimental result shown in Fig. 6.5(a) measured away from the vortices (blue line).

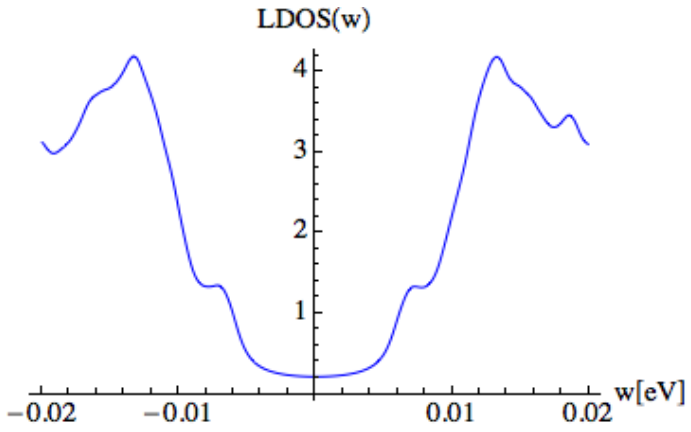

(a)

Figure 6.8: LDOS with $B = 0T$, $U_{RPA} = 0.865eV$, $U = 0.865eV$ and $J = U/4$. U_{RPA} is the U we use to generate the pairing (see Chapter 4).

We then proceed by introducing an external magnetic field and calculate the LDOS (see Fig.6.9). Regarding the spectra at the vortex core, the only difference with respect the previous more naive calculation shown in Fig.6.7(a), is that the smaller peak above the Fermi level has become more pronounced and that the larger peak below the Fermi energy has split into two sub peaks. It still qualitatively resembles the experimental result in Fig.6.5(a). Regarding the real space LDOS shown in Fig. 6.9(b), it is still quite different from the experimental ones and still no clear four-fold star shape at energies near zero, hence there is no major change from the previous calculation.

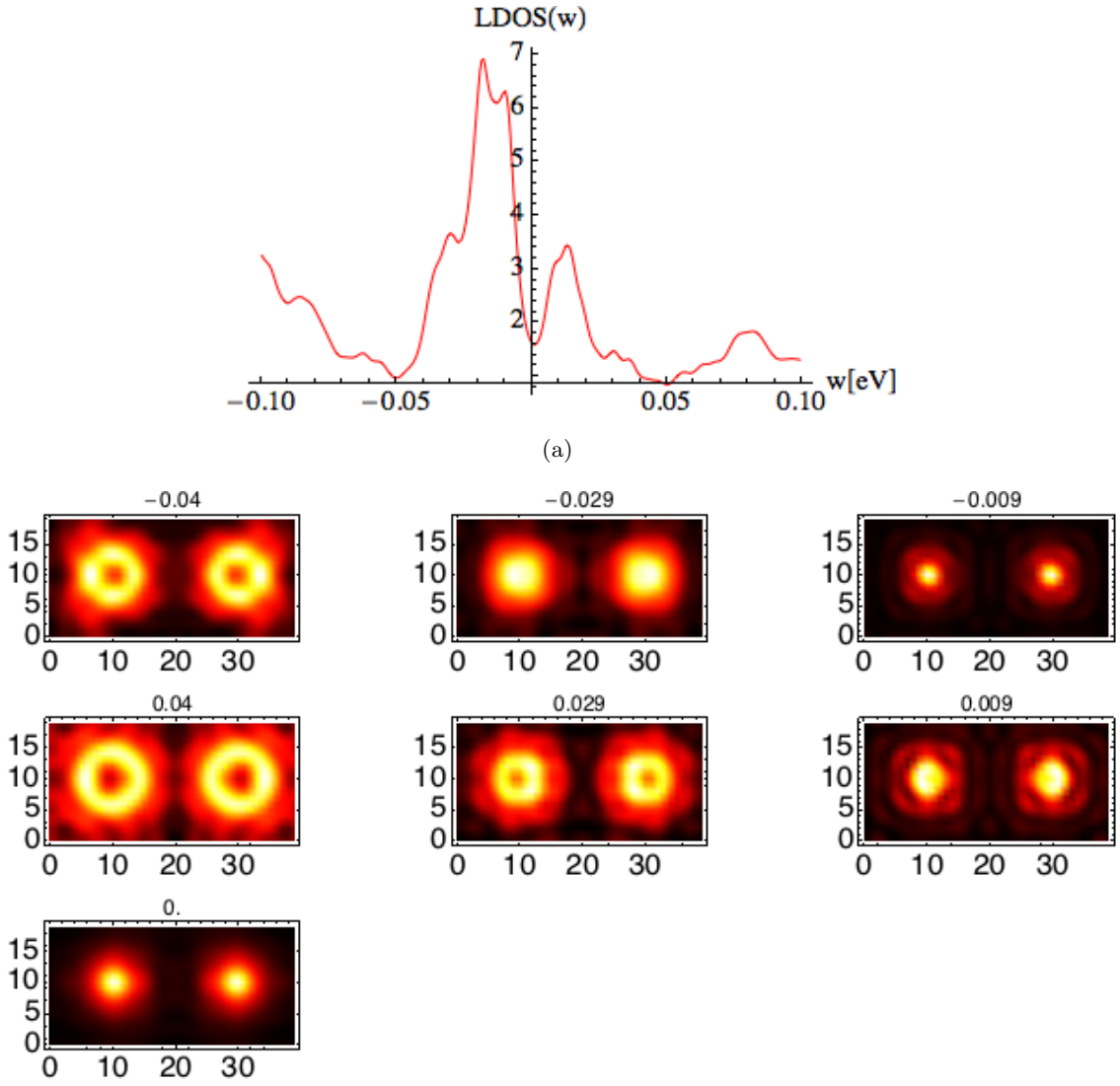

(a)

(b)

Figure 6.9: Total LDOS with $B = 62.5T$, $U_{RPA} = 0.9eV$, $U = 0eV$ and J=U/4. The superconducting gap in the bulk, where the magnetic field does not penetrate(or the gap for $B = 0T$ case) is $\sim 50meV$.(a)Energy resolved LDOS at the vortex core with smearing $\eta = 0.6$.(b)Space resolved LDOS for different energies given above each plot in eV with $\eta = 0.3$.

$U = 0.86eV$ & $J = U/4$

Now, in order to take a more realistic approach, we include the H_{int}^{MF} term, thus

$$H = H_0 + H_N + H_{int}^{MF} + H_{BCS}^{MF} + H_Z. \tag{6.2}$$

Until now, we have not included the Hubbard term (H_{int}^{MF}) in the Hamiltoanian, i.e. $U = J = 0$ (we actually did include it once, but only to check the $B = 0T$ case in Fig. 6.8). Now, we include this term and study its effect on the LDOS. We use again the pairing within the RPA approximation. We tune U such that it stays below U_{c2} above which the system orders magnetically. Even so, as explained in Chapter 5, vortices induce or enhance the magnetization in the vortex cores as seen in Fig. 6.11. In Fig. 6.11(a), we see the case where the system orders

magnetic even in the absence of vortices, since there is a finite magnetization even out of the region where the B field penetrates the system. On the other hand, as we decrease U and go below U_{c2} as in Fig. 6.11(b), the magnetization disappears everywhere but in the vortex cores. In Fig. 6.11(c), there is actually some magnetization nucleated in the vortex cores even in the absence of interactions ($U = J = 0$) due to the Zeeman term (see Eq. (2.14)).

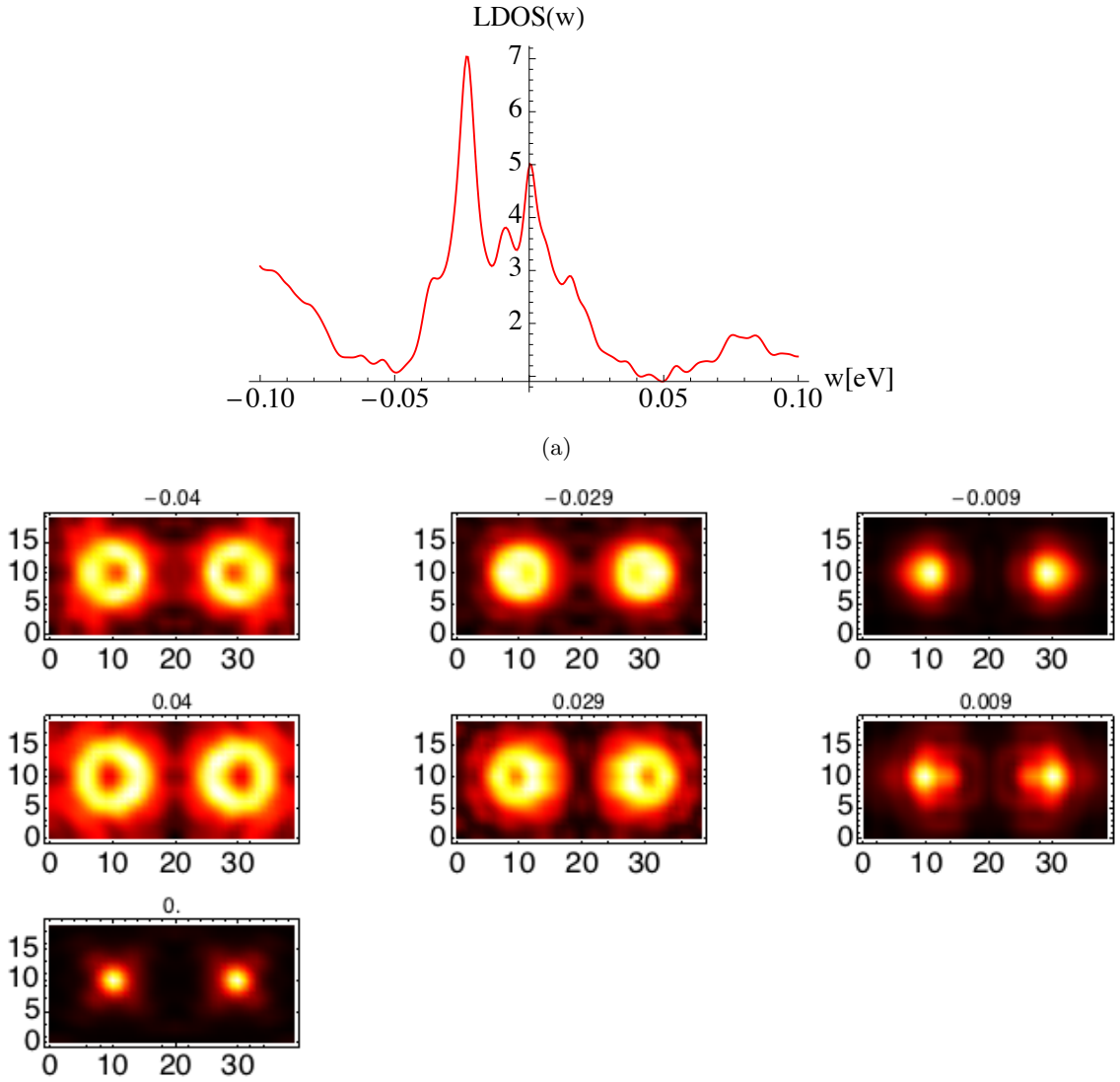

(a)

(b)

Figure 6.10: Total LDOS with $B = 62.5T$, $U_{RPA} = 0.9eV$, $U = 0.86eV$ and J=U/4. The superconducting gap in the bulk, where the magnetic field does not penetrate(or the gap for $B = 0T$ case) is $\sim 50meV$. (a) Energy resolved LDOS at the vortex core with smearing $\eta = 0.6$. (b) Space resolved LDOS for different energies given above each plot in eV with $\eta = 0.3$.

The main differences in this new calculation shown in Fig. 6.10 are the following: First in Fig. 6.10(a), the highest peak below the Fermi energy has become thinner and single-peaked and a new smaller peak has formed just below zero energy. The peak above, has split into two peaks. Second, in Fig. 6.10(b), the most important difference is that, now that we included interactions in such a way that the system is not magnetic but vortices induced magnetization, we find the four-fold star shape LDOS at the Fermi energy, with states extending in 45° with respect to the

Fe-Fe direction. Because far from the Fermi energy ($w = -0.04eV$ and $w = 0.04eV$), the largest spectral weight is far from the vortex core approaching the system edges, is hard to tell what is the direction and shape of the tails coming out.

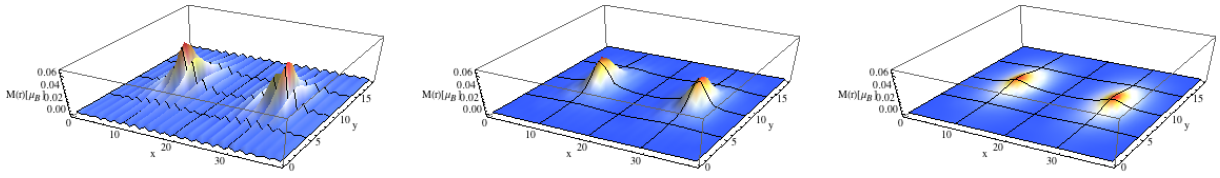

(a) (b) (c)

Figure 6.11: Real space magnetizetion for $B = 62.5T$ and $U_{RPA} = 0.9eV$. (a) $U = 0.88eV$, $J = U/4$. There is stripe order magnetization even out of the vortices, showing that we are above U_{c2}. (b) $U = 0.86eV$, $J = U/4$. The magnetization is enhanced in the vortex cores, but out of the core regions, there is no magnetization ($U_{c1} < U < U_{c2}$). (c) $U = J = 0$ ($U < U_{c1}$) there is no interactions and there is some magnetization in the vortices arising from the Zeeman term.

6.5 Discussion and conclusions

Wang *et al.* [69] studied the core anisotropy in LiFeAs within a semiclassical approximation by solving the Eilenberger equations and analyzed the LDOS distribution around a single vortex with the assumptions of various SG anisotropies (see Fig. 6.12). They did not do a self-consistent calculation for the SCOP but they put it by hand. Based on the fact that, the cross sections of the β_1 and β_2 electron pockets rotate by a full 180° along k_z direction, and since the gaps are larger (ARPES identified superconducting leading edge gaps of order 1.5-2 meV for the hole pockets, and 3 meV for the electron pockets [8]), they assume that the low-energy core states spatial anisotropy mainly comes from the hole pockets and they only take into account the γ pocket, which is the most anisotropic. In order to compare the influence of the gap structure versus the influence of the band structure on the shape of the vortex core states, they compare the LDOS calculated with a circular FS, with the case where the FS is a rounded square as the γ pocket in Fig. 6.1(b). In both cases, they put the same gap anisotropy, i.e. maximums of the gap in the direction As-As (45° with respect to the Fe-Fe direction) and minimums in the Fe-Fe direction. The given gap anisotropy favors the situation where the core states leak out in the Fe-Fe direction because of the gap minimum, which is the same in both cases. The circular FS favors the situation where the coherence length is not angle dependent(isotropic distribution of the core states), whereas the square FS favors a four-fold star shape of the vortex core states, with states leaking out in the As-As directions [69]. They find that, for the circular FS, the states leak out in the Fe-Fe direction as expected from the location of the gap minima. Instead, for the square FS case, they find that, even though the gap minimums favor a Fe-Fe leaking, the four tails of the star extend along the As-As direction, showing that the Fermi surface anisotropy in LiFeAs, is strong enough as to dominate over the gap structure. Thus, they associate the four-fold star shape of the low energy bound states found by Hanaguri *et al.* with the FS anisotropy of LiFeAs.

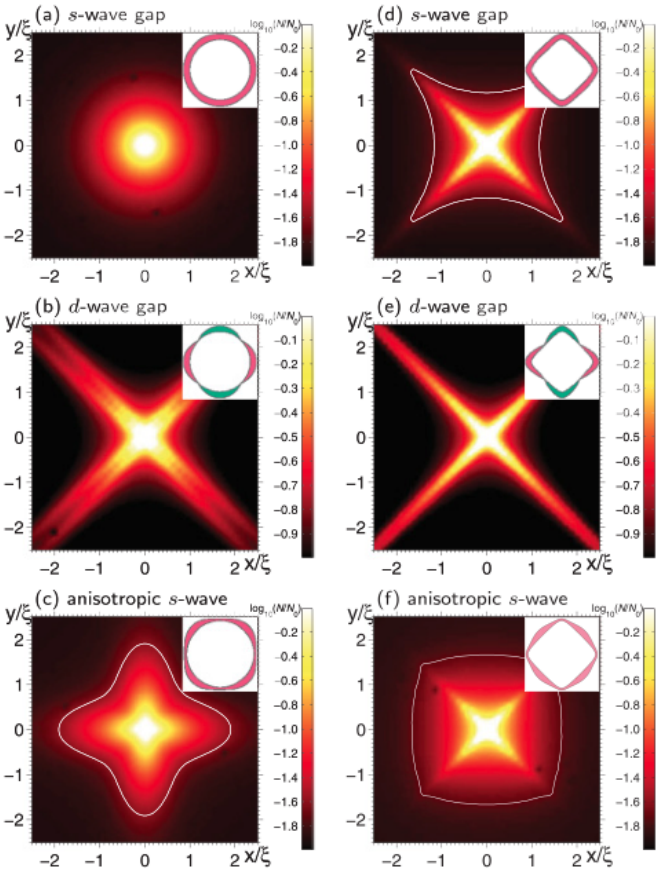

(a)

Figure 6.12: LDOS in the LiFeAs for different gap models with circular Fermi surface (a)-(c) and γ pocket (d)-(f): (a), (d) An isotropic s-wave gap Δ_0; (b), (e) a nodal d-wave gap: (c), (f) extended s-wave gap. Figure taken from [69].

In our model, the way the superconductivity opens a gap in the FS is shown in Fig. 6.4. As one can see, except for the inner hole pocket, which has a too large gap as to dominate the low energy states, the other hole pockets α_2 and γ have gap minimums in the Fe-Fe directions, which in principle would favor to have low-energy states leaking out in this direction. The anisotropy in the inner hole pocket α_1 is rotated 45° with respect to the anisotropy in the other hole pockets, which favors states to leak out in the As-As direction. Since in the most realistic case shown in Fig. 6.10 and Fig. A.1 in Appendix A, we find the leaking of the states nearer from the Fermi level in the As-As direction, we associate this shape of the LDOS with the square shape of the γ pocket, since as explained in [69], it causes quasiparticles from a large portion of the FS to travel along the As-As direction, forming large LDOS tails in this direction. As we go to energies further from the Fermi level, the As-As star shape vanishes and other shapes take place (see Fig. A.1 in Appendix A), which is due to the fact that this energy states belong also to other pockets. It might also be that the gap anisotropy dominates over the FS anisotropy at energies far from the Fermi level. For example, at energies very far from zero (see Fig. 6.10), although as previously mentioned is hard to tell features because of the small system size, we again roughly see the As-As direction star, which is consistent with fact that the largest gap located in α_1, which has the gap minima in this direction (see Fig. 6.4).

Regarding the other main feature of the LDOS in LiFeAs, i.e. the big peak below the Fermi

energy, we cannot analytically show why it is there, it just serves as a checking for our model, suggesting that is quite realistic. Some people did semi-analytics for the simpler one-band model [29] in the quantum limit and study the LDOS at the vortex core. They found that the intensity of LDOS should be quite asymmetric with respect to the Fermi level and this was associated with the lowest bound state.

The origin of the disagreement between our results with the experiments can be several. Due to the fact that in the calculation, the flux going through the magnetic unit cell (MUC) is fixed (see Section 3.2 in Chapter 3), the magnitude of the magnetic field is fixed by the system size. For a given magnetic flux, the larger the system, the smaller the magnetic field. Due to the numerical magnitude of doing realistic five band calculations, there is a limitation in doing calculations for low magnetic fields (large systems) as they do in experiments. Thus, we are forced to perform the calculations for unrealistically high magnetic fields, which means to put the wrong "impurity potential" in analogy to the impurity study. Another problem related to doing vortex state calculations is that the coherence length ξ (the radius of the vortex) increases as the size of the superconducting gap decreases. In the calculations we can tune the size of the gap by tuning the magnitude of the pairing. But, in order to reach the realistic gap magnitudes and at the same time have room for the vortices in the system, one has to go to computationally unaffordable large systems. Thus, we are forced to do the simulations with approximately one order of magnitude larger gaps. Another evident difference with the experiment is that, again, due to computational limitations, one cannot perform a calculation in a system where the two vortices are far enough as to not interact with each other, so they slightly overlap in the calculations. In the experiment, unless the flux is huge, the vortices are so far apart that one can consider the vortices to be not interacting with the neighboring vortices.

In conclusion, even with all the differences from the real experiment, we have still found very remarkable similarities, specially in the most realistic approach (see Fig. 6.10), where we use the RPA pairings and include the term H_{int}^{MF} in the Hamiltonian.

- Performing the most realistic approach to the problem so far, where we include 5 orbitals and we consider all the quantum effects by solving the Bogoliubov-de Gennes equations self-consistently, we agree with what Wang *et al* concluded in their semi classical approach, i.e., the four-fold star shape of the zero energy core states in LiFeAs, are related, to the rounded square shape of the γ hole pocket (see Fig. 6.10).
- In all our approximations, we found one of the main features of the Hanaguris results, which is the large LDOS peak below the Fermi energy, which serves as a checkpoint for our model (see Figures 6.7,6.9,6.10(a)). This peak was associated with the lowest energy bound state.
- Future interesting work in this ongoing project is related to the controversial gap structure in LiFeAs. We will, repeat the calculation for different gap structures, and see what vortices can say about it. Of course, it is crucial that we increase the system size in order to be able to appreciate the shape of the gap at energies far from zero and also, perform the calculations at smaller and more realistic gap sizes.

Chapter 7

Effect of vortices on the spin resonance in cuprates

In this chapter we will study the effect of the magnetic field on the neutron resonance of the cuprate superconductors (cuprates). In doing so, we will try to qualitatively reproduce some results from [54].

One of the most striking features of high T_c cuprates is that they are derived from insulating antiferromagnetic parent compounds. This proximity to magnetism has intrigued many researchers [7, 34], because it does not exist in conventional superconductors. Neutron scattering experiments show an unambiguous presence of short-range antiferromagnetic correlations in cuprates, which is the evidence for the link between magnetism and superconductivity in these materials [54]. Even so, the role of such excitations in the pairing mechanism for superconductivity is still unclear. For $YBa_2Cu_3O_{6+x}((123)O_{6+x})$, where x controls the hole doping level, the most prominent feature in the magnetic excitation spectrum is a sharp resonance [58].

Dai *et al* [54] performed neutron scattering experiments in underdoped $YBa_2Cu_3O_{6.6}$, where x and T_c are below their optimal values. The compound contains pairs of CuO_2 layers separated by charge reservoir layers. For $x = 0$, $(123)O_{6+x}$ is an antiferromagnetic insulator where the spin on each Cu^{2+} ion is antiparallel to its nearest neighbors, both in its layer and immediately adjacent layer [65]. As the oxygen content is increased, the material becomes a metal and finally near $x = 1$ it becomes a very good superconductor with $T_c = 93K$. At $x = 0.6$, T_c is reduced to around $60K$. During the evolution from insulator to superconductor, static antiferromagnetism is lost while magnetic (spin) fluctuations centered at the antiferromagnetic Bragg position $\mathbf{Q} = (\pi, \pi)$ persist [54].

Dai *et al* [54] found that this resonance exists at $34meV$ in $(123)O_{6.6}$ and it is superposed on a continuum which is gapped at low energies. Below the resonance energy, the continuum is strongest at a quartet of incommensurate positions disposed symmetrically about (π, π) [14]. They studied the effect of an external magnetic field on the resonance. In order to do so, they applied a $B = 6.8T$ field both on the ab-plane and approximately along the c-axis(20.6° rotated from the c-axis). In this chapter, we focus on the case where the magnetic field is along the c-axis. Because the background weakly depends on temperature for $T < 70K$, they show temperature difference spectrums. Fig. 7.1(b) shows the effect of superconductivity in $\chi(\mathbf{Q}, w)$ in the form of the difference between $T = 10K(< T_c)$ and $T = 70K(> T_c)$. The data show how superconductivity enhances the resonance at $34meV$. When the B field is switched on as shown in Fig. 7.1(c), even though the resonance still happens at 34 meV, the intensity gain of the resonance is suppressed by 30% compared to that at zero field 7.1(b).

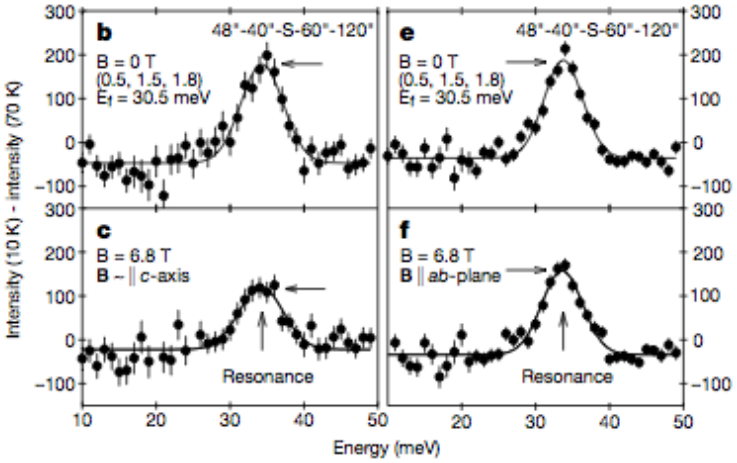

Figure 7.1: Neutron resonance at $\mathbf{Q} = (\pi, \pi)$ along the c-axis for (b) $B = 0T$, (c) $B = 6.8T$ and alone the ab-plane again for (e) $B = 0T$ (f) $B = 6.8T$. Figure taken from [54].

The neutron scattering spin resonance was also observed in various FeSC[12, 38, 48, 53] (see Fig. 7.2).

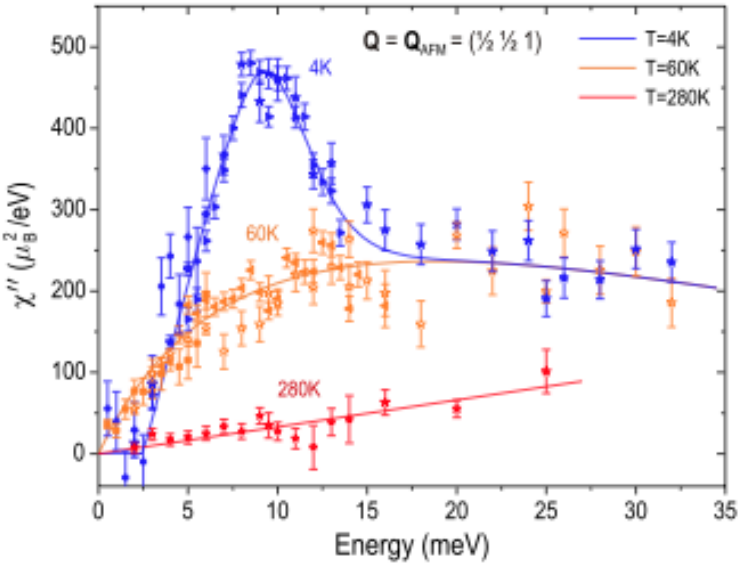

Figure 7.2: The neutron scattering spin resonance for $BaFe_{1.85}Co_{0.15}As_2(T_c = 26K)$. Figure taken from [38].

7.1 Theoretical model

As explained in Section 1.1 of Chapter 1, the building blocks of cuprates are 2-dimensional lattices of $3d$ transition metal ions. All d orbitals have weight in the Fermi surface, but among these $d_{x^2-y^2}$ is by far the one with the strongest presence; this fact allows to reduce the multiband electronic structure to an effective low-energy single band model.

Thus, our model Hamiltonian is basically the same as the one used for FeSC (see Section 2.1 of Chapter 2), with one important difference, which is that, whereas in the former model we had orbital indexes accounting for d_{xz}, d_{yz}, $d_{x^2-y^2}$, d_{xy} and $d_{3z^2-r^2}$, we now don't have them

since we treat this material as a single band system. Hence, the Hamiltonian is

$$H' = H'_0 + H'_N + H'_{int} + H'_{BCS} + H'_Z \tag{7.1}$$

where,

$$H'_0 = \sum_{ij,\sigma} t_{ij} e^{i\varphi_{ij}} \hat{c}^\dagger_{i\sigma} \hat{c}_{j\sigma}, \tag{7.2}$$

$$H'_N = -\mu_0 \sum_{i\sigma} \hat{n}_{i\sigma}, \tag{7.3}$$

$$H'_{int} = U \sum_i \hat{n}_{i\uparrow} \hat{n}_{i\downarrow}, \tag{7.4}$$

$$H'_{BCS} = -V_{ij} \sum_{i \neq j} \hat{n}_{i\uparrow} \hat{n}_{j\downarrow}, \tag{7.5}$$

$$H'_Z = \mathcal{Z}(\hat{n}_{i\uparrow} - \hat{n}_{i\downarrow}). \tag{7.6}$$

In the term H'_0, we include nearest neighbors ($t = -1.0eV$) and next-nearest neighbors ($t' = 0.3eV$) hoppings. Similar to before (see Appendix A.1), we perform a mean field decoupling in the quartic H'_{int} and H'_{BCS} terms to get the quadratic mean field Hamiltonian

$$\begin{aligned} H'^{MF} =& \sum_{ij,\sigma} t_{ij} e^{i\varphi_{ij}} \hat{c}^\dagger_{i\sigma} \hat{c}_{j\sigma} - \mu_0 \sum_{i\sigma} \hat{n}_{i\sigma} + U \sum_{i,\sigma} \langle \hat{n}_{i\bar{\sigma}} \rangle \hat{n}_{i\sigma} \\ & - \sum_{ij} [\Delta_{ij} \hat{c}^\dagger_{i\uparrow} \hat{c}^\dagger_{j\downarrow} + H.c.] + \mathcal{Z}(\hat{n}_{i\uparrow} - \hat{n}_{i\downarrow}), \end{aligned} \tag{7.7}$$

where

$$n_{i\uparrow} = \sum_l |u^l_{i\uparrow}|^2 f(E_l), \tag{7.8}$$

$$n_{i\downarrow} = \sum_l |v^l_{i\downarrow}|^2 (1 - f(E_l)), \tag{7.9}$$

$$\Delta_{ij} = V_{ij}(r) \sum_l v^{l*}_{j\downarrow} u^l_{i\uparrow} f(E_l). \tag{7.10}$$

Then, similar to Section 2.3 in Chapter 2, we perform the spin generalized Bogoliubov transformation, but in this case there is no orbital index

$$\begin{aligned} \hat{c}_{i\sigma} &= \sum_n (u^n_{i\sigma} \hat{\gamma}_{n\sigma} + v^{n*}_{i\sigma} \hat{\gamma}^\dagger_{n\bar{\sigma}}) \\ \hat{c}^\dagger_{i\sigma} &= \sum_n (u^{n*}_{i\sigma} \hat{\gamma}^\dagger_{n\sigma} + v^n_{i\sigma} \hat{\gamma}_{n\bar{\sigma}}). \end{aligned} \tag{7.11}$$

Thus, we can diagonalize the Hamiltonian by solving the BdG equations (see Appendix A.2).

7.2 Spin susceptibility calculation

Next, we want to calculate the spin susceptibility $\chi(\mathbf{q}, w)$. To do so, we first calculate $\chi_0^{+-}(\mathbf{r_i}, \mathbf{r_j}, \tau)$ in real space

$$\begin{aligned}\chi_0^{+-}(\mathbf{r_j}, \mathbf{r_i}, \tau) =& \langle T_\tau \hat{S}_j^+(0)\hat{S}_i^-(\tau)\rangle \\ =& \langle T_\tau \hat{c}_{j\uparrow}^\dagger(0)\hat{c}_{j\downarrow}(0)\hat{c}_{i\downarrow}^\dagger(\tau)\hat{c}_{i\uparrow}(\tau)\rangle \\ =& -\langle T_\tau \hat{c}_{i\uparrow}(\tau)\hat{c}_{j\uparrow}^\dagger(0)\rangle\langle T_\tau \hat{c}_{j\downarrow}(0)\hat{c}_{i\downarrow}^\dagger(\tau)\rangle \\ & -\langle T_\tau \hat{c}_{i\downarrow}^\dagger(\tau)\hat{c}_{j\uparrow}^\dagger(0)\rangle\langle T_\tau \hat{c}_{i\uparrow}(\tau)\hat{c}_{j\downarrow}(0)\rangle\end{aligned} \tag{7.12}$$

We then perform the Bogoliubov transformation in Eq. (7.12) to get

$$\begin{aligned}\chi_0^{+-}(\mathbf{r_j}, \mathbf{r_i}, \tau) = -\sum_{nm}[&(u_{i\uparrow}^n u_{j\uparrow}^{n*}\langle T_\tau \hat{\gamma}_{n\uparrow}(\tau)\hat{\gamma}_{n\uparrow}^\dagger(0)\rangle + v_{i\uparrow}^{n*}v_{j\uparrow}^n\langle T_\tau \hat{\gamma}_{n\downarrow}^\dagger(\tau)\hat{\gamma}_{n\downarrow}(0)\rangle) \\ &(u_{j\downarrow}^m u_{i\downarrow}^{m*}\langle T_\tau \hat{\gamma}_{m\downarrow}(0)\hat{\gamma}_{m\downarrow}^\dagger(\tau)\rangle + v_{j\downarrow}^{m*}v_{i\downarrow}^m\langle T_\tau \hat{\gamma}_{m\uparrow}^\dagger(0)\hat{\gamma}_{m\uparrow}(\tau)\rangle) \\ -&(u_{i\downarrow}^{n*}v_{j\uparrow}^n\langle T_\tau \hat{\gamma}_{n\downarrow}^\dagger(\tau)\hat{\gamma}_{n\downarrow}(0)\rangle + v_{i\downarrow}^n u_{j\uparrow}^{n*}\langle T_\tau \hat{\gamma}_{n\uparrow}(\tau)\hat{\gamma}_{n\uparrow}^\dagger(0)\rangle) \\ &(u_{i\uparrow}^m v_{j\downarrow}^{m*}\langle T_\tau \hat{\gamma}_{m\uparrow}(\tau)\hat{\gamma}_{m\uparrow}^\dagger(0)\rangle + v_{i\uparrow}^{m*}u_{j\downarrow}^m\langle T_\tau \hat{\gamma}_{m\downarrow}^\dagger(\tau)\hat{\gamma}_{m\downarrow}(0)\rangle)],\end{aligned} \tag{7.13}$$

where we already used that $\langle \hat{\gamma}_a \hat{\gamma}_b^\dagger\rangle = \delta_{a,b}$. By further utilizing the relations

$$\langle T_\tau \hat{\gamma}_n(\tau)\hat{\gamma}_n^\dagger(0)\rangle = (1 - f(E_n))e^{-E_n\tau} \tag{7.14}$$

$$\langle T_\tau \hat{\gamma}_n^\dagger(\tau)\hat{\gamma}_n(0)\rangle = f(E_n)e^{E_n\tau} \tag{7.15}$$

$$\langle T_\tau \hat{\gamma}_n(0)\hat{\gamma}_n^\dagger(\tau)\rangle = -f(E_n)e^{E_n\tau} \tag{7.16}$$

$$\langle T_\tau \hat{\gamma}_n^\dagger(0)\hat{\gamma}_n(\tau)\rangle = -(1 - f(E_n))e^{-E_n\tau} \tag{7.17}$$

where f is the Fermi distribution function, this becomes

$$\begin{aligned}\chi_0^{+-}(\mathbf{r_j}, \mathbf{r_i}, \tau) = -\sum_{nm}[&- u_{i\uparrow}^n u_{j\uparrow}^{n*}u_{j\downarrow}^m u_{i\downarrow}^{m*}(1 - f(E_{n\uparrow}))f(E_{m\downarrow})e^{-E_{n\uparrow}\tau}e^{E_{m\downarrow}\tau} \\ &- u_{i\uparrow}^n u_{j\uparrow}^{n*}v_{j\downarrow}^m v_{i\downarrow}^{m*}(1 - f(E_{n\uparrow}))(1 - f(E_{m\uparrow}))e^{-E_{n\uparrow}\tau}e^{-E_{m\uparrow}\tau} \\ &- v_{i\uparrow}^{n*}v_{j\uparrow}^n u_{j\downarrow}^m u_{i\downarrow}^{m*}f(E_{n\downarrow})f(E_{m\downarrow})e^{E_{n\downarrow}\tau}e^{E_{m\downarrow}\tau} \\ &- v_{i\uparrow}^{n*}v_{j\uparrow}^n v_{j\downarrow}^{m*}v_{i\downarrow}^m f(E_{n\downarrow})(1 - f(E_{m\uparrow}))e^{E_{n\downarrow}\tau}e^{E_{m\uparrow}\tau} \\ &+ u_{i\downarrow}^{n*}v_{j\uparrow}^n u_{i\uparrow}^m v_{j\downarrow}^{m*}f(E_{n\downarrow})(1 - f(E_{m\uparrow}))e^{E_n\tau}e^{-E_m\tau} \\ &+ u_{i\downarrow}^{n*}v_{j\uparrow}^n v_{i\uparrow}^{m*}u_{j\downarrow}^m f(E_{n\downarrow})f(E_{m\downarrow})e^{E_n\tau}e^{E_m\tau} \\ &+ v_{i\downarrow}^n u_{j\uparrow}^{n*}u_{i\uparrow}^m v_{j\downarrow}^{m*}(1 - f(E_{n\uparrow}))(1 - f(E_{m\uparrow}))e^{-E_n\tau}e^{-E_m\tau} \\ &+ v_{i\downarrow}^n u_{j\uparrow}^{n*}v_{i\uparrow}^{m*}u_{j\downarrow}^m(1 - f(E_{n\uparrow}))f(E_{m\downarrow})e^{-E_n\tau}e^{E_m\tau}].\end{aligned} \tag{7.18}$$

Now, by using the symmetry Eq. (A.31) given in Appendix A.2, we end up with

$$\chi_0^{+-}(\mathbf{r_j},\mathbf{r_i},\tau)=\sum_{nm}(u_{i\uparrow}^n u_{j\uparrow}^{n*}v_{j\downarrow}^{m*}v_{i\downarrow}^m-v_{i\downarrow}^n u_{j\uparrow}^{n*}u_{i\uparrow}^m v_{j\downarrow}^{m*})(1-f(E_{n\uparrow}))(1-f(E_{m\uparrow}))e^{-(E_{n\uparrow}+E_{m\uparrow})\tau}. \tag{7.19}$$

Transforming first to Matsubara frequency

$$\chi_0^{+-}(\mathbf{r_j},\mathbf{r_i},iw_n)=\int_0^\beta d\tau\chi_0^{+-}(\mathbf{r_j},\mathbf{r_i},\tau)e^{iw_n\tau} \tag{7.20}$$

and by using the relation

$$(1-f(x))(1-f(y))(e^{(-x-y)\beta}-1)=f(x)+f(y)-1, \tag{7.21}$$

we get

$$\chi_0^{+-}(\mathbf{r_j},\mathbf{r_i},iw_k)=\sum_{nm}(-u_{i\uparrow}^n u_{j\uparrow}^{n*}v_{j\downarrow}^{m*}v_{i\downarrow}^m+v_{i\downarrow}^n u_{j\uparrow}^{n*}u_{i\uparrow}^m v_{j\downarrow}^{m*})\frac{f(E_{n\uparrow})+f(E_{m\uparrow})-1}{E_{n\uparrow}+E_{m\uparrow}-iw_k}. \tag{7.22}$$

We then generate the RPA susceptibility $\chi_{RPA}^{+-}(\mathbf{r_j},\mathbf{r_i},iw_k)$, which is given by

$$\chi_{RPA}^{+-}(\mathbf{r_j},\mathbf{r_i},iw_k)=(1-U\chi_0^{+-}(\mathbf{r_j},\mathbf{r_i},iw_k))^{-1}.\chi_0^{+-}(\mathbf{r_j},\mathbf{r_i},iw_k). \tag{7.23}$$

The measured neutron cross section is proportional to the imaginary part of the Fourier transform $\chi_{RPA}^{+-}(\mathbf{q},iw_k)$ (see Eq. 1.13 in Chapter 1) given by

$$\chi_{RPA}^{+-}(\mathbf{q},iw_k)=\frac{1}{N}\sum_{ij}\chi_{RPA}^{+-}(\mathbf{r_j},\mathbf{r_i},iw_k)e^{-i\mathbf{q}\cdot(\mathbf{r_j}-\mathbf{r_i})}, \tag{7.24}$$

where we Fourier transform with respect to the $\mathbf{r_j}-\mathbf{r_i}$.
We also calculate the $\mathbf{q}$ summed susceptibility $\chi_{RPA}^{+-}(iw_k)$, given by

$$\chi_{RPA}^{+-}(iw_k)=\sum_{\mathbf{q}}\chi_{RPA}^{+-}(\mathbf{q},iw_k). \tag{7.25}$$

This quantity is relevant to compare with NMR experiments, where there is no $\mathbf{q}$ resolution.
The spin resonance at $\mathbf{Q}=(\pi,\pi)$ for the homogeneous d-wave superconductor has previously been calculated [6]. Let us understand analytically why the imaginary part of the spin susceptibility has a divergence at this wave vector. As it is well known [6], the bare spin susceptibility, $\chi_{BCS}^0(\mathbf{q},iw_n)$, of a BCS superconductor is given by

$$\begin{aligned}\chi_{BCS}^0(\mathbf{q},iw_n)=&\sum_{\mathbf{k}}\frac{1}{2}\left(1+\frac{\xi_{\mathbf{k}}\xi_{\mathbf{k+q}}+\Delta_{\mathbf{k}}\Delta_{\mathbf{k+q}}}{E_{\mathbf{k}}E_{\mathbf{k+q}}}\right)\frac{f(E_{\mathbf{k}})-f(E_{\mathbf{k+q}})}{iw_n-(E_{\mathbf{k}}-E_{\mathbf{k+q}})}\\&+\frac{1}{4}\left(1-\frac{\xi_{\mathbf{k}}\xi_{\mathbf{k+q}}+\Delta_{\mathbf{k}}\Delta_{\mathbf{k+q}}}{E_{\mathbf{k}}E_{\mathbf{k+q}}}\right)\frac{f(E_{\mathbf{k}})+f(E_{\mathbf{k+q}})-1}{iw_n-(E_{\mathbf{k}}+E_{\mathbf{k+q}})}\\&+\frac{1}{4}\left(1-\frac{\xi_{\mathbf{k}}\xi_{\mathbf{k+q}}+\Delta_{\mathbf{k}}\Delta_{\mathbf{k+q}}}{E_{\mathbf{k}}E_{\mathbf{k+q}}}\right)\frac{1-f(E_{\mathbf{k}})-f(E_{\mathbf{k+q}})}{iw_n+(E_{\mathbf{k}}+E_{\mathbf{k+q}})}.\end{aligned} \tag{7.26}$$

Here, $E_{\mathbf{k}}^2=\xi_{\mathbf{k}}^2+\Delta_{\mathbf{k}}^2$ and $\xi_{\mathbf{k}}=\epsilon_{\mathbf{k}}-\mu$ and $\Delta_{\mathbf{k}}=\frac{\Delta_0}{2}(\cos k_x-\cos k_y)$.

The fact that $\chi_0(\mathbf{q}, w)$ describes particle-hole excitations, has interesting consequences in the case of an unconventional supeconducting state. Excitations are gapped below approximatetely $2\Delta_0$; (at $T = 0$) only above this threshold does $\mathrm{Im}\chi_0(\mathbf{q}, w)$ become non-zero. The occurrence of the resonance is directly related to the factor (see Eq. (7.26))

$$\left(1 - \frac{\xi_{\mathbf{k}}\xi_{\mathbf{k+q}} + \Delta_{\mathbf{k}}\Delta_{\mathbf{k+q}}}{E_{\mathbf{k}}E_{\mathbf{k+q}}}\right), \tag{7.27}$$

which at the Fermi level becomes

$$\left(1 - \frac{\Delta_{\mathbf{k}}\Delta_{\mathbf{k+q}}}{E_{\mathbf{k}}E_{\mathbf{k+q}}}\right). \tag{7.28}$$

In order to have a resonance, it is necessary that the gap changes sign between regions on the Fermi surface or surfaces separated by a given momentum $\mathbf{Q}$ which contribute significantly to the spin scattering

$$\mathrm{sgn}(\Delta_{\mathbf{k+Q}}) = -\mathrm{sgn}(\Delta_{\mathbf{k}}). \tag{7.29}$$

In this case, the factor Eq. (7.28) goes to two (remember that at the Fermi level $E_{\mathbf{k}}^2 = \Delta_{\mathbf{k}}^2$). If there was no sign change, this factor would vanish. In the case where it doesn't vanish, the imaginary part of χ_0 posseses a discontinuous jump at $\Omega_c = min(|\Delta_{\mathbf{k}}|+|\Delta_{\mathbf{k+q}}|)$ [35]. Due to the Kraamers-Kronig relations, the real part exhibits a logarithmic singularity.

Now, the full susceptibility $\chi(\mathbf{q}, iw_n)$ is of the RPA form and it is shown in Eq. 7.30

$$\chi_{RPA}(\mathbf{q}, iw_n) = \frac{\chi^0_{BCS}(\mathbf{q}, iw_n)}{1 - U\chi^0_{BCS}(\mathbf{q}, iw_n)}, \tag{7.30}$$

where U is the Coulomb repulsion. The fact that the FS of the cuprates is resonably nested at the wave vector $\mathbf{Q} = (\pi, \pi)$ [6] (see Fig. 7.3) and that the gap changes sign between surfaces connected by this wave vector (see Fig. 1.7(c) in Chapter 1), leads to $\chi^0_{BCS}(\mathbf{q}, iw_n)$ being peaked at this wave vector.

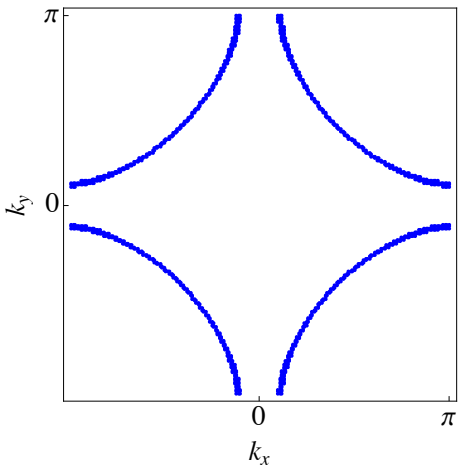

Figure 7.3: Fermi surface of the Hamiltonian H' (in Eq. (7.1)) with parameters $t = -1.0eV$, $t' = 0.3eV$, $U = 0eV$, $V_{ij} = 0eV$, $B = 0T$ and $\mu_0 = -1.0eV$, which corresponds to 15% hole doping. The semi-flat contours connected by wave vector $\mathbf{Q} = (\pi, \pi)$, lead to nesting that favors peaks of $\chi^0_{BCS}(\mathbf{q}, iw_n)$ at this wave vector.

The energies and wave vectors satisfying the dynamical Stoner criterion

$$1 - U\mathrm{Re}\chi^0_{BCS}(\mathbf{q}, iw_n) = 0 \quad \text{and} \quad \mathrm{Im}\chi^0_{BCS}(\mathbf{q}, iw_n) \text{ small}, \tag{7.31}$$

cause resonances in the full spin susceptibility $\chi_{RPA}(\mathbf{q}, iw_n)$, as shown in Fig. 7.6(a).

7.3 Results

We want to study the effect of an applied perpendicular magnetic field on the neutron resonance, both for the $\mathbf{q}$ resolved peak at $\mathbf{Q} = (\pi, \pi)$ and for the $\mathbf{q}$ summed quantity. Furthermore, we want to study the evolution of the peak as we change the strength of the onsite Coulomb interactions U. To do so, we perform the susceptibility calculations in two cases: 1) $U < U_{c1}$ where the system neither becomes spontaneously magnetic nor can vortices induce magnetization and 2) $U_{c1} < U < U_{c2}$ where the ground state is not magnetic but vortices can induce magnetization. Fig. 7.4 shows the magnetization in these two cases.

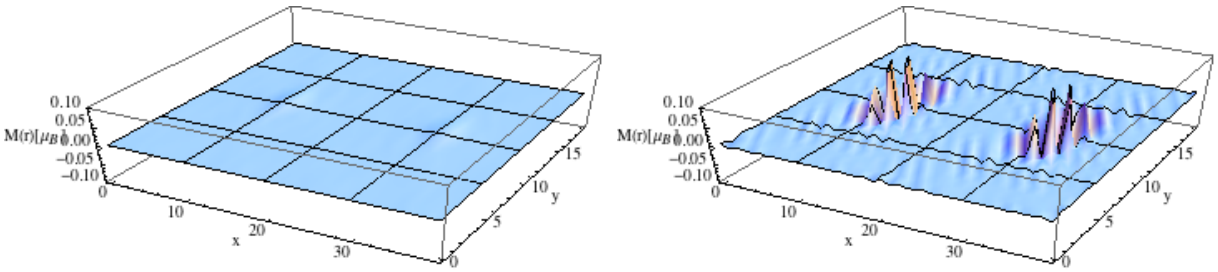

(a) (b)

Figure 7.4: Magnetization in real space for measured in units of μ_B and for (a) $U(= 0.6) < U_{c1}$ and (b) $U_{c1} < U(= 1.9) < U_{c2}$. These figures show, how there is no magnetization below U_{c1} but when $U_{c1} < U < U_{c2}$, although there is no magnetization in the system, vortices induce it in their vicinity.

In the following, we first start by showing the neutron resonance in the absence of an external magnetic field. We then show the resonance peak in the case where there is an external magnetic field. We finally show the $\mathbf{q}$ summed resonance. We do the same for the above mentioned two cases.

7.3.1 $U < U_{c1}$

In this section we study the case where there is neither a spontaneous magnetization nor vortex induced magnetization, i.e. $U < U_{c1}$ (see Fig. 7.4(a)). Fig. 7.5 shows $\mathrm{Re}\chi_0^{+-}(\mathbf{Q}, w)$ and $\mathrm{Im}\chi_0^{+-}(\mathbf{Q}, iw_k)$ where $\mathbf{Q} = (\pi, \pi)$. The cut between $\mathrm{Re}\chi_0^{+-}(\mathbf{Q}, w)$ and $1/U$, corresponds to the energy (approximately $0.615eV$) at which the dynamical Stoner criterion, given in Eq. (7.31), is fulfilled.

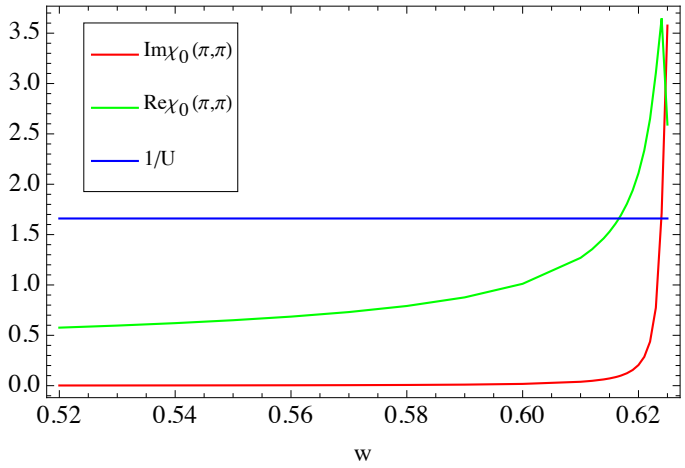

Figure 7.5: $\mathrm{Re}\chi_0^{+-}(\mathbf{Q},w)$ (green) and $\mathrm{Im}\chi_0^{+-}(\mathbf{Q},iw_k)$ (red) with $\mathbf{Q}=(\pi,\pi)$. The horizontal line indicates $1/U$ with $U=0.6eV$. The intersection point between $1/U$ and $\mathrm{Re}\chi_0^{+-}(\mathbf{Q},w)$ happens within the gap thus creating a true bound state. This is shown in Fig. 7.6(a).

This gives rise to a sharp resonance in the imaginary part of the full spin susceptibility $\chi_{RPA}^{+-}(\mathbf{Q},w)$ as one can see in Fig. 7.6(a). When an external magnetic field is applied, the resonance is almost completely suppressed and smeared out as shown in Fig. 7.6(b).

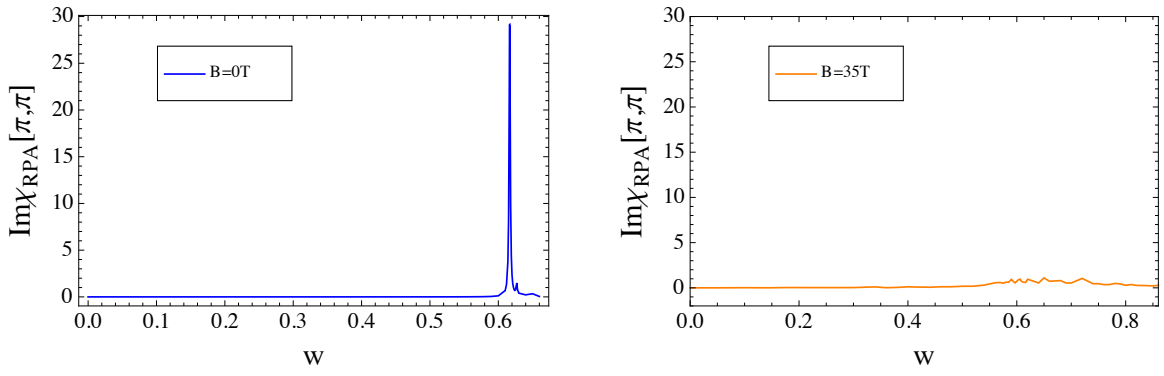

Figure 7.6: $\mathrm{Im}\chi_0^{+-}(\mathbf{Q},w)$ at $\mathbf{Q}=(\pi,\pi)$ for $U=0.6eV$. (a) The case where $B=0T$. It shows a sharp resonance at $w=0.615eV$. (b) The case where $B=35T$. The resonance is almost completely suppressed and smeared out.

This resonance reveals a gap exhibiting a threshold energy to particle-hole excitations. The excitation gap (the spin gap) to electron-hole excitations varies with q_y as can be seen in Fig. 7.7(b). In Fig. 7.7(c) it is possible to see how, apart from the strong suppression, the main effect of the magnetic field is to smear out the resonance, which is consistent with the fact that the magnetic field breaks the degeneracies splitting up the states.

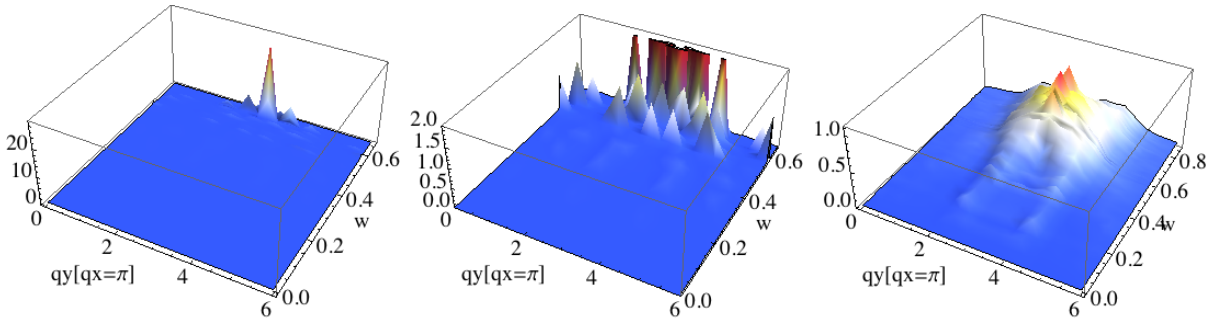

(a) (b) (c)

Figure 7.7: Im $\chi^{+-}_{RPA}(\mathbf{q}, w)$ is plotted at $q_x = \pi$ as a function q_y. (a) The case where $B = 0T$. (b) The same as (a) but in a different scale in order to appreciate the features of the resonance at energies below the large resonance at $\mathbf{Q} = (\pi, \pi)$. This figure shows how the excitation gap to electron-hole excitations varies with q_y as can be seen from the low-energy part. (c) The case where $B = 35T$.

We now show the $\mathbf{q}$ summed full susceptibility (see Eq. (7.25)) in Fig. 7.8, which as mentioned before, is relevant for NMR experiments where there is no wave vector resolution. While the $\mathbf{q}$ resolved calculation showed that there was a gap of particle-hole excitations for the concrete wave vector $\mathbf{Q} = (\pi, \pi)$, at which we know the largest resonance happens, this calculation shows the magnetic fluctuations spectra coming for all the wave vectors. The $B = 0T$ case shown in Fig. 7.8(a), shows a power-law energy dependence at low energies as expected for a d-wave superconductor (we attribute the oscillations to finite size effects). The $w = 0$ point corresponds to the $\mathbf{q}$ matching of the nodes. On the other hand, the $B = 35T$ case shown Fig. 7.8(b), also shows a power law but the spin excitations appear enhanced at low energies.

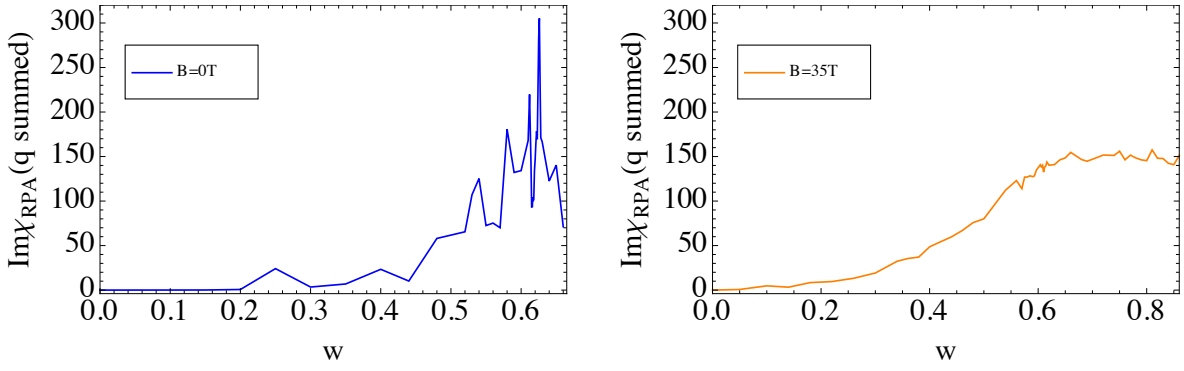

(a) (b)

Figure 7.8: Im $\chi^{+-}_{RPA}(w)$ foe $U = 0.6eV$ and magnetic fields (a) $B = 0T$ and (b) $B = 35T$.

7.3.2 $U_{c1} < U < U_{c2}$

We now increase U and enter the range where, vortices enhance the magnetization at the vortex cores. Again we find a resonance (shown in Fig. 7.9(a)), but in this case, the resonance takes place at a lower energy (approximately 0.49 eV), than in the previous lower U case (see Fig. 7.6(a)). The resonance is also larger than in the lower U case, shown in Fig. 7.6(a). In the $B \neq 0T$ case shown in Fig. 7.9(b), the resonance is again strongly suppressed and smeared out,

but less than in the previous case (see Fig. 7.6(b)). Another effect of the B field is that it slightly shifts the resonance energy downwards in energy and the height of the peak is increased.

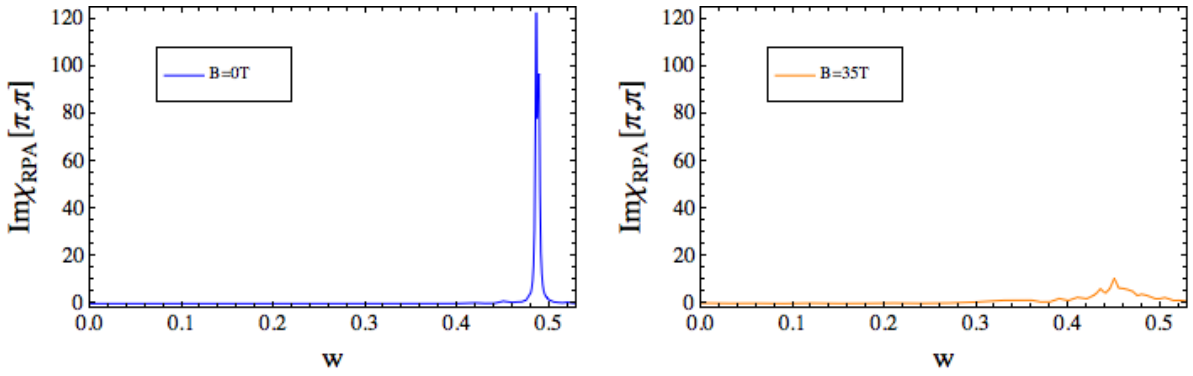

(a) (b)

Figure 7.9: $\mathrm{Im}\chi_0^{+-}(\mathbf{Q}, w)$ at $\mathbf{Q} = (\pi, \pi)$ for $U = 1.9eV$. (a) The case where $B = 0T$. It shows a resonance at $w = 0.49eV$. (b) The case where $B = 0T$. The resonance is strongly suppressed and smeared out. There is also an apparent shift downwards in energy of the peak.

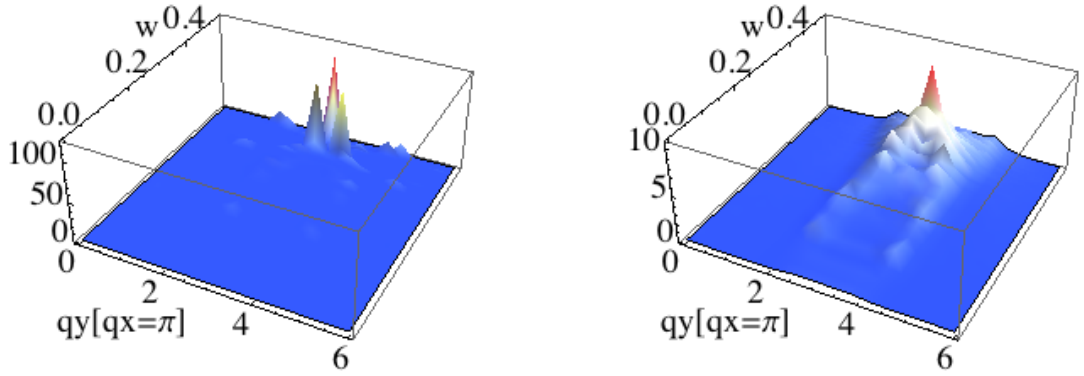

(a) (b)

Figure 7.10: Im $\chi_{RPA}^{+-}(\mathbf{q}, w)$ is plotted at $q_x = \pi$ as a function q_y for $U = 1.9eV$ and (a) $B = 0T$, (b) $B = 35T$.

We now show the $\mathbf{q}$ summed full susceptibility again in Fig. 7.11. Similar as before (see Fig. 7.8), we find the same qualitative behavior as in the $U = 0.6eV$ case.

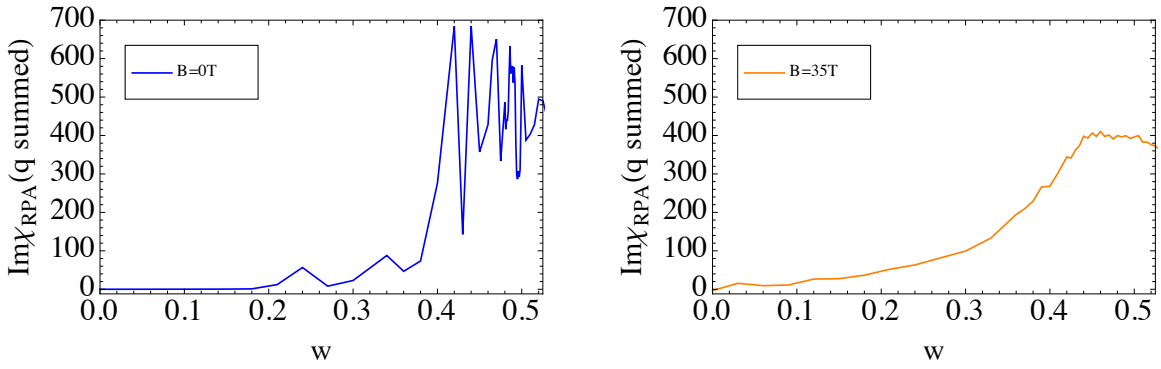

(a) (b)

Figure 7.11: Im $\chi^{+-}_{RPA}(w)$ foe $U = 1.9eV$ and magnetic fields (a) $B = 0T$ and (b) $B = 35T$.

7.4 Conclusions

• We have seen that in the presence of a strong external magnetic field, the spin resonance is strongly suppressed and smeared out (Figures 7.6 and 7.9). Our result agrees with the experimental result shown in Fig. 7.1 in that there is a suppression, but in our calculations the suppression is considerably stronger than in their measurements. We attribute this to 1) our magnetic field is much larger than theirs (ours is $35T$ whereas theirs is $6.8T$) and 2) our magnetic field is completely parallel to the c-axis whereas theirs is 20.6° rotated with respect to it. They claim that the suppression is much larger when the B field is almost along the c-axis than when it is in the ab plane. This implies that the more parallel the magnetic field is to the c-axis, the stronger the suppression should be. In the future, we plan to calculate the case for lower fields. The system size of our calculations was 40x20 lattice points, which corresponds to $B = 35T$ (note that, since the flux is fixed to two half flux quanta (see Chapter 3), the value of the magnetic field is varied by changing the system size). For example, in order to have $B = 6.6T$, we would need a 92x46 lattice.

• Our calculations have shown that, the presence of an external magnetic field slows down the magnetic fluctuations, i.e. the peak is slightly shifted downwards in energy as shown in Fig. 7.6. This is in principle in disagreement with the experimental result shown in Fig. 7.1, where the position of the resonance does not vary as a magnetic field is applied. On the one hand, we think that in principle the magnetic field should always slow down the magnetic fluctuations because it tries to align the spins. Of course, the interaction is going to be stronger for higher magnetic fields, giving rise to a larger slowing down. Hence, we think that, there is some slowing down in the experiment although too small to be measured. On the other hand the energy at which the resonance takes place is related to Δ_0 which is the magnitude of the SCOP in the bulk. It could be that due to the large coherence length of the vortices in our calculations (compared to the systemm size), the average value of Δ_0 was decreased, as shown in Fig. 7.12.

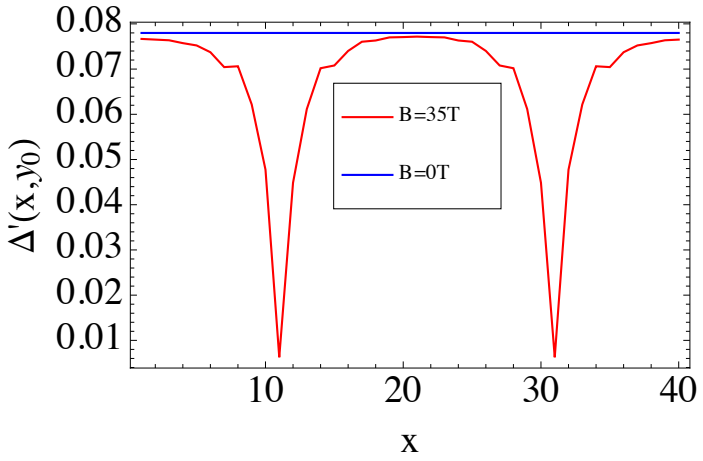

Figure 7.12: Cut of SCOP crossing the vortex cores where Δ' is minimum (red) and same cut in the case where there is no magnetic field (blue).

Looking at Fig. 7.12, it seems plausible that the shift of the peak is due to having a smaller average Δ_0 in the $B = 35T$ case, since in this case, the SCOP does not reach the bulk Δ_0 given by the blue line. This will be verified when the calculation is performed in a larger system.

Another origin of this shift could be the induced magnetization in the vortex case (see Fig. 7.4). Andersen *et al* [5] studied the disorder-induced freezing of the dynamical spin fluctuations in underdoped cuprate superconductors. They found that the low energy weight of the spin resonance arises from the disorder-induced magnetism. They found that as they increased the impurity concentration giving rise to a stronger magnetization, the spin fluctuations slowed down. Thus, we analogously interpret that, because as shown in Fig. 7.4 the vortices enhance the magnetization leading to a state with more magnetization (as the increase of impurity concentration does), the magnetic fluctuations slow down.

• Another effect we found is that, as we increase the Coulomb repulsion by increasing U, the magnetic fluctuations slow down but the height of the resonance peak is increased. Andersen *et al* found the same effect at the incommensurate wave vector $q_{IC} = (\frac{3}{4}, 1)\pi$ (see Fig. 7.13). This is related to the fact that, as we increase U while staying below the critical repulsion U_{c2} above which a global magnetic state is favorable, we approach towards the instability at $U = 1/\chi_0^{+-}(\mathbf{Q}, w)$ where the full susceptibility (shown in Eq. (7.30)) diverges. This would only diverge if we had an infinite system but what actually happens in real finite systems is that, the system breaks down and a new ground state is created, the magnetic ground state. In the magnetic state, where there is static ($w = 0$) antiferromagnetism, the resonance takes place at $w = 0$. Hence, it makes sense that, as we approach the instability, the resonance goes towards zero, until it reaches zero to give static magnetization.

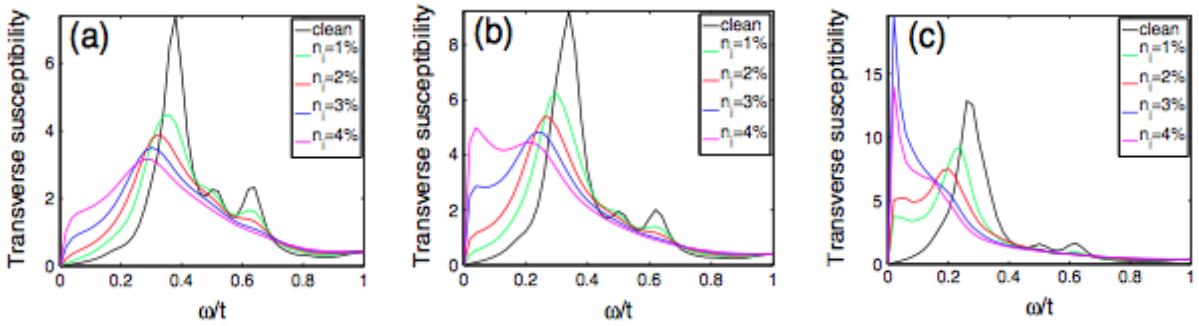

(a) (b) (c)

Figure 7.13: (a)-(c) $\chi(q_{IC}, w)$ as a function of w for different n_{imp} and $U = 2.5t$ (a), $U = 2.6t$ (b), and $U = 2.7t$ (c). Figure taken from [5].

- Regarding the shape of the resonance in the presence of a magnetic field, we do not quite agree the previous theoretical studies. Bruus *et al* [30] found that, within the SO(5) model, the resonance at $\mathbf{Q} = (\pi, \pi)$ splits into a ring centered at $\mathbf{Q}$ in the presence of a magnetic field. Instead, we find a simple smeared peak as shown in Figures 7.7(c) and 7.10(b).

Chapter 8

Conclusions

In this thesis, we have developed and implemented our studies of the magnetic field dependence of the superconducting state of the high-T_c superconductors, but specially the Fe-based superconductors. We have tried to model and understand both published and unpublished data from several research groups in Denmark [63], USA [54], and Japan [28]. Thus, it is of interest to a large part of our research community. More concretely, we have developed the machinery to solve the quantum mechanical problem of vortices inside superconductors. This has been a laborious effort but the formalism and associated computer programming has been established, optimized, and been applied to a series of interesting problems, including the effect of the magnetic field on the magnetic order of 1111 materials as well as the local density of states in LiFeAs. We have also studied the spin fluctuations and the effect of a magnetic field on the neutron scattering measurements in the cuprate high-T_c superconductors.

In doing so, we have concluded that:

• When a magnetic field is applied, the magnetic moments in the vortex cores become larger as shown in Fig. 5.6, and the larger the field, the larger this enhancement is. It is due to this enhancement that $|M(\mathbf{Q})|^2$ is enhanced by the B field in the neutron scattering measurements on the 122 materials [63], as shown in Fig. 5.4.

• In order to make the superconductivity couple to magnetism, i.e. get not only coexistence but also ("the elusive") competition in our model (see Chapter 2) as shown in Fig. 5.3, the RPA choice of pairing is not a good approach, but instead, the inter pairings should be increased such that their magnitude is closer to the magnitude of the intra pairings, compared to the RPA case, where the intra pairings are one or two orders of magnitude larger than the inter couplings. (This is not 100% sure yet, we are currently studying the problem, but we are approaching to this conclussion).

• In the most realistic calculation of LDOS in LiFeAs shown in Fig. 6.10 of Chapter 6 and Fig. A.1 of Appendix A, we find the leaking of the lowest energy states in the As-As direction, in agreement with [28] (see Fig. 6.6). We associate this shape with the square shape of the γ pocket, since as explained in [69], it causes quasiparticles from a large portion of the FS to travel along the As-As direction, forming large LDOS tails in this direction. This interpretation agrees with [69].

• Our calculations have shown that, the presence of an external magnetic field slows down the magnetic fluctuations in a one-band superconductor, i.e. the peak is slightly shifted downwards in energy as shown in Fig. 7.6, which in principle is in disagreement with the experimental result shown in Fig. 7.1, where the position of the resonance does not vary when a magnetic field is applied. We attribute this slowing down mainly to the large coherence length of the vortices compared to the system size in our calculations, which could give rise to a decrease of the average magnitude of the gap in the bulk (see Fig. 7.12). This has to be checked by

performing the calculations for systems where the coherence length, compared to the system size, is smaller. We also suggest that, analogous to what Andersen *et al* [5] find, the origin of the slowing down might be the magnetization induced by vortices.

- We have tested our code many times and in many ways, so we know that it works. It has certainly been a laborious effort, but now it is ready to be applied to many interesting problems.

Appendix A

Appendix

A.1 Mean field treatment

In order to obtain the quadratic mean-field Hamiltonian we perform a decoupling in the quartic terms. Let us start the discussion with the interaction term

$$\begin{aligned} H_{int} =& U\sum_{i\mu}\hat{n}_{i\mu\uparrow}\hat{n}_{i\mu\downarrow} + U'\sum_{i,\mu<\nu,\sigma}\hat{n}_{i\mu\sigma}\hat{n}_{i\nu\bar{\sigma}} + (U'-J)\sum_{i,\mu<\nu,\sigma}\hat{n}_{i\mu\sigma}\hat{n}_{i\nu\sigma} \\ &+ J\sum_{i,\mu<\nu,\sigma}\hat{c}^{\dagger}_{i\mu\sigma}\hat{c}^{\dagger}_{i\nu\bar{\sigma}}\hat{c}_{i\mu\bar{\sigma}}\hat{c}_{i\nu\sigma} + J'\sum_{i,\mu<\nu,\sigma}\hat{c}^{\dagger}_{i\mu\sigma}\hat{c}^{\dagger}_{i\mu\bar{\sigma}}\hat{c}_{i\nu\bar{\sigma}}\hat{c}_{i\nu\sigma}. \end{aligned} \tag{A.1}$$

We decouple it in the density channel, i.e. we keep terms like $\langle\hat{c}^{\dagger}_{i\mu\sigma}\hat{c}_{i\mu\sigma}\rangle$ and we neglect quadratic terms in fluctuations. Hence,

$$\begin{aligned} H^{MF}_{U} &= U\sum_{i\mu}(\hat{n}_{i\mu\uparrow}\langle\hat{n}_{i\mu\downarrow}\rangle + \hat{n}_{i\mu\downarrow}\langle\hat{n}_{i\mu\uparrow}\rangle + const.) \\ &= U\sum_{i\mu\sigma}(\hat{n}_{i\mu\sigma}\langle\hat{n}_{i\mu\bar{\sigma}}\rangle + const.), \end{aligned} \tag{A.2}$$

$$H^{MF}_{U'} = U'\sum_{i,\mu<\nu,\sigma}(\hat{n}_{i\mu\sigma}\langle\hat{n}_{i\nu\bar{\sigma}}\rangle + \hat{n}_{i\nu\bar{\sigma}}\langle\hat{n}_{i\mu\sigma}\rangle + const.), \tag{A.3}$$

$$H^{MF}_{(U'-J)} = (U'-J)\sum_{i,\mu<\nu,\sigma}(\hat{n}_{i\mu\sigma}\langle\hat{n}_{i\nu\sigma}\rangle + \langle\hat{n}_{i\mu\sigma}\rangle\hat{n}_{i\nu\sigma} + const.). \tag{A.4}$$

The other terms of H_{int} do not allow for decoupling in the density channel, that is why J and J' do not arise explicitly in H^{MF}_{int}. The sum of these three terms gives rise to

$$H^{MF}_{int} = \sum_{i,\mu\neq\nu,\sigma}[U\langle\hat{n}_{i\mu\bar{\sigma}}\rangle + U'\langle\hat{n}_{i\nu\bar{\sigma}}\rangle + (U'-J)\langle\hat{n}_{i\nu\sigma}\rangle]\hat{n}_{i\mu\sigma}. \tag{A.5}$$

For the BCS term,

$$H_{BCS} = -\sum_{ij,pqst}\Gamma^{st}_{pq}(r)\hat{c}^{\dagger}_{ip\uparrow}\hat{c}^{\dagger}_{jt\downarrow}\hat{c}_{js\downarrow}\hat{c}_{iq\uparrow}, \tag{A.6}$$

we decouple in the "Cooper" channel by keeping terms like $\langle \hat{c}^\dagger_{i\mu\sigma}\hat{c}^\dagger_{j\nu\bar{\sigma}}\rangle$ and $\langle \hat{c}_{j\nu\bar{\sigma}}\hat{c}_{i\mu\sigma}\rangle$ and we allow for both intra- and inter-orbital pairing, thus

$$\begin{aligned} H^{MF}_{BCS} &= -\sum_{ij,pt}\sum_{qs}(\Gamma^{st}_{pq}(r)\langle \hat{c}_{js\downarrow}\hat{c}_{iq\uparrow}\rangle \hat{c}^\dagger_{ip\uparrow}\hat{c}^\dagger_{jt\downarrow} + H.c.) \\ &= -\sum_{ij,pt}(\Delta^{pt}_{ij}\hat{c}^\dagger_{ip\uparrow}\hat{c}^\dagger_{jt\downarrow} + H.c.) \end{aligned} \tag{A.7}$$

where

$$\Delta^{pt}_{ij} = \sum_{qs}\Gamma^{st}_{pq}(r)\langle \hat{c}_{js\downarrow}\hat{c}_{iq\uparrow}\rangle. \tag{A.8}$$

We dropped the constants in both expressions because, constant terms vanish in the Bogoliubov-de Gennes equations, as we will see in the next section.

Now, we have our quadratic mean field Hamiltonian

$$\begin{aligned} H^{MF} = &\sum_{ij,\mu\nu,\sigma} t^{\mu\nu}_{ij}e^{i\varphi_{ij}}\hat{c}^\dagger_{i\mu\sigma}\hat{c}_{j\nu\sigma} - \mu_0\sum_{i\mu\sigma}\hat{n}_{i\mu\sigma} \\ &+ \sum_{i,\mu\neq\nu,\sigma}[U\langle\hat{n}_{i\mu\bar{\sigma}}\rangle + U'\langle\hat{n}_{i\nu\bar{\sigma}}\rangle + (U'-J)\langle\hat{n}_{i\nu\sigma}\rangle]\hat{n}_{i\mu\sigma} \\ &- \sum_{ij,\mu\nu}[\Delta^{\mu\nu}_{ij}\hat{c}^\dagger_{i\mu\uparrow}\hat{c}^\dagger_{j\nu\downarrow} + H.c.] + \mathcal{Z}\sum_{\mu}(\hat{n}_{i\mu\uparrow} - \hat{n}_{i\mu\downarrow}). \end{aligned} \tag{A.9}$$

A.2 Bogoliubov de-Gennes equations

In order to diagonalize our Hamiltonian, we compute the commutation $[H^{MF}, \hat{c}_{i\mu\sigma}]$ in two different ways. Let us start by commuting each part of the H^{MF}.

The kinetic energy term,

$$\begin{aligned} [H_0, \hat{c}_{k\alpha\sigma'}] &= \sum_{ij,\mu\nu,\sigma} t^{\mu\nu}_{ij}e^{i\varphi_{ij}}[\hat{c}_{i\mu\sigma}\hat{c}_{j\nu\sigma}, \hat{c}_{k\alpha\sigma'}] \\ &= -\sum_{ij,\mu\nu,\sigma} t^{\mu\nu}_{ij}e^{i\varphi_{ij}}\{\hat{c}^\dagger_{i\mu\sigma}, \hat{c}_{k\alpha\sigma'}\}\hat{c}_{j\nu\sigma} \\ &= -\sum_{j\nu} t^{\alpha\nu}_{kj}e^{i\varphi_{kj}}\hat{c}_{j\nu\sigma'}, \end{aligned} \tag{A.10}$$

thus

$$[H_0, \hat{c}_{i\mu\sigma}] = -\sum_{j\nu} t^{\mu\nu}_{ij}e^{i\varphi_{ij}}\hat{c}_{j\nu\sigma}. \tag{A.11}$$

The number of particles term,

$$\begin{aligned} [H_N, \hat{c}_{k\alpha\sigma'}] &= -\mu_0\sum_{i\mu\sigma}[\hat{c}^\dagger_{i\mu\sigma}\hat{c}_{i\mu\sigma}, \hat{c}_{k\alpha\sigma'}] \\ &= \mu_0\sum_{i\mu\sigma}\{\hat{c}^\dagger_{i\mu\sigma}, \hat{c}_{k\alpha\sigma'}\}\hat{c}_{i\mu\sigma} \\ &= \mu_0\hat{c}_{k\alpha\sigma'}, \end{aligned} \tag{A.12}$$

thus

$$[H_N, \hat{c}_{i\mu\sigma}] = \mu_0 \hat{c}_{i\mu\sigma}. \tag{A.13}$$

The interactions term,

$$\begin{aligned}
[H_{int}^{MF}, \hat{c}_{i\mu\sigma}] &= \sum_{k,b(b\neq a),\sigma'} [U\langle n_{ka\bar{\sigma}'}\rangle + U'\langle n_{kb\bar{\sigma}'}\rangle + (U'-J)\langle n_{kb\sigma'}\rangle][\hat{c}^{\dagger}_{ka\sigma'}\hat{c}_{ka\sigma'}, \hat{c}_{i\mu\sigma}] \\
&= -\sum_{k,b(b\neq a),\sigma'} [U\langle n_{ka\bar{\sigma}'}\rangle + U'\langle n_{kb\bar{\sigma}'}\rangle + (U'-J)\langle n_{kb\sigma'}\rangle]\{\hat{c}^{\dagger}_{ka\sigma'}, \hat{c}_{i\mu\sigma}\}\hat{c}_{ka\sigma'} \\
&= \sum_{\nu(\nu\neq\mu)} [U\langle n_{i\mu\bar{\sigma}}\rangle + U'\langle n_{i\nu\bar{\sigma}}\rangle + (U'-J)\langle n_{i\nu\sigma}\rangle]\hat{c}_{i\mu\sigma},
\end{aligned} \tag{A.14}$$

thus

$$[H_{int}^{MF}, \hat{c}_{i\mu\sigma}] = \sum_{\nu(\nu\neq\mu)} [U\langle n_{i\mu\bar{\sigma}}\rangle + U'\langle n_{i\nu\bar{\sigma}}\rangle + (U'-J)\langle n_{i\nu\sigma}\rangle]\hat{c}_{i\mu\sigma}. \tag{A.15}$$

The BCS term,

$$\begin{aligned}
[H_{BCS}^{MF}, \hat{c}_{k\mu\sigma}] &= -\sum_{ij,pt} \Delta_{ij}^{pt} [\hat{c}^{\dagger}_{ip\uparrow}\hat{c}^{\dagger}_{jt\downarrow}, \hat{c}_{k\mu\sigma}] \\
&= -\sum_{ij,pt} \Delta_{ij}^{pt} (\hat{c}^{\dagger}_{ip\uparrow}\{\hat{c}^{\dagger}_{jt\downarrow}, \hat{c}_{k\mu\sigma}\} - \{\hat{c}^{\dagger}_{ip\uparrow}, \hat{c}_{k\mu\sigma}\}\hat{c}^{\dagger}_{jt\downarrow}) \\
&= -\sum_{jp} \Delta_{jk}^{p\mu} \hat{c}^{\dagger}_{jp\uparrow}\delta_{\downarrow\sigma} + \sum_{jt} \Delta_{kj}^{\mu t} \hat{c}^{\dagger}_{jt\downarrow}\delta_{\uparrow\sigma},
\end{aligned} \tag{A.16}$$

thus

$$[H_{BCS}^{MF}, \hat{c}_{i\mu\sigma}] = -\sum_{j\nu} \Delta_{ji}^{\nu\mu} \hat{c}^{\dagger}_{j\nu\uparrow}\delta_{\downarrow\sigma} + \sum_{j\nu} \Delta_{ij}^{\mu\nu} \hat{c}^{\dagger}_{j\nu\downarrow}\delta_{\uparrow\sigma}. \tag{A.17}$$

The Zeeman term,

$$\begin{aligned}
[H_Z, \hat{c}_{k\alpha\sigma}] &= \mathcal{Z} \sum_{i\mu} [(\hat{n}_{i\mu\uparrow} - \hat{n}_{i\mu\downarrow}), \hat{c}_{k\alpha\sigma}] \\
&= \mathcal{Z} \sum_{\mu i} (-\{\hat{c}^{\dagger}_{i\mu\uparrow}, \hat{c}_{k\alpha\sigma}\}\hat{c}_{i\mu\uparrow} + \{\hat{c}^{\dagger}_{i\mu\downarrow}, \hat{c}_{k\alpha\sigma}\}\hat{c}_{i\mu\downarrow}) \\
&= \mathcal{Z}(-\delta_{\sigma\uparrow}\hat{c}_{k\alpha\uparrow} + \delta_{\sigma\downarrow}\hat{c}_{k\alpha\downarrow}),
\end{aligned} \tag{A.18}$$

thus

$$[H_Z, \hat{c}_{i\mu\sigma}] = \mathcal{Z}(-\delta_{\sigma\uparrow}\hat{c}_{i\mu\uparrow} + \delta_{\sigma\downarrow}\hat{c}_{i\mu\downarrow}), \tag{A.19}$$

where $\mathcal{Z} \equiv -\frac{\mu_B g_s B}{2}$.

We turn now to the second method, were we use the spin- generalized Bogoliubov transformation

$$\hat{c}_{i\mu\sigma} = \sum_n (u^n_{i\mu\sigma}\hat{\gamma}_{n\sigma} + v^{n*}_{i\mu\sigma}\hat{\gamma}^\dagger_{n\bar{\sigma}}) \tag{A.20}$$
$$\hat{c}^\dagger_{i\mu\sigma} = \sum_n (u^{n*}_{i\mu\sigma}\hat{\gamma}^\dagger_{n\sigma} + v^n_{i\mu\sigma}\hat{\gamma}_{n\bar{\sigma}}).$$

Note that

$$[H^{MF}, \hat{\gamma}_{n\sigma}] = -E_{n\sigma}\hat{\gamma}_{n\sigma}, \tag{A.21}$$
$$[H^{MF}, \hat{\gamma}^\dagger_{n\sigma}] = E_{n\sigma}\hat{\gamma}^\dagger_{n\sigma}.$$

We then get by the second method:

$$[H^{MF}, \hat{c}_{i\mu\uparrow}] = \sum_n (-E_{n\uparrow}u^n_{i\mu\uparrow}\hat{\gamma}_{n\uparrow} + E_{n\downarrow}v^{n*}_{i\mu\uparrow}\hat{\gamma}^\dagger_{n\downarrow}) \tag{A.22}$$
$$[H^{MF}, \hat{c}_{i\mu\downarrow}] = \sum_n (E_{n\uparrow}v^{n*}_{i\mu\downarrow}\hat{\gamma}^\dagger_{n\uparrow} - E_{n\downarrow}u^n_{i\mu\downarrow}\hat{\gamma}_{n\downarrow}).$$

We now have two equivalent ways of expressing the commutators. By equating the coefficients of the $\hat{\gamma}$ operators, we arrive to the Bogoliubov-de Gennes equations:

$$-E_{n\uparrow}u_{i\mu\uparrow} = -\sum_{j\nu} t^{\mu\nu}_{ij}u^n_{j\nu\uparrow} - \sum_{\nu(\nu\neq\mu)} (-\mu_0 + Un_{i\mu\downarrow} + U'n_{\nu\downarrow} + (U'-J)n_{i\nu\uparrow})u^n_{i\mu\uparrow} \tag{A.23}$$
$$- \mathcal{Z}\, u^n_{i\mu\uparrow} + \sum_{j\nu} \Delta^{\mu\nu}_{ij}v^n_{j\nu\downarrow}$$

$$E_{n\uparrow}v^{n*}_{i\mu\downarrow} = -\sum_{j\nu} t^{\mu\nu}_{ij}v^{n*}_{j\nu\downarrow} - \sum_{\nu(\nu\neq\mu)} (-\mu_0 + Un_{i\mu\uparrow} + U'n_{\nu\uparrow} + (U'-J)n_{i\nu\downarrow})v^{n*}_{i\mu\downarrow} \tag{A.24}$$
$$+ \mathcal{Z}\, v^{n*}_{i\mu\downarrow} - \sum_{j\nu} \Delta^{\nu\mu}_{ji}u^{n*}_{j\nu\uparrow}$$

$$E_{n\downarrow}v^{n*}_{i\mu\uparrow} = -\sum_{j\nu} t^{\mu\nu}_{ij}v^{n*}_{j\nu\uparrow} - \sum_{\nu(\nu\neq\mu)} (-\mu_0 + Un_{i\mu\downarrow} + U'n_{\nu\downarrow} + (U'-J)n_{i\nu\uparrow})v^{n*}_{i\mu\uparrow} \tag{A.25}$$
$$- \mathcal{Z}\, v^{n*}_{i\mu\uparrow} + \sum_{j\nu} \Delta^{\mu\nu}_{ij}u^{n*}_{j\nu\downarrow}$$

$$-E_{n\downarrow}u_{i\mu\downarrow} = -\sum_{j\nu} t^{\mu\nu}_{ij}u^n_{j\nu\downarrow} - \sum_{\nu(\nu\neq\mu)} (-\mu_0 + Un_{i\mu\uparrow} + U'n_{\nu\uparrow} + (U'-J)n_{i\nu\downarrow})u^n_{i\mu\downarrow} \tag{A.26}$$
$$+ \mathcal{Z}\, u^n_{i\mu\downarrow} - \sum_{j\nu} \Delta^{\nu\mu}_{ji}v^n_{j\nu\uparrow}$$

Upon a little manipulation we can write these equations in matrix form:

$$\begin{pmatrix} \hat{H}_\uparrow & \hat{\Delta}_{ij}^{\mu\nu} \\ \hat{\Delta}_{ji}^{\nu\mu *} & -H_\downarrow^* \end{pmatrix} \begin{pmatrix} u_\uparrow^n \\ v_\downarrow^n \end{pmatrix} = E_{n\uparrow} \begin{pmatrix} u_\uparrow^n \\ v_\downarrow^n \end{pmatrix} \tag{A.27}$$

and

$$\begin{pmatrix} \hat{H}_\downarrow & -\hat{\Delta}_{ji}^{\nu\mu} \\ -\hat{\Delta}_{ij}^{\mu\nu *} & -H_\uparrow^* \end{pmatrix} \begin{pmatrix} u_\downarrow^n \\ v_\uparrow^n \end{pmatrix} = E_{n\downarrow} \begin{pmatrix} u_\downarrow^n \\ v_\uparrow^n \end{pmatrix}, \tag{A.28}$$

where

$$\hat{H}_\sigma u_{i\mu} = \sum_{j\nu} t_{ij}^{\mu\nu} u_{j\nu}^n + \sum_{\nu(\nu\neq\mu)} (-\mu_0 + U n_{i\mu\bar{\sigma}} + U' n_{\nu\bar{\sigma}} + (U'-J) n_{i\nu\sigma}) u_{i\mu}^n + \mathcal{Z}\ u_{i\mu} \tag{A.29}$$

and

$$\hat{\Delta}_{ij}^{\mu\nu} = -\sum_{j\nu} \Delta_{ij}^{\mu\nu} u_{j\nu}. \tag{A.30}$$

Since we are concerned only with eigenvectors corresponding to positive eigenvalues and the symmetry

$$\begin{pmatrix} u_\uparrow^n \\ v_\downarrow^n \\ E_{n\uparrow} \end{pmatrix} \mapsto \begin{pmatrix} v_\uparrow^{n*} \\ u_\downarrow^{n*} \\ -E_{n\downarrow} \end{pmatrix} \tag{A.31}$$

holds, we only need to diagonalize the first matrix

$$\begin{pmatrix} \hat{H}_\uparrow & \hat{\Delta}_{ij}^{\mu\nu} \\ \hat{\Delta}_{ji}^{\nu\mu *} & -H_\downarrow^* \end{pmatrix} \begin{pmatrix} u^n \\ v^n \end{pmatrix} = E_{n\uparrow} \begin{pmatrix} u^n \\ v^n \end{pmatrix}. \tag{A.32}$$

A.3 Self-consistent fields

At this point, it is possible to express the self-consistent fields of our mean-field Hamiltonian in terms of the eigenvectors and eigenvalues:

$$\begin{aligned} n_{i\mu\uparrow} = \langle \hat{c}_{i\mu\uparrow}^\dagger \hat{c}_{i\mu\uparrow} \rangle &= \sum_n |u_{i\mu\uparrow}|^2 \langle \hat{\gamma}_{n\uparrow}^\dagger \hat{\gamma}_{n\uparrow} \rangle + \sum_n |v_{i\mu\uparrow}^n|^2 \langle \hat{\gamma}_{n\downarrow} \hat{\gamma}_{n\downarrow}^\dagger \rangle \\ &= \sum_n |u_{i\mu\uparrow}^n|^2 f(E_{n\uparrow}) + \sum_n |v_{i\mu\uparrow}^n|^2 f(-E_{n\downarrow}) \\ &= \sum_{n, E_{n\uparrow}>0} |u_{i\mu\uparrow}^n|^2 f(E_{n\uparrow}) + \sum_{n, E_{n\uparrow}<0} |u_{i\mu\uparrow}^n|^2 f(E_{n\uparrow}) \\ &= \sum_l |u_{i\mu\uparrow}^l|^2 f(E_l) \end{aligned} \tag{A.33}$$

where $\sum_n$ sums only for those n values which have positive (or negative when specified) eigenvalues, $E_{n\sigma} > 0$, and $\sum_l$ sums over all positive and negative eigenvalues. The symmetry given

in Eq. (A.31) has been used. Following the same steps we get the expression for the spin down density,

$$\begin{aligned} n_{i\mu\downarrow} &= \langle \hat{c}^{\dagger}_{i\mu\downarrow}\hat{c}_{i\mu\downarrow}\rangle = \sum_n |u_{i\mu\downarrow}|^2\langle \hat{\gamma}^{\dagger}_{n\downarrow}\hat{\gamma}_{n\downarrow}\rangle + \sum_n |v^n_{i\mu\downarrow}|^2\langle \hat{\gamma}_{n\uparrow}\hat{\gamma}^{\dagger}_{n\uparrow}\rangle \\ &= \sum_n |u^n_{i\mu\downarrow}|^2 f(E_{n\downarrow}) + \sum_n |v^n_{i\mu\downarrow}|^2 f(-E_{n\uparrow}) \\ &= \sum_{n,E_{n\uparrow}<0} |v^n_{i\mu\downarrow}|^2 f(-E_{n\uparrow}) + \sum_{n,E_{n\uparrow}>0} |v^n_{i\mu\downarrow}|^2 f(-E_{n\uparrow}) \\ &= \sum_l |v^l_{i\mu\downarrow}|^2 (1-f(E_l)) \end{aligned} \tag{A.34}$$

The SCOP:

$$\begin{aligned} \Delta^{\mu\nu}_{ij} &= \sum_{qs} \Gamma_{\mu qs\nu}(r)\langle \hat{c}_{js\downarrow}\hat{c}_{iq\uparrow}\rangle \\ &= \sum_{qs} \Gamma_{\mu qs\nu}(r)(\sum_n u^n_{js\downarrow}v^{n*}_{iq\uparrow}\langle \hat{\gamma}_{n\downarrow}\hat{\gamma}^{\dagger}_{n\downarrow}\rangle + \sum_n v^{n*}_{js\downarrow}u^n_{iq\uparrow}\langle \hat{\gamma}^{\dagger}_{n\uparrow}\hat{\gamma}_{n\uparrow}\rangle) \\ &= \sum_{qs} \Gamma_{\mu qs\nu}(r)(\sum_{n,E_{n\uparrow}<0} v^{n*}_{js\downarrow}u^n_{iq\uparrow}f(E_{n\uparrow}) + \sum_{n,E_{n\uparrow}>0} v^{n*}_{js\downarrow}u^n_{iq\uparrow}f(E_{n\uparrow})) \\ &= \sum_{qs} \Gamma_{\mu qs\nu}(r)\sum_l v^{l*}_{js\downarrow}u^l_{iq\uparrow}f(E_l) \end{aligned} \tag{A.35}$$

A.4 LDOS

Spin resolved LDOS is given by

$$N_{i\sigma}(w) = -\frac{1}{\pi}Im\sum_{n\mu}\left[\frac{|u^n_{i\mu\sigma}|^2}{w-E_{n\sigma}+i\eta} + \frac{|v^n_{i\mu\sigma}|^2}{w+E_{n\bar{\sigma}}+i\eta}\right]. \tag{A.36}$$

Thus,

$$N_{i\uparrow}(w) = -\frac{1}{\pi}Im\sum_{n\mu}\left[\frac{|u^n_{i\mu\uparrow}|^2}{w-E_{n\uparrow}+i\eta} + \frac{|v^n_{i\mu\uparrow}|^2}{w+E_{n\downarrow}+i\eta}\right] \tag{A.37}$$

$$= -\frac{1}{\pi}Im\sum_{n\mu}\left[\frac{|u^n_{i\mu\uparrow}|^2}{w-E_{n\uparrow}+i\eta} + \frac{|u^n_{i\mu\uparrow}|^2}{w-E_{n\uparrow}+i\eta}\right] \tag{A.38}$$

$$= -\frac{1}{\pi}Im\sum_{l\mu}\left[\frac{|u^l_{i\mu\uparrow}|^2}{w-E_{l\uparrow}+i\eta}\right].$$

And following the same line,

$$N_{i\downarrow}(w) = -\frac{1}{\pi}Im\sum_{n\mu}\left[\frac{|u^n_{i\mu\downarrow}|^2}{w-E_{n\downarrow}+i\eta} + \frac{|v^n_{i\mu\downarrow}|^2}{w+E_{n\uparrow}+i\eta}\right] \tag{A.39}$$

$$= -\frac{1}{\pi}Im\sum_{l\mu}\left[\frac{|v^l_{i\mu\downarrow}|^2}{w+E_{l\uparrow}+i\eta}\right]. \tag{A.40}$$

A.5 LDOS in LiFeAs

In this section, I put more figures to which I refer in Chapter 6.

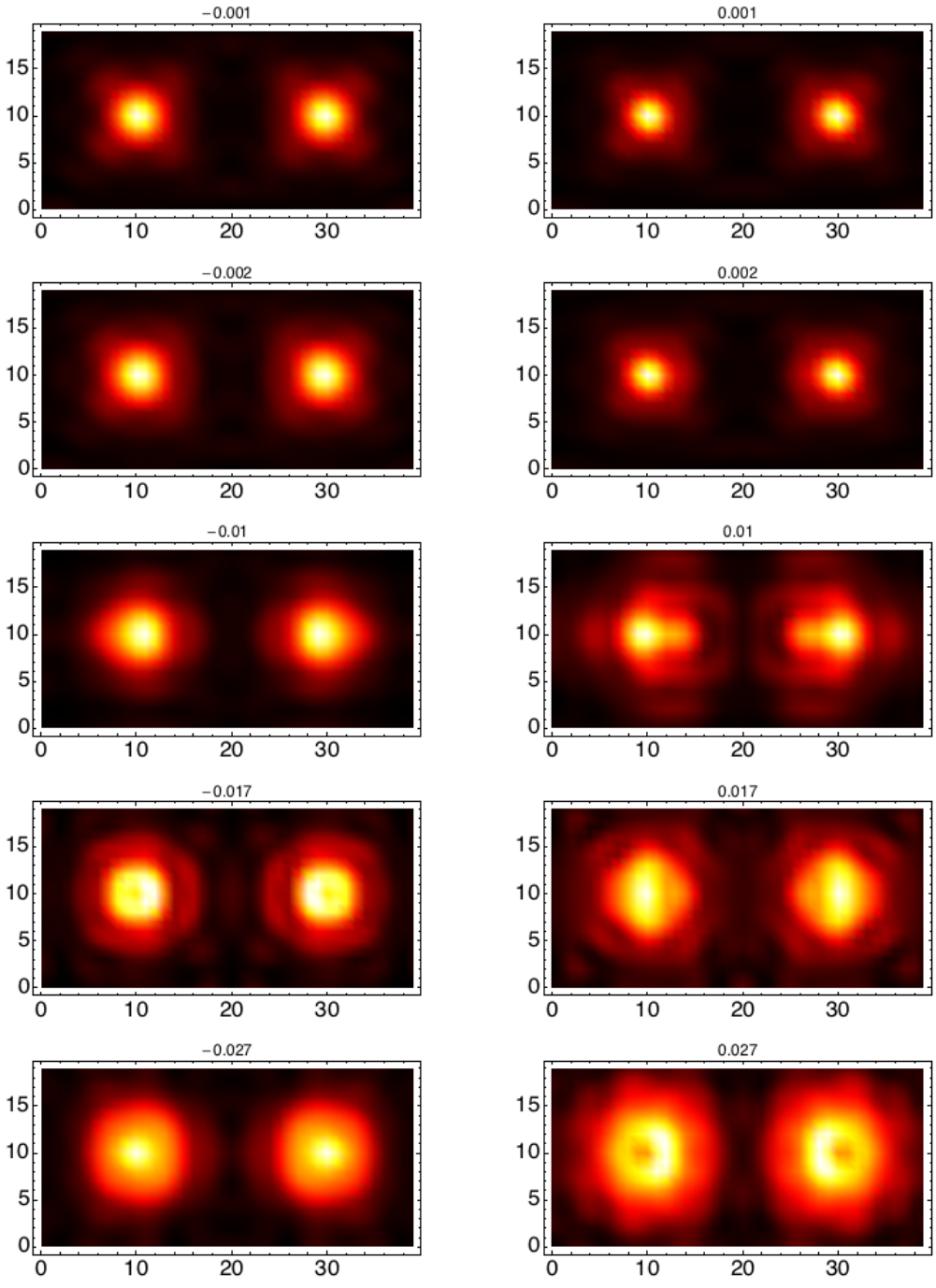

(a)

Figure A.1: Total LDOS with $B = 62.5T$, $U_{RPA} = 0.9eV$, $U = 0.86eV$ and J=U/4. The superconducting gap in the bulk, where the magnetic field does not penetrate(or the gap for $B = 0T$ case) is $\sim 50meV$.(a)Energy resolved LDOS at the vortex core with smearing $\eta = 0.6$. (b) Space resolved LDOS for different energies given above each plot in eV with $\eta = 0.3$.

Aknowledgements

In the very first place, thank you very much Brian for just being an AWESOME supervisor. Thanks for having an answer for the 99% of the questions and for pointing towards the right direction in the 1% left. Thanks for having beers with your students apart from being the boss, very important.

Thanks a lot Shantanu, for keeping it real, for having a 200% disposition to help at any time, for using and teaching me American slang every evening and for being funny. Also thanks for many many very useful discussions.

Thank you Astrid, for being sweet, for being the only Danish human being who speaks Basque and for always being willing to help. Thank you also for some very useful discussions.

Thank you Andreas, for being an angel on earth, for helping and for keeping offering your help with no limits (thanks for staying until eleven in the evening on a saturday to write my the Fortran parallelization code!!). Also thanks for the very useful discussions about LiFeAs.

Thank you very much Maria, for contributing to have a more Basque environment around us, and for doing your fancy lip hollow sound each time you passed by our office. Also thank you, for letting us use your RPA code and for some very useful discussions throughout this year.

Tak skal du have Monix, for being sweet, for making our office "hygeligt" and for being active and fun. Thanks for worrying about the good of everybody. Thanks for taking care of the gifts and thanks for being like a grandma inside. Thanks being from LOLAND. Thanks for the awesome times we had throughout the last year.

Thank you Morten for being nice and kind, always a pleasure. Thank you also for being willing to help and for some very useful discussions. Thanks for your "spæness".

Thanks Marcella, for being nice and contributing to the "hygeligtness" of our office. Thanks for the crackers. Thanks for the many awesome times we had throughout the last year.

Thanks Asger, for being another angel on earth. Thanks, for being the wise 200 years old man, interested in History, the Basque whale hunters and "elg". Thanks for your contribution to the "hygeligtness" of our office.

Thanks Erikas for having an answer to every question I had throughout the last year and a half and for always helping when needed.

Thanks Mathias Lunde for being one of the funniest people I know and for being inappropriate.

Thanks Kim for saying Agur, and for worrying about my girlfriend Mathematica.

Thanks also Gediminas for helping me introduce to the many-body physics in the early days and for being nice and helpful many times throughout the last two years.

Thanks Anine for being sweet and for helping me out with Latex in the last day.

Thanks also Konrad, Samuel, Mathias Rosdalh, Marius, Vladimir, Jeroen and the Professors for making the Condensed Matter Theory group a friendly working environment.

Thanks to all my teachers at the University of the Basque Country, mainly for the knowledge I acquired from them and also for making the way nice.

Thank you Professor Emilio Artacho for introducing me to research in Physics and for being always helpful regarding recommendation letters, advice...

Thank you very much to all my family, especially my father Luis for pushing and working hard for my scholarships, applications etc. , my mother Mireia for always being sweet, my sister Uma for being funny, generous and having let me take a break every year in Dubai and my grandparents amama Pepita, amama Agustina and aitite Toribio for treating me like a King each time I go home. Thank you for always being there and for having had made the greatest contribution to my success in my academic carrier.

I also thank my girlfriend Itziar, for putting up with "my physics" and for being adorable.

Finally, thank you very much to La Caixa bank, for giving me a scholarship, which made possible this amazing experience in Copenhagen.

Bibliography

[1] *http://web.stanford.edu/group/photontheory/ARPES.html*.

[2] F. Ahn, I. Eremin, J. Knolle, V. B. Zabolotnyy, S. V. Borisenko, B. Büchner, and A. V. Chubukov. Superconductivity from repulsion in lifeas: Novel s-wave symmetry and potential time-reversal symmetry breaking. *Phys. Rev. B*, 89:144513, Apr 2014.

[3] M. P. Allan, A. W. Rost, A. P. Mackenzie, Yang Xie, J. C. Davis, K. Kihou, C. H. Lee, A. Iyo, H. Eisaki, and T.-M. Chuang. Anisotropic energy gaps of iron-based superconductivity from intraband quasiparticle interference in lifeas. *Science*, 336(6081):563–567, 2012.

[4] Alexander Altland and Ben Simons. *Condensed Matter Field Theory*.

[5] Brian M. Andersen, Siegfried Graser, and P. J. Hirschfeld. Disorder-induced freezing of dynamical spin fluctuations in underdoped cuprate superconductors. *Phys. Rev. Lett.*, 105:147002, Sep 2010.

[6] Brian Moller Andersen. Coexistence of magnetic and superconducting order in the high-tc materials. Master's thesis, Niels Bohr Institute, Copenhagen University, 2004.

[7] P. W. ANDERSON. The resonating valence bond state in la2cuo4 and superconductivity. *Science*, 235(4793):1196–1198, 1987.

[8] S. V. Borisenko, V. B. Zabolotnyy, D. V. Evtushinsky, T. K. Kim, I. V. Morozov, A. N. Yaresko, A. A. Kordyuk, G. Behr, A. Vasiliev, R. Follath, and B. Büchner. Superconductivity without nesting in lifeas. *Phys. Rev. Lett.*, 105:067002, Aug 2010.

[9] Sergey V. Borisenko, Volodymyr B. Zabolotnyy, Alexnader A. Kordyuk, Danil V. Evtushinsky, Timur K. Kim, Igor V. Morozov, Rolf Follath, and Bernd Bchner. One-sign order parameter in iron based superconductor. *Symmetry*, 4:251–264, 2012.

[10] J.Matricon C.Caroli, P.G.De Gennes. Bound fermion states on a vortex line in a type ii superconductor. *Phys. Lett.*, 9, 1964.

[11] Shun Chi, S. Johnston, G. Levy, S. Grothe, R. Szedlak, B. Ludbrook, Ruixing Liang, P. Dosanjh, S. A. Burke, A. Damascelli, D. A. Bonn, W. N. Hardy, and Y. Pennec. Sign inversion in the superconducting order parameter of lifeas inferred from bogoliubov quasiparticle interference. *Phys. Rev. B*, 89, Mar 2014.

[12] A. D. Christianson, E. A. Goremychkin, R. Osborn, S. Rosenkranz, M. D. Lumsden, C. D. Malliakas, I. S. Todorov, H. Claus, D. Y. Chung, M. G. Kanatzidis, R. I. Bewley, and T. Guidi. Unconventional superconductivity in ba0.6k0.4fe2as2 from inelastic neutron scattering. *Nature*, 456(7224):930–932, 12 2008.

[13] S.-K. Mo A. S. Erickson-J. Analytis J.-H. Chu D.J. Singh Z. Hussain T. H. Geballe I. R. Fisher D. H. Lu, M. Yi and Z.-X. Shen. Electronic structure of the iron-based superconductor laofep. *Nature*, 455, 2008.

[14] Pengcheng Dai, H. A. Mook, and F. Doğan. Incommensurate magnetic fluctuations in $\mathrm{yba_2cu_3}O_{6.6}$. *Phys. Rev. Lett.*, 80:1738–1741, Feb 1998.

[15] D.J.Scalapino. The case for $d_{x^2-y^2}$ pairing in the cup rate superconductors. *Physics Reports*, 250:329–365, 1995.

[16] Adriana Moreo Elbio Dagotto, Takashi Hotta. Colossal magneto resistant materials: the key role of phase separation. *Physics Reports*, 344, 2001.

[17] Song et al. Electronic hinomogeneity and vortex disorder in superconducting $sr_{0.75}k_{0.25}fe_2as_2$. *arXiv*, 1212.3240, 2012.

[18] Y. Fasano, I. Maggio-Aprile, N. D. Zhigadlo, S. Katrych, J. Karpinski, and Ø. Fischer. Local quasiparticle density of states of superconducting $\mathrm{smfeaso_{1-x}f_x}$ single crystals: Evidence for spin-mediated pairing. *Phys. Rev. Lett.*, 105:167005, Oct 2010.

[19] Johannes Ferber, Kateryna Foyevtsova, Roser Valentí, and Harald O. Jeschke. Lda + dmft study of the effects of correlation in lifeas. *Phys. Rev. B*, 85:094505, Mar 2012.

[20] Maria N. Gastiasoro, P. J. Hirschfeld, and Brian M. Andersen. Impurity states and cooperative magnetic order in fe-based superconductors. *Phys. Rev. B*, 88:220509, Dec 2013.

[21] Maria Navarro Gastiasoro. Bogoliubov-de gennes studies of fe-based superconductors.

[22] A. A. Golubov, O. V. Dolgov, A. V. Boris, A. Charnukha, D. L. Sun, C. T. Lin, A. F. Shevchun, A. V. Korobenko, M. R. Trunin, and V. N. Zverev. Normal state resistivity of $\mathrm{ba_{1-x}k_xfe_2as_2}$: evidence for multiband strong-coupling behavior. 2010.

[23] Akira Goto. Magnetic translation group on abrikosov lattice. *Czechoslovak Journal of Physics*, 46, 1996.

[24] Grasser. private communication.

[25] J. S. Griffith. *The theory of transition-metal ions.* 1961.

[26] George Gruner. *Density waves in solids.* PERSEUS PUBLISHING, 1994.

[27] T. Hajiri, T. Ito, R. Niwa, M. Matsunami, B. H. Min, Y. S. Kwon, and S. Kimura. Three-dimensional electronic structure and interband nesting in the stoichiometric superconductor lifeas. *Phys. Rev. B*, 85:094509, Mar 2012.

[28] T. Hanaguri, K. Kitagawa, K. Matsubayashi, Y. Mazaki, Y. Uwatoko, and H. Takagi. Scanning tunneling microscopy/spectroscopy of vortices in lifeas. *Phys. Rev. B*, 85:214505, Jun 2012.

[29] N. Hayashi, T. Isoshima, M. Ichioka, and K. Machida. Low-lying quasiparticle excitations around a vortex core in quantum limit. *Phys. Rev. Lett.*, 80:2921–2924, Mar 1998.

[30] Karsten Flensberg Henrik Bruus. *Many-Body Quantum Theory in Condensed Matter Physics.*

[31] Christian Hess, Steffen Sykora, Torben Hänke, Ronny Schlegel, Danny Baumann, Volodymyr B. Zabolotnyy, Luminita Harnagea, Sabine Wurmehl, Jeroen van den Brink, and Bernd Büchner. Interband quasiparticle scattering in superconducting lifeas reconciles photoemission and tunneling measurements. *Phys. Rev. Lett.*, 110:017006, Jan 2013.

[32] H. F. Hess, R. B. Robinson, R. C. Dynes, J. M. Valles, and J. V. Waszczak. Scanning-tunneling-microscope observation of the abrikosov flux lattice and the density of states near and inside a fluxoid. *Phys. Rev. Lett.*, 62, Jan 1989.

[33] H. F. Hess, R. B. Robinson, and J. V. Waszczak. Vortex-core structure observed with a scanning tunneling microscope. *Phys. Rev. Lett.*, 64:2711–2714, May 1990.

[34] J. E. Hirsch. Antiferromagnetism, localization, and pairing in a two-dimensional model for cuo$_2$. *Phys. Rev. Lett.*, 59:228–231, Jul 1987.

[35] P J Hirschfeld, M M Korshunov, and I I Mazin. Gap symmetry and structure of fe-based superconductors. *Reports on Progress in Physics*, 74, 2011.

[36] Jennifer E Hoffman. Spectroscopic scanning tunneling microscopy insights into fe-based superconductors. *Reports on Progress in Physics*, 74, 2011.

[37] Hiroaki Ikeda, Ryotaro Arita, and Jan Kuneš. Phase diagram and gap anisotropy in iron-pnictide superconductors. *Phys. Rev. B*, 81:054502, Feb 2010.

[38] D. S. Inosov, J. T. Park, P. Bourges, D. L. Sun, Y. Sidis, A. Schneidewind, K. Hradil, D. Haug, C. T. Lin, B. Keimer, and V. Hinkov. Normal-state spin dynamics and temperature-dependent spin-resonance energy in optimally doped bafe1.85co0.15as2. *Nat Phys*, 6, 2010.

[39] P. Jeglič, A. Potočnik, M. Klanjšek, M. Bobnar, M. Jagodič, K. Koch, H. Rosner, S. Margadonna, B. Lv, A. M. Guloy, and D. Arčon. ^{75}As. *Phys. Rev. B*, 81:140511, Apr 2010.

[40] Bing Shen Bin Zeng Yan Huang-Ang Li Da Wang Huan Yang Cong Ren Qiang-Hua Wang Shuheng H. Pan Jei Shan, Yong-Lei Wang and Hai-Hu Wen. Observaition of ordered vortices with andreev bound states in $ba_{0.6}k_{0.4}fe_2as_2$. *Nature Physics*, 7:325–331, 2011.

[41] Yoichi Kamihara, Takumi Watanabe, Masahiro Hirano, and Hideo Hosono. Iron-based layered superconductor la[o1-xfx]feas (x = 0.050.12) with tc = 26 k. *Journal of the American Chemical Society*, 130(11):3296–3297, 2008.

[42] A. F. Kemper, M. M. Korshunov, T. P. Devereaux, J. N. Fry, H-P. Cheng, and P. J. Hirschfeld. Anisotropic quasiparticle lifetimes in fe-based superconductors. *Phys. Rev. B*, 83:184516, May 2011.

[43] Daniel I. Khomskii. *Basic Aspects of the Quantum Theory of Solids*. CAMBRIDGE UNIVERSITY PRESS, 2010.

[44] Kazuhiko Kuroki, Seiichiro Onari, Ryotaro Arita, Hidetomo Usui, Yukio Tanaka, Hiroshi Kontani, and Hideo Aoki. Unconventional pairing originating from the disconnected fermi surfaces of superconducting lafeaso1-xfx. *Phys. Rev. Lett.*, 101:087004, Aug 2008.

[45] Alexander Lankau, Klaus Koepernik, Sergey Borisenko, Volodymyr Zabolotnyy, Bernd Büchner, Jeroen van den Brink, and Helmut Eschrig. Absence of surface states for lifeas investigated using density functional calculations. *Phys. Rev. B*, 82:184518, Nov 2010.

[46] Geunsik Lee, Hyo Seok Ji, Yeongkwan Kim, Changyoung Kim, Kristjan Haule, Gabriel Kotliar, Bumsung Lee, Seunghyun Khim, Kee Hoon Kim, Kwang S. Kim, Ki-Seok Kim, and Ji Hoon Shim. Orbital selective fermi surface shifts and mechanism of high T_c superconductivity in correlated aFeAs (a = Li, na). *Phys. Rev. Lett.*, 109:177001, Oct 2012.

[47] S.W. Lovesey. *Theory of neutron scattering from condensed matter.* Clarendon Press, Oxford.

[48] M D Lumsden and A D Christianson. Magnetism in fe-based superconductors. *Journal of Physics: Condensed Matter*, 22, 2010.

[49] T. A. Maier, S. Graser, D. J. Scalapino, and P. J. Hirschfeld. Origin of gap anisotropy in spin fluctuation models of the iron pnictides. *Phys. Rev. B*, 79:224510, Jun 2009.

[50] Nicola Marzari and David Vanderbilt. Maximally localized generalized wannier functions for composite energy bands. *Phys. Rev. B*, 56:12847–12865, Nov 1997.

[51] I. I. Mazin, D. J. Singh, M. D. Johannes, and M. H. Du. Unconventional superconductivity with a sign reversal in the order parameter of lafeaso$_{1-x}$f$_x$. *Phys. Rev. Lett.*, 101:057003, Jul 2008.

[52] N. Ni, M. E. Tillman, J.-Q. Yan, A. Kracher, S. T. Hannahs, S. L. Bud'ko, and P. C. Canfield. Effects of co substitution on thermodynamic and transport properties and anisotropic h_{c2} in $ba(fe_{(1-x)}co_x)_2as_2$ single crystals. *Phys. Rev. B*, 78:214515, Dec 2008.

[53] J. T. Park, G. Friemel, Yuan Li, J.-H. Kim, V. Tsurkan, J. Deisenhofer, H.-A. Krug von Nidda, A. Loidl, A. Ivanov, B. Keimer, and D. S. Inosov. Magnetic resonant mode in the low-energy spin-excitation spectrum of superconducting rb$_2$fe$_4$se$_5$ single crystals. *Phys. Rev. Lett.*, 107:177005, Oct 2011.

[54] G. Aepli S. M. Hayden Pengcheng Dai, H. A. Mook and F. Dogan. Resonance as measure of pairing correlations in the high-tc superconductor $yba_2cu_3o_{6.6}$. *Nature*, 406, 2000.

[55] Daniela Pfannkuche and Rolf R. Gerhardts. Theory of magnetotransport in two-dimensional electron systems subjected to weak two-dimensional superlattice potentials. *Phys. Rev. B*, 46:12606–12626, Nov 1992.

[56] D. K. Pratt, W. Tian, A. Kreyssig, J. L. Zarestky, S. Nandi, N. Ni, S. L. Bud'ko, P. C. Canfield, A. I. Goldman, and R. J. McQueeney. Coexistence of competing antiferromagnetic and superconducting phases in the underdoped Ba(fe$_{0.953}$co$_{0.047}$)$_2$as$_2$ compound using x-ray and neutron scattering techniques. *Phys. Rev. Lett.*, 103:087001, Aug 2009.

[57] X B He Guorong Li Ru-wen Peng J R Thompson B C Sales A S Sefat M A McGuire D Mandrus J F Wendelken V Keppens R Jin, M H pan and E W Plummer. Elecgronic, magnetic and optical properties of two fe-based superconductors and related parent compounds. *Supercond. Sci. Technol.*, 23, 2010.

[58] J. et al. Rossat-Mignod. Neutron scattering study of the $yba_2cu_3o_{6+x}$. *Physica C*, 185-189, 1991.

[59] P. J. Hirschfeld D. J. Scalapino S. Graser, T. A. Maier. Near-degeneracy of several pairing channels in multi orbital models for the fe pnictides. *New Journal of Physics*, 11, 2009.

[60] P J Maier P J Hirschfeld S Graser, T A Maier and D J Scalapino. Near-degeneracy of several pairing channels in multi orbital models for the fe pnictides. *N. J. of Phys.*, 11, Feb 2009.

[61] Jeno Solyom. *Fundamentals of the Physics of Solids-Vol. I.*

[62] Can-Li Song, Yi-Lin Wang, Peng Cheng, Ye-Ping Jiang, Wei Li, Tong Zhang, Zhi Li, Ke He, Lili Wang, Jin-Feng Jia, Hsiang-Hsuan Hung, Congjun Wu, Xucun Ma, Xi Chen, and Qi-Kun Xue. Direct observation of nodes and twofold symmetry in fese superconductor. *Science*, 332(6036):1410–1413, 2011.

[63] Gitte Stieper. Competing superconducting and magnetic order parameters and field induced magnetism in $ba(fe_{0.95}co_{0.05})_2as_2$. Master's thesis, Niels Bohe Institute, Copenhagen University, 2012.

[64] A. E. Taylor, M. J. Pitcher, R. A. Ewings, T. G. Perring, S. J. Clarke, and A. T. Boothroyd. Antiferromagnetic spin fluctuations in lifeas observed by neutron scattering. *Phys. Rev. B*, 83:220514, Jun 2011.

[65] J. M. Tranquada, D. E. Cox, W. Kunnmann, H. Moudden, G. Shirane, M. Suenaga, P. Zolliker, D. Vaknin, S. K. Sinha, M. S. Alvarez, A. J. Jacobson, and D. C. Johnston. Neutron-diffraction determination of antiferromagnetic structure of cu ions in $Yba_2cu_3o_{6+x}$ with $x = 0.0and0.15$. *Phys. Rev. Lett.*, 60:156–159, Jan 1988.

[66] Wei-Feng Tsai, Yan-Yang Zhang, Chen Fang, and Jiangping Hu. Impurity-induced bound states in iron-based superconductors with s-wave $cosk_xcosk_y$ pairing symmetry. *Phys. Rev. B*, 80:064513, Aug 2009.

[67] K. Umezawa, Y. Li, H. Miao, K. Nakayama, Z.-H. Liu, P. Richard, T. Sato, J. B. He, D.-M. Wang, G. F. Chen, H. Ding, T. Takahashi, and S.-C. Wang. Unconventional anisotropic s-wave superconducting gaps of the lifeas iron-pnictide superconductor. *Phys. Rev. Lett.*, 108:037002, Jan 2012.

[68] Y. Wang, A. Kreisel, V. B. Zabolotnyy, S. V. Borisenko, B. Büchner, T. A. Maier, P. J. Hirschfeld, and D. J. Scalapino. Superconducting gap in lifeas from three-dimensional spin-fluctuation pairing calculations. *Phys. Rev. B*, 88:174516, Nov 2013.

[69] Yan Wang, Peter J. Hirschfeld, and Ilya Vekhter. Theory of quasiparticle vortex bound states in iron-based superconductors: Application to scanning tunneling spectroscopy of lifeas. *Phys. Rev. B*, 85:020506, Jan 2012.

[70] Yong Wang and A. H. MacDonald. Mixed-state quasiparticle spectrum for d-wave superconductors. *Phys. Rev. B*, 52, Aug 1995.

[71] B. Andrei Bernevig with Taylor L. Hughes. *Topological insulators and topological super conductors.*

[72] Z.P. Yin, K. Haule, and G. Kotliar. Kinetic frustration and the nature of the magnetic and paramagnetic states in iron pnictides and iron chalcogenides. *Nat Mater*, 10:932–935, 12 2011.

[73] Degang Zhang. Nonmagnetic impurity resonances as a signature of sign-reversal pairing in feas-based superconductors. *Phys. Rev. Lett.*, 103:186402, Oct 2009.

[74] Tao Zhou, Degang Zhang, and C. S. Ting. Spin-density wave and asymmetry of coherence peaks in iron pnictide superconductors from a two-orbital model. *Phys. Rev. B*, 81:052506, Feb 2010.